CANADIAN THESES ON MICROFICHE

I.S.B.N.

THESES CANADIENNES SUR MICROFICHE

National Library of Canada
Collections Development Branch

Canadian Theses on
Microfiche Service

Ottawa, Canada
K1A 0N4

Bibliothèque nationale du Canada
Direction du développement des collections

Service des thèses canadiennes
sur microfiche

NOTICE

The quality of this microfiche is heavily dependent upon the quality of the original thesis submitted for microfilming. Every effort has been made to ensure the highest quality of reproduction possible.

If pages are missing, contact the university which granted the degree.

Some pages may have indistinct print especially if the original pages were typed with a poor typewriter ribbon or if the university sent us a poor photocopy.

Previously copyrighted materials (journal articles, published tests, etc.) are not filmed.

Reproduction in full or in part of this film is governed by the Canadian Copyright Act, R.S.C. 1970, c. C-30. Please read the authorization forms which accompany this thesis.

THIS DISSERTATION
HAS BEEN MICROFILMED
EXACTLY AS RECEIVED

AVIS

La qualité de cette microfiche dépend grandement de la qualité de la thèse soumise au microfilmage. Nous avons tout fait pour assurer une qualité supérieure de reproduction.

S'il manque des pages, veuillez communiquer avec l'université qui a conféré le grade.

La qualité d'impression de certaines pages peut laisser à désirer, surtout si les pages originales ont été dactylographiées à l'aide d'un ruban usé ou si l'université nous a fait parvenir une photocopie de mauvaise qualité.

Les documents qui font déjà l'objet d'un droit d'auteur (articles de revue, examens publiés, etc.) ne sont pas microfilmés.

La reproduction, même partielle, de ce microfilm est soumise à la Loi canadienne sur le droit d'auteur, SRC 1970, c. C-30. Veuillez prendre connaissance des formules d'autorisation qui accompagnent cette thèse.

LA THÈSE A ÉTÉ
MICROFILMÉE TELLE QUE
NOUS L'AVONS REÇUE

NL-339 (r. 82/08)

Canada

0-315-08975-X

National Library of Canada
Bibliothèque nationale du Canada

88

Canadian Theses Division
Division des thèses canadiennes

Ottawa, Canada
K1A 0N4

56892

PERMISSION TO MICROFILM — AUTORISATION DE MICROFILMER

- Please print or type — Écrire en lettres moulées ou dactylographier

Full Name of Author — Nom complet de l'auteur
MOTOI KUMAI

Date of Birth — Date de naissance
Sep. 14, 1948

Country of Birth — Lieu de naissance
JAPAN

Permanent Address — Résidence fixe
Japan Petroleum Exploration Co, Ltd.
1-18-14 Ebisu Shibuya-ku, Tokyo, JAPAN

Title of Thesis — Titre de la thèse
Determination of Hydraulic Fracture Parameters from Surface Deformation

University — Université
The University of Alberta

Degree for which thesis was presented — Grade pour lequel cette thèse fut présentée
M. Sc

Year this degree conferred — Année d'obtention de ce grade
1982

Name of Supervisor — Nom du directeur de thèse
Dr. Edo Nyland

Permission is hereby granted to the NATIONAL LIBRARY OF CANADA to microfilm this thesis and to lend or sell copies of the film.

The author reserves other publication rights, and neither the thesis nor extensive extracts from it may be printed or otherwise reproduced without the author's written permission.

L'autorisation est, par la présente, accordée à la BIBLIOTHÈQUE NATIONALE DU CANADA de microfilmer cette thèse et de prêter ou de vendre des exemplaires du film.

L'auteur se réserve les autres droits de publication; ni la thèse ni de longs extraits de celle-ci ne doivent être imprimés ou autrement reproduits sans l'autorisation écrite de l'auteur.

Date
April 15, 1982

Signature
Motoi Kumai

NL-91 (4/77)

THE UNIVERSITY OF ALBERTA

Determination of Hydraulic Fracture Parameters from Surface Deformation

by

©

Motoi Kumai

A THESIS
SUBMITTED TO THE FACULTY OF GRADUATE STUDIES AND RESEARCH
IN PARTIAL FULFILMENT OF THE REQUIREMENTS FOR THE DEGREE
OF Master of Science
IN
Geophysics

Department of Physics

Edmonton, Alberta
Spring 1982

THE UNIVERSITY OF ALBERTA

RELEASE FORM

NAME OF AUTHOR Motoi Kumai

TITLE OF THESIS Determination of Hydraulic Fracture Parameters from Surface Deformation

DEGREE FOR WHICH THESIS WAS PRESENTED Master of Science

YEAR THIS DEGREE GRANTED Spring 1982

Permission is hereby granted to THE UNIVERSITY OF ALBERTA LIBRARY to reproduce single copies of this thesis and to lend or sell such copies for private, scholarly or scientific research purposes only.

The author reserves other publication rights, and neither the thesis nor extensive extracts from it may be printed or otherwise reproduced without the author's written permission.

(SIGNED) Motoi Kumai

PERMANENT ADDRESS:

Japan Petroleum Exploration Co., Ltd.
1-18-14 Ebisu Shibuya-ku
Tokyo, Japan

DATED March 26 1982

THE UNIVERSITY OF ALBERTA

FACULTY OF GRADUATE STUDIES AND RESEARCH

The undersigned certify that they have read, and recommend to the Faculty of Graduate Studies and Research, for acceptance, a thesis entitled Determination of Hydraulic Fracture Parameters from Surface Deformation submitted by Motoi Kumai in partial fulfilment of the requirements for the degree of Master of Science in Geophysics.

....

Supervisor

....

....

....

Date.....March 26, 1982.....

ABSTRACT

The use of hydraulic fracturing in the field of energy resources development has generated a need for effective methods to determine the size and orientation of induced fractures. Surface deformation monitoring has been considered as one of the feasible geophysical methods. In order to understand its relevance, we have to understand how well the surface deformation delineates changes of the source parameters of fracture.

I review past studies of hydraulic fracturing; field experiments of deformation monitoring and basic problems in the behavior of hydraulic fractures. Mainly using an analytical solution for the surface displacement due to a horizontal penny-shaped fracture, I discuss a method to determine the source parameters from surface deformation measurements, and present a measure to evaluate the applicability of deformation monitoring for investigation of hydraulic fractures.

ACKNOWLEDGEMENTS

I would like to express my sincere appreciation to my supervisor, Dr. Edo Nyland, for his guidance and patient assistance during this study.

I would like to thank Dr. M. B. Dusseault for his contributions of useful information and suggestions, and for his reviewing this work.

I am indebted to The Japan Petroleum Exploration Co., Ltd. (Tokyo, Japan) for providing financial support throughout the course of this work since late January in 1980. Most of all, I heartly thank Dr. T. Tamano, General Manager of The Geophysical Headquarters, who has given me this opportunity to study in Canada for more than two years. I furthermore wish to thank all my superiors, who agreed with this project, and arranged the laborious procedures required for my study abroad. I also wish to extend my appreciation to all my colleagues for their assistance during my long-term absence from the office.

I thank Dr. D. Rankin, Dr. T. Asada and Dr. Y. Nabetani for all helping me start this study at this university.

In this thesis, I quote many arguments and figures from references on valuable studies relating to hydraulic fracturing. Here, I would express my gratitude to the authors of those references.

List of Tables

Table	Description	Page
2.1.1	The major content of the past field experiments in which surface deformation measurements were used to investigate hydraulic fractures.	39-41
2.2.1	Tabulation of the function F and G in Eq.2.2.27 (from Paris and Sih, 1965).	56
2.3.1	Stress intensity factors for a horizontal penny-shaped fracture (from Kassir and Sih, 1975, p225).	77
3.1.1	Estimates of the amplitude factor of the surface deformation due to a horizontal penny-shaped fracture, based on Eq.3.1.9.	93
3.2.1	Dependence of computation of surface displacements due to a rectangular fracture on spacings of points in numerical integration.	97
3.2.2	Cross-correlations of two displacement fields resulting from different values of the size parameter b.	101
3.2.3	Variation of the maximum amplitude of surface displacements with changes of the size parameter b.	103
4.3.1	$\sigma_q(a_o, a_o-\Delta a, \tilde{J})/\sigma_q(a_o, a_o-\Delta a, J=10)$	129
4.3.2	$\sigma_q(a_o=0.4, a_o-\Delta a, J)$	137
4.3.3	Estimates of the upper limit of noise-level to attain a resolution of ±20 meters for the radius of fracture.	137
4.3.4	The optimum and minimum acceptable measurement configurations.	139

List of Figures

Figure	Description	Page
2.1.1	An example of pressure history during a hydraulic fracturing operation (from Ren Jen Sun,1969).	18
2.1.2	Examples of calculated and surveyed uplifts (from Ren Jen Sun,1969).	18
2.1.3	Examples of surface uplift, extent, and thickness of injected grout sheet (from Ren Jen Sun, 1969).	20
2.1.4	Examples of surface tilt changes during steam injection operations (from Holzhausen et al., 1980).	26
2.1.5	Examples of records of wellhead pressure and tilt response at a measurement site during steam injection operations (from Holzhausen et al., 1980).	27
2.1.6	Examples of surface tilt changes due to nitrogen gas injection (from Evans et al., 1980).	32
2.1.7	Examples of surface tilt changes due to (a) hydraulic fracturing operations and (b) an explosive injection (from M.D.Wood Inc., 1980).	37
2.2.1	A cylindrical cavity subjected to far-field stresses.	44
2.2.2	A cylindrical cavity subjected to an internal pressure.	44
2.2.3	Schematic diagram of (a) hydraulic fracturing set-up and (b) associated boundary stress assumed by Kehle.	48
2.2.4	Vertical and tangential stresses induced at the wall of the hole due to stresses in Fig.2.2.3. (from Kehle, 1964).	48
2.2.5	Crack in a borehole wall subjected to far-field stresses and internal pressure.	55
2.2.6	I(α) defined by Eq.2.2.28 for different	

ratio of L/a. (from Abou-Sayed et al., 1978). 55

2.2.7 The Mohr diagram in 2-D. 59

2.2.8 The Mohr diagram in 3-D. 62

2.2.9 Mohr diagrams for discussion of (a) failure in a plane of weakness and (b) failure through a body. 63

2.3.1 Stress intensity factors at the edge of an infinitely long (2-D) fracture subjected to a uniform internal pressure. (a)= a vertical fracture (b)= a horizontal fracture (from Pollard et al., 1979). 70-71

2.3.2 Interpretation of signs of stress intensity factors and propagation directions of a fracture. 73

2.3.3 Stress intensity factors for horizontal fractures subjected to uniform and linear pressure distributions. (from Pollard et al., 1979). 75

2.3.4 Skewed crack under far-field stresses and internal pressure. 78

2.3.5 Orientation of an extending crack which maximizes energy release rate (from Abou-Sayed et al.,1978). 78

3.1.1 Surface deformation fields due to a horizontal penny-shaped fracture. 85

3.1.2 The amplitude of extrema of the surface deformation due to a horizontal penny-shaped fracture. 87-89

3.1.3 The location of extrema of the surface deformation due to a horizontal penny-shaped fracture. 92

3.2.1 The geometry of model fractures. 96

3.2.2 Variation of the shape of displacement fields in terms of a change of a size parameter of a rectangular fracture. 99

3.2.3 Surface deformation fields due to an inclined penny-shaped fracture with a dip-angle 60 degrees and characterized by a constant displacement dislocation. 104

3.2.4 Variation of surface displacements due to an inclined penny-shaped fracture with various dip-angles. 105-106

3.2.5 Difference of surface displacements resulting from different dislocation distributions, constant and linear symmetric. 108

3.3.1 Surface deformation fields due to an inclined rectangular shear fault model. 111

4.2.1 The least-squares error as a function of an unknown non-linear parameter a. 117

4.2.2 Two polygons with "similar" shape. 120

4.3.1 $\sigma_T(a_o,a,J)$ 123

4.3.2 Schematic diagram of $\sigma_g(a_o,a,J)$ showing its dependence on the number of measurement points, J. 123

4.3.3 The curve of $\sigma_g(a_o,a_o-\Delta a,J)$ as a function of J. 126-128

4.3.4 Difference of resolution factors b resulting from changes of J. 129

4.3.5 The curve of $\sigma_g(a_o,a,J)$ as a function of a. 132-136

4.3.6 Models of measurement point configuration. 138

4.3.7 The amplitude factor as a function of an unknown parameter a, normalized the true value of the amplitude facture, $\mathring{f}$. 141

4.4.1 Resolution resulting from data P alone, Q alone and the combination Z=P+xQ. 147

4.5.1 Schematic diagram showing convergence of f in iterative computations. 153

4.6.1 Parameters defining geodetic measurements and displacement vectors at the points (i) and (j). 158

Table of Contents

Chapter Page

1. Introduction 1
   - 1.1 Measurement and Analysis of Ground Deformation 2
   - 1.2 Source Models in Volcanism and Seismology 5
   - 1.3 Previous Field Work 8
   - 1.4 Plan of the Thesis 15
2. The Behavior of Hydraulic Fracture 16
   - 2.1 Previous Field Experiments Utilizing Deformation Measurements 16
   - 2.2 Inception of Hydraulic Fracture 42
   - 2.3 Fracture Orientation Changes 66
3. Theoretical Size of Surface Deformations 81
   - 3.1 A horizontal penny-shaped fracture 81
   - 3.2 An Inclined Fracture 95
   - 3.3 A Shear Fault Model 110
4. Determination of Source Parameters of a Horizontal Penny-shaped Fracture 113
   - 4.1 Basic Procedure 113
   - 4.2 Resolution - Basic Concept 114
   - 4.3 The Resolution Related to the Model Functions g ..121
   - 4.4 S/N Enhancement by Combination of Two Kinds of Data 143
   - 4.5 Determination of Time Varying Fracture Parameters 148
   - 4.6 Observation Equations for Geodetic Measurements ..158
5. Conclusions 162
6. Bibliography 167

1. Introduction

Since its introduction to the petroleum industry (Clark, 1949), the technique of hydraulic fracturing has been applied as a tool for underground waste disposal, geothermal energy recovery, solution mining and in-situ bitumen recovery from oil sands and oil shale deposits as well as for conventional oil/gas reservoir stimulation. The technique has received a considerable amount of theoretical and experimental attention. Unfortunately, the analysis of the behavior of induced fractures is still inadequate. The difficulty is that the form of the fracture depends on several variables such as the interaction between the properties of injection fluid and the properties of the formation rock, the strength characteristics of the reservoir materials, the in-situ stress state, the initial pore pressure and the fluid penetration, and the pre-existing fractures and zones of weakness.

Hydraulic fracturing in a project should be designed to create fractures of a desired form for the particular purpose. The form of the fracture, especially its orientation and size, is crucial. Nevertheless there have been few cases in which the form of induced fractures could be well determined. One of the biggest problems in the application of hydraulic fracturing relates to the methods for the determination of the size and orientation of fractures. Geophysical techniques involving surface measurement of physical quantities and their changes associated with hydraulic fracturing are required. Any technique sensitive to the presence of fractures should be considered. The feasibility of seismic and acoustic measurements, ground deformation monitoring and electric potential measurements have been evaluated by field experiments, but the number of the experiments with published results is quite small. Here I discuss the use of ground deformation measurements.

1.1 Measurement and Analysis of Ground Deformation

The value of ground surface deformation measurements for the determination of quantitative details of fracture implies the detectability of small magnitude surface deformation and methods for the analysis of the resulting data. Accurate measurements with high resolution instruments and construction of a tractable, realistic fracture model are the minimum requirements.

Even if surface deformations are measured accurately by high resolution instruments, this does not imply the detection of the surface deformations due to the fluid injection into the subsurface. The earth is not [illegible] stationary but a deformable body which changes in internal structure and shape by natural and induced forces. The types of surface deformation are multifarious in terms of time scale, spatial extent and magnitude. The extraction of the signals from the fluid injection operation can not be attained without suppression and estimation of the background noise and proper data processing for the signal enhancement.

The major noise which should be taken into consideration for the extraction of the signals from the fluid injection is caused by tides and meteorological effects such as diurnal thermal strain, wind, barometric fluctuation and moisture change, and the near-surface enviroments such as the machinery for injection operation and fluctuating aquifers. Only some of them are periodic and predictable. (Wyatt and Berger, 1980; Savage and Prescott, 1973).

Hydraulic fracturing is not always accompanied by permanent deformation of the ground surface. The period of the fluid injection operations usually ranges from several tens of minutes to a few hours, or a few days. The measurements are required to follow relatively short time phenomena.

In order to analyze the observed surface deformation, we assume a mathematical fracture model, and we need to understand the theoretical ground deformation due to the model fracture. There are two ways to characterize the subsurface deformation. In one of them the subsurface deformation is characterized by the displacement dislocation, and the other assumes the forces acting in the region of subsurface deformation. The complexity of real subsurface deformations makes it difficult to suggest how the distribution of the displacement dislocation or the forces should be modelled. Surface deformation associated with fluid injection has not yet been studied sufficiently that a strict fracture model can be constructed.

We need a tractable and realistic crack model in order to start the solution of this problem. Even if the crack is assumed to have simple shape characterized by uniform forces or constant displacement dislocation in an idealized elastic earth model, analytical solutions exist only for a limited number of symmetrical geometries (e.g., Sih,1973; Kassir and Sih,1975), and even those are complicated. These solutions all have a singularity, a stress concentration of infinity, at the crack tip, which probably plays an important role in the propagation of the fracture but is physically impossible. Therefore the assumption of the displacement or stress conditions should be reconsidered to make the crack model more reasonable. For more complex crack models, numerical approaches are naturally required. It is also important to understand how much the theoretical surface deformation fields from the simple crack model differ from the alternative model which takes into consideration such a physically impossible situation, and how well the surface deformation delineates the changes of the source parameters of fracture.

There have been few hydraulic fracturing experiments where ground deformation was measured and the results published. The reason for this seems to be the difficulty of constructing a tractable, realistic crack model and of developing the techniques for field measurements.

1.2 Source Models in Volcanism and Seismology

There have been several source models applied to the analysis of surface deformation associated with volcanism. Yamakawa (1955) and Fukuda (1944) assumed spherical models. Walsh et al. (1971) studied a semi-infinite line source model. Davis et al. (1974) used an ellipsoidal, anelastic source model for the interpretation of the Kilauea's observation. Dietrich et al. (1975) calculated the surface displacements due to a variety of volcanic source shapes by finite elements analysis. Swanson et al. (1976) applied the above five different models to the observations around Kilauea's rift and compared the results. Koide et al. (1975) discussed formation of fractures around magmatic intrusions. Lachenbruch (1961) analyzed natural extension fractures which initiate at the surface and propagate downward.

In seismology, elastic theory of dislocation demonstrated the equivalence of small shear dislocation and the double-couple force, the so called body force equivalence (Steketee,1958; Maruyama,1963; Burridge and Knopoff, 1964), and then brought a significant advance with regard to the elucidation of seismic source mechanism. The relation of seismic source to shear fault movement has been substantiated by many observations. Many earthquakes have been described in terms of the time and spatial parameters of such seismic fault models, (cf., Yonekura, 1978). It is furthermore noted that surface deformations and seismic radiation have been explained quite reasonably by this rather simple model.

Basic mathematical treatments of elastic theory of dislocation for the calculation of surface deformation were presented by Steketee (1958) and Maruyama (1964). Analytical solutions for simple shear fault models with uniform displacement dislocation on a plane were derived by Chinnery (1960), who assumed a two-dimensional, vertical, strike-slip fault, Press (1965), who analyzed a vertical, rectangular fault model with dip and strike-slips (and published incorrect results), and Manshinha and Smylie (1971), who took account of arbitrary dip-angle of a rectangular fault plane. The static deformation field due to dislocation in a multi-layered medium has been studied by Sato (1971) and Sato and Matsuura (1973, 1974, 1975). Nyland (1971) discussed body force equivalents as sources of anelastic processes. Other references are found in articles of Ben-Menahem and Singh (1969, 1970).

Several attempts have been made to interpret static displacement fields due to the occurrence of an earthquake in terms of a dislocation function varying along a complex fault surface. In those analyses, the dislocation function has been determined by using the method of linear inversion, the least-squares procedure or the finite elements modelling, under an assumption that the other presupposed fault parameters are adequate. The reliability of the estimated results depends strongly on that of the presupposed fault parameters. (Savage and Hastie,1966; Canitez and Toksoz,1972; Mikumo,1973; Jungles and Franzier,1973; Alewine and Jordan,1973; Nyland,1973, 1976; McCowan et al.,1977; Miyashita and Matsuura,1978).

Earthquakes represent failure of geological materials to resist tectonic stress. The stress is accumulated over a period of time, and must be accompanied by deformation and straining of rock. Laboratory experiments and theoretical considerations predict that a change in the strain rate should precede the failure. Therefore, it is a crucial subject for earthquake prediction to monitor the temporal and spatial extent as well as the magnitude of the changes in the strain rates preceding earthquakes.

The value of the deformation measurement is also found in the fact that a substantial part of the faulting associated with earthquakes takes place too slowly to be detected by most seismometers. There is the further possibility that slow and 'silent' earthquakes may result in significant displacements, and anelastic processes following earthquakes may strongly affect the stress enviroment. These phenomena would be accompanied by episodic ground displacements that might not be much smaller than those associated with seismic events. Geodetic monitoring of tectonic deformation has been conducted in various forms, for example, the monitoring of long-term strain accumulation patterns and rates, medium-term episodic strain changes as the preparatory phase of an earthquake, the detection of short-term strain changes just prior to its fault movement, and the observation of postseismic deformation as the relaxation process of regional and local stress patterns. Not only the measurement of local strain accumulation and release in and around seismic active zones but also global tectonic deformation monitoring play a great role in the study of the dynamics of the earth interior. (NRC, 1981; Nyland,1977; Thatcher, 1979; Savage et al.,1981; J.G.R Vol.85,No.B4,1980).

The interaction of a fracture and a free surface has been studied also in the field of fracture mechanics; e.g., Sih (1973), Erdorgan et al.(1974). Stress intensity factors on the fracture periphery are of much interest in fracture mechanics, and stresses and displacements on the free surface are not given generally.

1.3 Previous Field Work

I refer to four field experiments; (1) Ren Jen Sun, 1969, (2) Holzhausen et al.,1980, (3) Evans et al.,1980 and (4) M.D.Wood. Inc.,1979, in which the behavior of hydraulic fractures was analyzed by using the surface deformations measured by either levelling or borehole tiltmeters.

Previous field experiments suggest that fluid injection into the subsurface certainly causes surface deformations, and furthermore demonstrate that the measurement of surface deformations can provide an indication of the overall geometry of hydraulic fracture and reflect major changes in the facture behavior such as a change in propagation direction (e.g., from vertical to horizontal) or cessation of growth resulting from intersection of pre-existing natural joint or fissure.

The magnitude of the measured surface deformations is large enough compared with the resolution of the instruments and the survey accuracy. The tiltmeter surveys reported that tilt changes of ground surface are on the order of 0.1-2.5 microradians, (cf., (2), (3) and (4)), whereas the resolution of the tiltmeters used for the field experiments is order of 10^{-2} - 10^{-3} microradians. The uplift survey in one of the field experiments reported maximum surface uplifts of 4-12 mm. (cf., (1)). Unfortunately, the specification of the levelling surveys is not clear. Probably the best attainable measurement accuracy of levelling survey is estimated by 4mm x (line length in km)$^{0.5}$.

The period of the fluid injection operations ranged from several tens of minutes to several hours, and for one case, (2), it was as long as about 40 days. Even if a fracturing operation was conducted over a long term, ground responses were reported to be characterized by several short-term events which suggest the repetition of growth and collapse of a fracture. The areal size of surface deformation around the well is estimated to be roughly 2-3 times of the injection depth (180-350 m). As a reference, the calculated size of the fractures ranges from one-fourth to half of the injection depth in most cases. Although results have not published, the tiltmeter surveys are reported to have been conducted for hydraulic fracturing as deep as 3000m. (M.D.Wood.Inc., personal communication).

Surface deformation in the previous experiments was measured by levelling or by tiltmeters. The previous tilt surveys consisted of at most nine borehole tiltmeters, eight of which were installed in a circular array from the well at a radius of half the injection depth. The number of the tiltmeters used does not seem to be sufficient.

In order to measure complex surface deformation more exactly and delineate the fracture behavior more clearly, we need to incorporate more observations of the measurable quantities. On the other hand, we have to examine the techniques of the measurement from the aspect of the relation between the the accuracy of each survey and the predicted magnitude of surface deformation, the measuring efficiency and the sensitivity of each measurable quantity to the form of the fractures. We could use optical or laser levelling, surface laser ranging and spaceborne laser ranging for the displacement measurements. The disadvantage of these surveys is the difficulty of continuous operation. For strain measurement, several strain meters are available, such as long baseline Invar wire or fused quartz rod strain meter. For tilt measurement, several types of tiltmeters are available. In addition to tilts and uplifts, measurements of horizontal displacements and strains might be useful and should be considered.

The mathematical fracture model so far used for analysing the observed surface deformations is either a horizontal penny-shaped model, (Sun, 1969), or a two-dimensional inclined model, (Pollard et al., 1979). Both models assume a plane fracture subjected to a uniform internal pressure in an idealized earth such as a semi-infinite, homogeneous and isotropic, linear elastic medium. In spite of the simplification, analyses of the observed surface deformation led to the plausible conclusions about the fracture behavior. The two-dimensional inclined fracture model was applied to one fracture among sixteen fractures whose corresponding surface deformations were analysed quantitatively in the previous field experiments.

In one of the field experiments, (Sun, 1969), the radius of the fractures was estimated from the volume of the injection fluid. For such an estimate of fracture radius, the values of the elastic constants and the internal pressure should be known, and an assumption about the impermeability of surrounding rock should hold true. Such analysis is not always applicable to all cases. The comparison between the observed and calculated uplifts supports the validity of the mathematical fracture model. The calculation of the fracture size from the observed uplift data, so called "inversion problem", was not discussed at all in this project.

In the other three field experiments with tiltmeter measurements, the size of the fractures was estimated from the observed tilt fields by two methods. The theoretical surface deformation field based on the fracture models is expressed by the product of the quantity given by elastic constants and internal pressure in the fracture and the quantity given by functional relation between the measurement point and the source geometry. The former quantity will be called here "the amplitude factor" of the surface deformation. If the geometric relation between the measurement points and the source allows, we can estimate both of the amplitude factor and the geometric parameters of the fracture from the observed surface responses.

When the induced fracture is regarded as horizontal and penny-shaped, eight tiltmeters installed in a circular array around the injection well, (such site configuration of the instruments has been used in most previous experiments), provide substantially only the tilt responses at one measurement point. In such case, the amplitude factor should be known a priori to permit estimation of source parameters. Nevertheless, the physical quantities which contribute to the amplitude factor are very uncertain. An estimate of the internal pressure in the fracture (driving pressure) is very difficult. The uncertainty of the driving pressure has been overcome by using the concept of stress intensity factor.

Linear elastic fracture mechanics states that a fracture propagates when the stress intensity factor at the fracture tip reaches a critical value (called fracture toughness) of the material. Then we have a relationship between the driving pressure, and radius of the fracture and the fracture toughness of the surrounding rock. It is also a fact that estimation of the driving pressure from the relationship requires a certain value of the fracture toughness and the radius, which are usually unknown and should be calculated from the observations. However, assumptions about the order of the magnitude of fracture size and the fracture toughness gives a rough estimate of the driving pressure. Once the amplitude factor is estimated, it is easy to determine the fracture radius. Except for one example in which the observed wellhead pressures were used for the analysis, there is no application of the wellhead pressure to estimate the driving pressure.

The other method (Evans et al.,1980) for determining the geometric parameters of a fracture was based on the two-dimensional inclined fracture model. The eight tiltmeters installed in a circular array provided information to determine both of the amplitude factor and the geometric parameters such as the strike, dip-angle and length of the fracture. If the observed tilt field is normalized by the magnitude of a reference measurement point, the uncertainty of the amplitude factor is estimated from the absolute magnitude of the measured surface deformations. Once the geometric parameters of the fracture are determined from the relative magnitude of observed tilts, they lead to the amplitude factor. The driving pressure estimated this way is valuable for understanding the pressure distribution in a fracture and the in-situ fracture toughness. This analysis is essential when compared with the previous one which depends heavily on uncertain assumptions.

In the tiltmeter surveys, the surface tilt responses have been monitored relatively densely in time. If the surface deformations had been analyzed in terms of the time history of the radius and driving pressure of the fractures, significant results which delineate the process of fracture growth might have been obtained. As described in Section 2.3, theories of fracture propagation predict that a fracture is not necessarily a plane fracture centered at the injection depth. It seems that, in the previous experiments, the data acquired under the limitation of the small number of instruments and the site configuration did not stimulate the investigators to verify the possibility of those theoretical predictions.

Except for the use of observation wells, most diagnostic tecnologies for the inspection of induced fractures, such as wellbore impression packers, injection of radioactive sand into the fracture for subsequent detection with a well logging tool, lineament analysis, seisviewer imagery, borehole television and post-fracture well temperature logs, suffer the disadvantage that they give, at best, fracture dimensions and orientation at the wellbore only. The fact that past field experiments of surface deformation measurements, somehow or other, delineated the overall size of the fractures is valuable.

1.4 Plan of the Thesis

In this thesis, I first review the four field experiments cited above, and some basic problems of hydraulic fracturing; the initiation and orientation changes of fracture. Next, I discuss theoretical size of surface deformations, using a horizontal penny-shaped fracture model, inclined tensile and shear fracture models. Next, an inversion scheme relating the surface deformations due to a horizontal penny-shaped fracture is introduced. The resolution inherent of this inversion scheme is evaluated against an estimated level of measurement errors. The optimum survey configuration and a possible combination of different observable data are discussed from the point of view of the attainable highest resolution. Assuming that the surface deformations during an injection operation are given by a time function, an effective procedure for the determination of rates of fracture growth is shown.

2. The Behavior of Hydraulic Fracture

First, I refer to four previous field experiments; Ren Jen Sun (1969), Holzhausen et al. (1980), Evans et al. (1980) and M.D.Wood. Inc. (1979), in which surface deformation measurements were used to investigate hydraulic fractures. The major content of these field experiments is tabulated in Table 2.1.1 (at the end of Section 2.1). In the next two sections, the basic problems of hydraulic fracturing; the initiation and orientation changes of a fracture, are reviewed.

2.1 Previous Field Experiments Utilizing Deformation Measurements

(1) Ren Jen Sun (1969)

Hydraulic fracturing experiments were conducted at ORNL (Oak Ridge National Laboratory, Tennessee) from 1960 to 1965 to evaluate the feasibility of disposal of radioactive waste by injecting grout mixtures into a shale formation. Through the experiments, the theoretical size of hydraulically induced fractures was compared with field measurements of the surface uplifts. ORNL is located in the Appalachian belt of faulted and folded Paleozoic rocks. All the injections were made into the lowermost unit of the Conasauga shale formation, which is about 300 m thick.

The experiments consisted of seven injection operations and five uplift surveys. The behavior of one of the induced fractures is as follows. The injection was made through a slot in the casing at a depth of 285 m. The estimated overburden pressure at the injection depth is 7.57 MPa. Fracturing was initiated with water. The fracturing started at 10.39 MPa of pressure at the surface, then the pressure fell quickly to 9.31 MPa at a pumping rate of 0.57 m^3/min. and increased to 11.27 MPa as the rate was increased slightly. Six minutes after the fracture was started, by which time 3.2-3.4 m^3 of water had been pumped, the pressure in a nearby observation well, 9 m west of the injection well, suddenly rose to 5.49 MPa, indicating that the fracture had extended into it. After the pump was stopped, the water was bled back out of the injection well, and the pressure in the observation well fell to 2.45 MPa in about 100 minutes. The main injection of water-cement-bentonite mixture was then started. The mixture consisted of 346 m^3 of grout containing 201 tons of cement and 5700 kg of bentonite clay. The maximum pressure for the slurry injection was 15.88 MPa. About 40 minutes after the injection started, the pressure dropped to between 11.76 and 12.05 MPa.

The history of pressure during the injection is shown in Fig.2.1.1. The fact that the injection pressure was, in all cases, greater than the formation overburden pressure, indicates the occurence of horizontal fracture. Study of cores made after grout injections also showed that the fractures were concordant with the nearly horizontal bedding. Fig.2.1.2 shows the calculated and observed surface

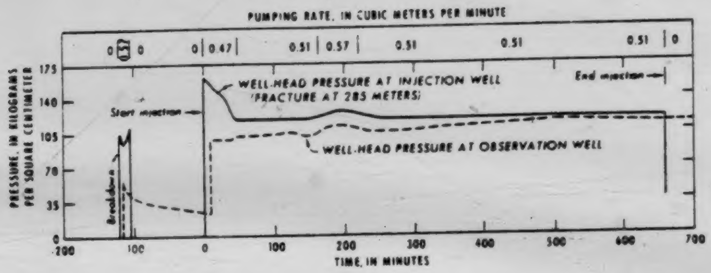

Fig.2.1.1 ..... An example of pressure history during a hydraulic fracturing operation (from Ren Jen Sun, 1969).

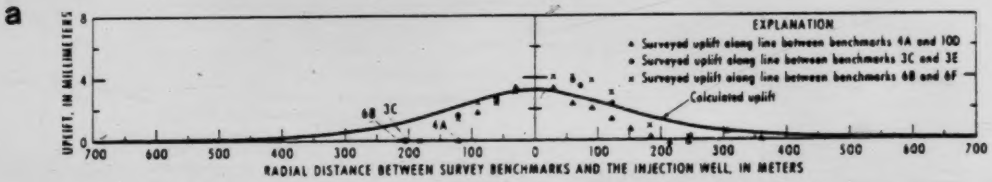

Fig. 7. Calculated and surveyed uplift produced by injection 1, second experiment, September 3, 1960.

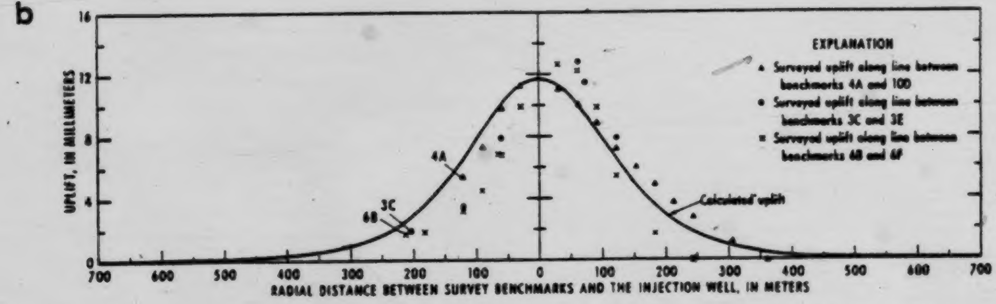

Fig. 8. Calculated and surveyed uplift produced by injection 2, second experiment, September 10, 1960.

Fig.2.1.2 ..... Examples of calculated and surveyed uplifts (from Ren Jen Sun, 1969).

uplifts. Fig.2.1.3 shows the observation geometry, the measured surface uplift and the extent and thickness of the injected grout sheet obtained from core-hole data for two cases of the experiment.

The calculation of the theoretical uplift is based on a mathematical model of a horizontal penny-shaped fracture internally pressurized by fluid injection. For the model fracture in an infinite isotropic and homogeneous, impermeable, linear elastic medium, the fracture radius, a, can be calculated from the internal pressure P, the total volume of injection fluid Q and elastic constants, say Young's modulus E and Poisson's ratio ν , by the relation

$$a = \left\{ \frac{3EQ}{16(1-\nu^2)P} \right\}^{1/3} \qquad (2.1.1)$$

The separation of the fracture walls is found to be

$$\frac{8P(1-\nu^2)}{\pi E}(a^2 - r^2)^{1/2} \qquad (2.1.2)$$

where r is distance from the center of the fracture. The maximum separation B occurs at r=0, and is found to be

$$B = \frac{8P(1-\nu^2)}{\pi E} a \qquad (2.1.3)$$

In order to use Eq.2.1.1 and Eq.2.1.3 for the calculation of the radius and maximum separation of the fracture formed under the ground surface, it is necessary to take account of the effect of the free ground surface. It has been, however, found that the influence is only 2-3 percent if the radius of fracture is less than one half of

6006 REN JEN SUN

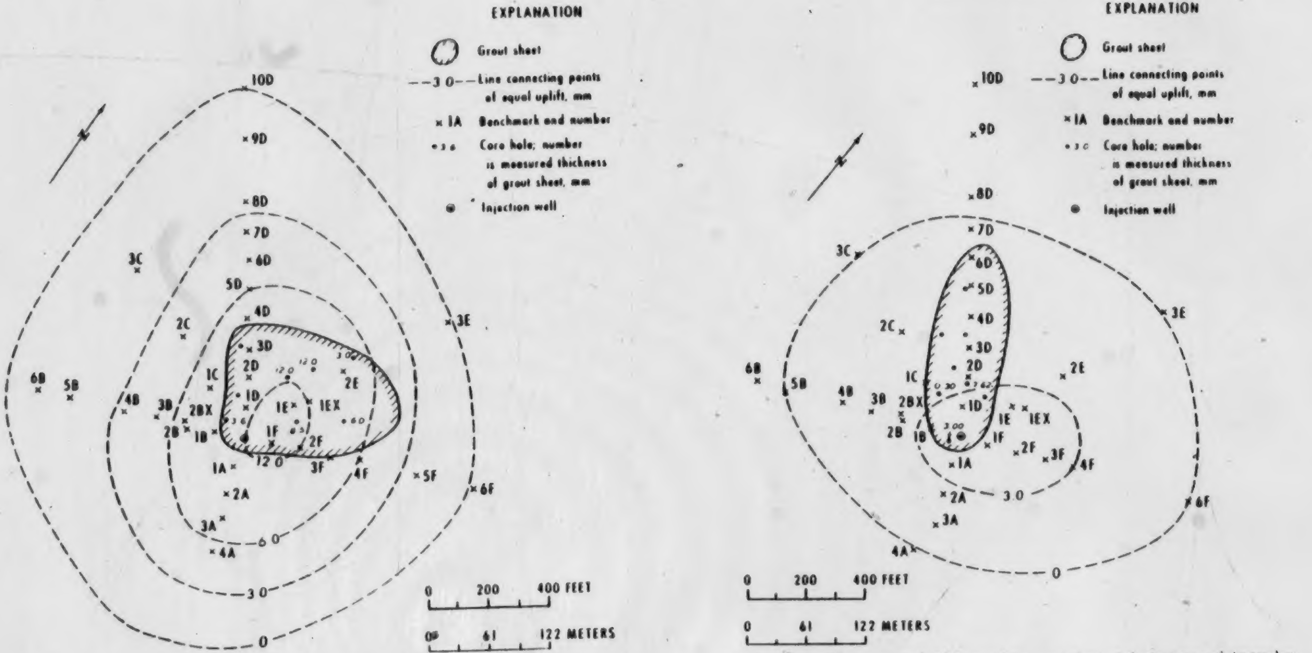
EXPLANATION
Grout sheet
--3 0-- Line connecting points of equal uplift, mm
× 1A Benchmark and number
• 3 0 Core hole; number is measured thickness of grout sheet, mm
Injection well
0 200 400 FEET
0 61 122 METERS
10D
9D
8D
7D
6D
5D
4D
3D
2D
1D
1C
2C
3C
6B
5B
4B
3B
2B
2BX
1B
1A
2A
3A
4A
1E
1EX
2E
3E
1F
2F
3F
4F
5F
6F
3 0
6 0
12 0
0

Fig. 6. Surface uplift, extent, and thickness of the grout sheet of the injection of September 10, 1960 [after *DeLaguna et al.*, 1968, and W. DeLaguna (written communication, ORNL, June 10, 1968)]

b

Fig. 5. Surface uplift, extent, and thickness of the grout sheet of the injection of September 3, 1960 [after *DeLaguna et al.*, 1968, and W. DeLaguna (written communication, ORNL, June 10, 1968)].

a

Fig.2.1.3 ..... Examples of surface uplift, extent, and thickness of injected grout sheet (from Ren Jen Sun, 1969).

the depth of fracture, and is almost zero if the radius is less than one fifth of the depth (Sun, 1969).

The fracture model from which Eq.2.1.1 derives ignores the effect of cohesive forces near the edge region of a fracture on the stress and strain field. The fracture model yields an infinite tensile stress at the edge of the fracture. A more realistic value for the radius of a fracture should be derived from fracture models which take account of cohesive forces and finite tensile stress at the edge of the fracture.

One of the modifications of Eq.2.1.1 comes from the fracture model proposed by Barenblatt (1962). In his concept of a fracture, the fracture is divided into two regions. In the inner region (radius a), the opposite faces of the fracture are relatively far apart, hence there is no molecular interaction between them. In the edge region (radius a to a'), they are sufficiently close to each other so that there are cohesive forces between them. For the mathematical simplification of the problem, it is assumed that: 1) The width of the edge region of the fracture is small when compared with the size of the whole fracture, and, 2) When the fracture extends, the shape of the section normal to the fracture surface in the edge region does not depend on the pressure in the fracture and is always the same for a given material under given conditions of temperature and overburden pressure.

Under the particular case in which the forces of cohesion are small enough and may be neglected when compared with the overburden pressure and the injection pressure P_0, the following relation is found.

$$\alpha = a / a' \qquad (2.1.4)$$

$$(1 - \alpha^2)^{1/2} = (P_0 - \rho g h) / P_0 \qquad (2.1.5)$$

where ρ is density of overburden material, g is gravitational acceleration and h is depth. Then, the average pressure over the entire circular area of radius a' can be assumed as $\alpha^2 P$, where $P = P_0 - \rho g h$. In this case, Eq.2.1.1 and Eq.2.1.3 are modified in the form

$$a' = \left\{ \frac{3EQ}{16(1 - \nu^2)\alpha^2 P} \right\}^{1/3} \frac{1}{\alpha} \qquad (2.1.6)$$

$$B = \frac{8(1 - \nu^2)}{\pi E} \alpha^2 P \qquad (2.1.7)$$

(Sun, 1969, Eq.19 and Eq.20).

The theoretical surface deformations of this fracture model can be expressed by the product of the maximum separation (B of Eq.2.1.3 or Eq.2.1.7) and a quantity which depends only on geometric parameters, such as observation coordinates, the depth and radius of the fracture. For convenience, the fracture model in which the magnitude of surface deformations is calculated in terms of B defined by Eq.2.1.3 will be called "the first model", and the other model related with Eq.2.1.7 will be called "the second model".

The calculated surface uplifts in Fig.2.1.2 are based on "the second model". Comparison between the calculated and the observed uplifts supports the validity of the mathematical fracture model. Fig.2.1.3b shows that, while the cored grout sheet has a nearly circular shape, the injected grout moved generally toward the north-east. In the other experiment shown in Fig.2.1.3a, the grout sheet has an elliptical shape, the movement of the grout sheet is greater, and no correlation can be found between the shape of the grout sheet and the pattern of uplift. The maximum thickness of the grout sheets measured in cores is much less than the calculated values. For example, the theoretical value for the case of Fig.2.1.3a is 7.92 cm and the observed thicknesses are on the figure. The discrepancy between the measured and calculated thicknesses was interpreted as due to the fact that the liquid phase of the injected slurry had been squeezed out and the soild phase had been compacted by the overburden pressure.

(2) Holzhausen et al. (1980)

A second example is the initial cycle of steam stimulation project of Canada Gulf Resources (1979) conducted in the Athabasca oil sands region, Alberta, Canada. The hydraulic fracturing was carried out over a depth interval of 308-317 m of an injection well in the Cretaceous McMurray Formation. The ground deformation was measured with a circular array of eight tiltmeters at a radius of 122 m from the well and an additional tiltmeter installed 610 m from the well. These nine tiltmeters were installed in shallow boreholes less than 7 m deep. The tiltmeters measure tilts in two perpendicular vertical planes, and have a resolution of 5x10^{-3} microradians and a range of 5x10^{4} microradians.

The hydraulic fracturing was initiated three times by cold-water injection. The fracture caused by the injection was interpreted as vertical because the fracture propagated at downhole pressures of about 5.6 MPa whereas the minimum possible value of overburden pressure was about 6.0 MPa.

After the cold-water injection, steam injection took place and continued intermittently for about 40 days. Ground deformation during this phase occurred episodically over periods of a fraction of an hour to a few hours. Gradual, long-term changes, resulting from the increasing volume of injected fluids and thermal expansion of the formation, were reported to prove less distinguishable and less diagonostic of formation response than the episodic short-term changes, which were called "events".

The short-term events were typically preceded by gradual increase of wellhead pressure over periods ranging from several hours to more than one day. After the wellhead pressure rose up to a peak value (8.0-9.4 MPa), it fell rapidly, reaching a minimum (6.7-7.9 MPa) within a few hours and then rising again gradually. The tilt response during each of the events first changed rapidly as pressure dropped, then recovered toward its former value. In most cases, the recovery of the tilt field began before that of pressure. The overall tilt changes indicated uplift of the ground surface during the initial pressure drop, followed by subsidence of the surface not in excess of its initial uplift. Eight events among eleven detected during the period of steam injection were analyzed quantitatively. Figs.2.1.4a and b shows the changes of the tilt vectors during the first event and during the eighth event, respectively. Figs.2.1.5a and b show the records of wellhead pressure and the tilt changes at an instrument site during the first event and during the sixth and the seventh events, respectively.

The surface deformation during the steam injection indicated the occurence of horizontal fractures. This was supported by both the radially symmetric uplift of the ground surface and the records of pressure. In any case, the recorded pressure did not drop below the estimated overburden pressure before the beginning of subsidence of the uplifted ground surface.

The transition from the initial formation of a vertical fracture caused by the cold-water injection to the subsequent growth of horizontal fractures was accounted for in terms of thermal expansion of the oil sands during steam injection. "As heating progressed, some vertical expansion of the material should have been possible, whereas horizontal expansion may have been largely suppressed because of the confining effect of the surrounding rock. As

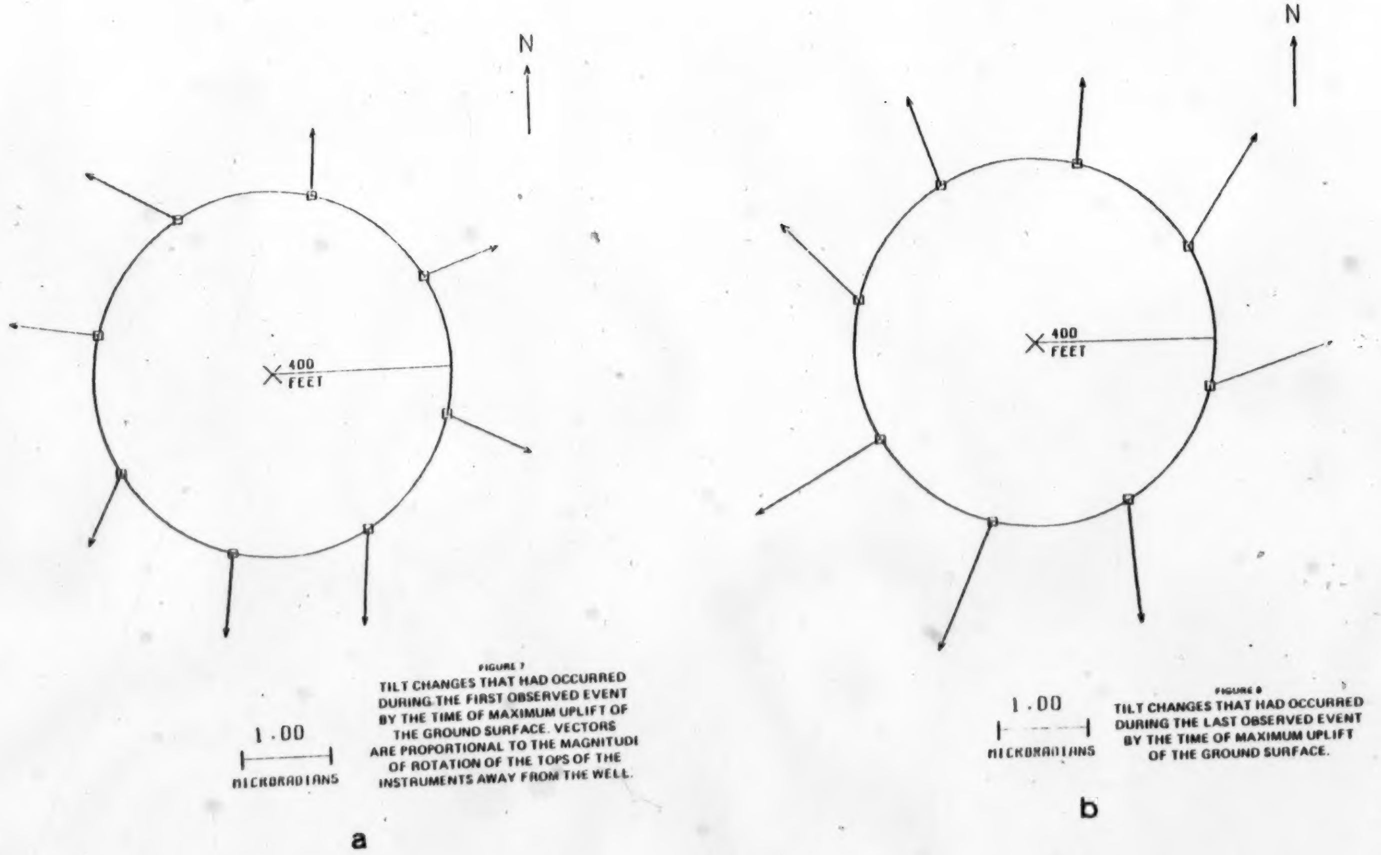
N
N
400 FEET
400 FEET
1.00
MICRORADIANS
1.00
MICRORADIANS
a
b

FIGURE 7
TILT CHANGES THAT HAD OCCURRED DURING THE FIRST OBSERVED EVENT BY THE TIME OF MAXIMUM UPLIFT OF THE GROUND SURFACE. VECTORS ARE PROPORTIONAL TO THE MAGNITUDI OF ROTATION OF THE TOPS OF THE INSTRUMENTS AWAY FROM THE WELL.

FIGURE 8
TILT CHANGES THAT HAD OCCURRED DURING THE LAST OBSERVED EVENT BY THE TIME OF MAXIMUM UPLIFT OF THE GROUND SURFACE.

Fig.2.1.4 ..... Examples of surface tilt changes during steam injection operations (from Holzhausen et al., 1980).

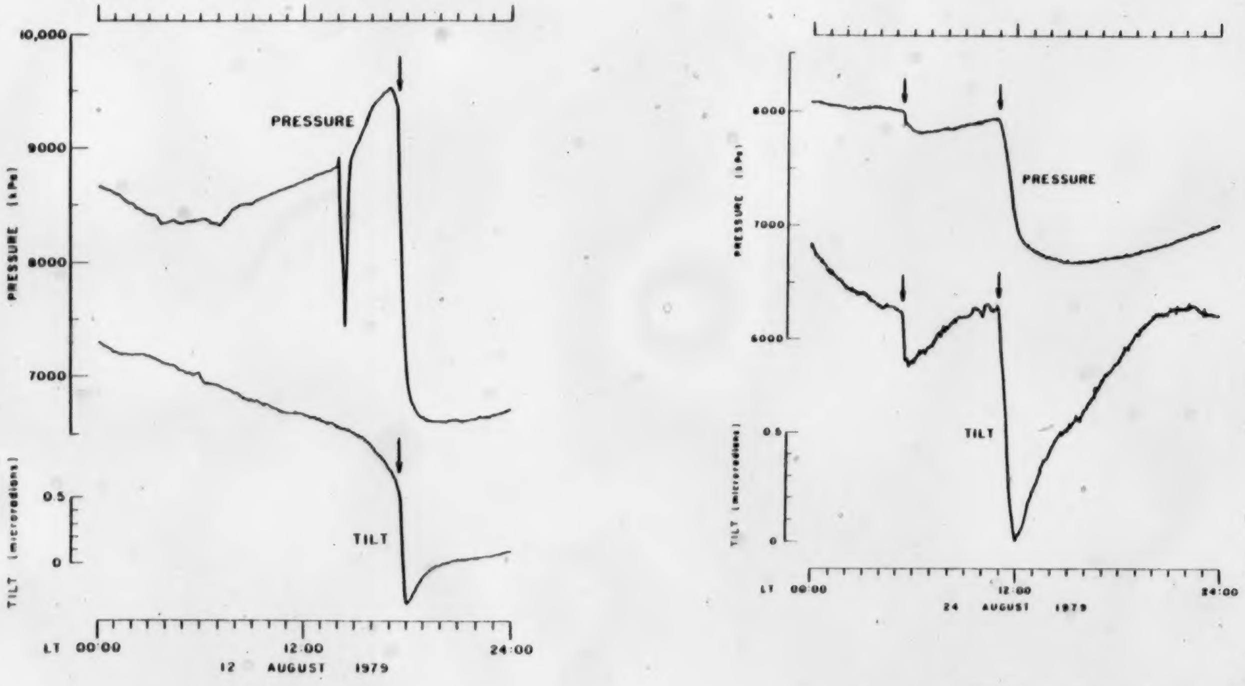

FIGURE 5
RECORDS OF WELLHEAD PRESSURE AND ONE CHANNEL OF TILT DURING THE FIRST OBSERVED EVENT. ARROWS MARK THE START OF THE EVENT. THE LARGE PRESSURE DROP ABOUT THREE HOURS EARLIER WAS CAUSED BY TRIPPING OF THE BOILER BUT HAD NO EFFECT ON THE DEFORMATION FIELD.

a

FIGURE 6
RECORDS OF WELLHEAD PRESSURE AND ONE CHANNEL OF TILT DURING TWO EVENTS THAT OCCURRED WITHIN SEVERAL HOURS OF EACH OTHER ON 24 AUGUST.

b

Fig.2.1.5 ..... Examples of records of wellhead pressure and tilt response at a measurement site during steam injection operations (from Holzhausen et al.,1980).

temperatures increased, this fracture should have been closed by thermal expansion of the oil sands. The resulting horizontal suppression of expansion would lead to an increase in the magnitude of the horizontal in-situ stress components, leaving the vertical stress largely unaffected. It thus seems likely that horizontal fractures began to form when horizontal stresses began to overcome the vertical in-situ compression."

The assumption of impermeable rock does not hold for this test site. Therefore, the radius of fracture can not be estimated from the relationship between it and the total volume of injected fluid, Eq.2.1.1. In fact, it was reported that the capacity of the fractures estimated from the measured tilts was only 0.2-2.8 percent of the injected volume of water-equivalent steam.

Estimates of the radius of the fractures were based on "the first model" for a horizontal penny-shaped fracture. In order to estimate the radius from the observed tilt, the elastic constants and the driving pressure of the fracture should be known. (This statement holds true for this experiment because of the configuration of measurement points and the assumption of the shape of fracture.) For this experiment site, the values of the density of overburden, the injection pressures at the bottom hole and the elastic constants of the surrounding rocks were uncertain. Although the well-head pressures were monitored, it has been thought that estimates of driving pressures vary by factors of four or five even when well head pressures are measured.

The uncertainty of the driving pressure of the fractures was overcome by using the concept of fracture intensity factor and fracture toughness. Linear elastic fracture mechanics states that a fracture propagates when the stress intensity factor at the fracture tip reaches a critical value (Kic, called fracture toughness) of the material. For a penny-shaped fracture in an infinite, isotropic and homogeneous elastic body, the relation between the stress intensity factor Ki, the driving pressure Pd and the radius a is given by

$$K_I = 2 P_d \sqrt{a} / \pi \qquad (2.1.8)$$

(cf., The effect of the free-surface on the stress intensity factor is shown in Section 2.3). When the fracture is in a state of mechanical equilibrium, the stress intensity fractor is postulated to be equal to the fracture toughness. Hence the driving pressure is given by

$$P_d = \pi \cdot K_{Ic} / 2 \sqrt{a} \qquad (2.1.9)$$

The fracture toughness of the oil sands was assumed to be under 330 KPa$\sqrt{m}$ by taking account of the fracture toughness of about 330-1100 KPa$\sqrt{m}$ for most rock. The equilibrium driving pressure just prior to structure collapse was deduced as 35-140 KPa. Moreover, for the calculation of the radius of the fractures presumed to be horizontal and penny-shaped, the shear modulus of the overburden materials was assumed to be between $1.2x10^3$ and $2.6x10^3$ MPa and the Poisson's ratio to be 0.3. The radius of the fractures, respectively distinguished as a short-term event, was estimated by using these possible values of the elastic constants and the driving pressure, and by comparing the magnitude of the measured tilts with the magnitude of the theoretical tilts which vary with variation of the radius of fracture.

(3) Evans et al. (1980)

A third example presents results of a tiltmeter survey conducted in 1979 in order to determine the geometric characteristics of fractures associated with nitrogen gas injection into the Devonian shale in Know Country, Ohio. Bedding of all the formations around the injection well is approximately horizontal, and the shale contains high angle faults of approximate orientation N70°E.

The injection well penetrated to a depth of 341 m, the upper 322 m of which was cased. The casing was perforated between 305-314 m. The total volume of the nitrogen injected during about 28 minutes is 400 m^3 calculated in terms of the gas volume at a temperature of 10.2°C and a gas pressure of 6.205 MPa. Eight tiltmeters were installed in a circular array around the well. A shallow watertable was reported to have contributed significantly to the background noise level of three instruments.

The measured tilt changes are shown in Fig.2.1.6a. From the inspection of the set of tilt waveforms, the tilt event was divided into three phases. The tilt vectors accumulated during each phase are shown in Figs.2.1.6b,c,d. The transition from Phase I to Phase II was identified by a sudden change in the previously consistent tilt rates and directions recorded by all instruments. The onset of Phase II marks a change in the evolution of the fracture growth. Wellbore pressure and flow rate remained undisturbed both during and following the transition.

The observed tilt vectors of Phase I suggest the occurrence of a long, almost vertical fracture. Based upon a two-dimensional model for the free-surface displacements and tilts due to an infinitely long fracture of arbitrary dip, height (length along the dip direction) and depth to center, subjected to a uniform internal pressure, (Pollard et al., 1979), the strike, dip-angle and height of the fracture were estimated. The complex tilt responses of Phase II were not analyzed quantitatively. The transition from Phase I to Phase II was explained by two possible hypotheses.

Fig.2.1.6b shows that the tilt vectors are almost perpendicular to a direction of about N60°E and distributed symmetrically with respect to the strike. The dip angle and the length along the dip direction were determined by comparing the relative amplitudes of the observed and the theoretically predicted tilts. The form of the tilt field is dependent only upon relative fracture geometry. Hence,

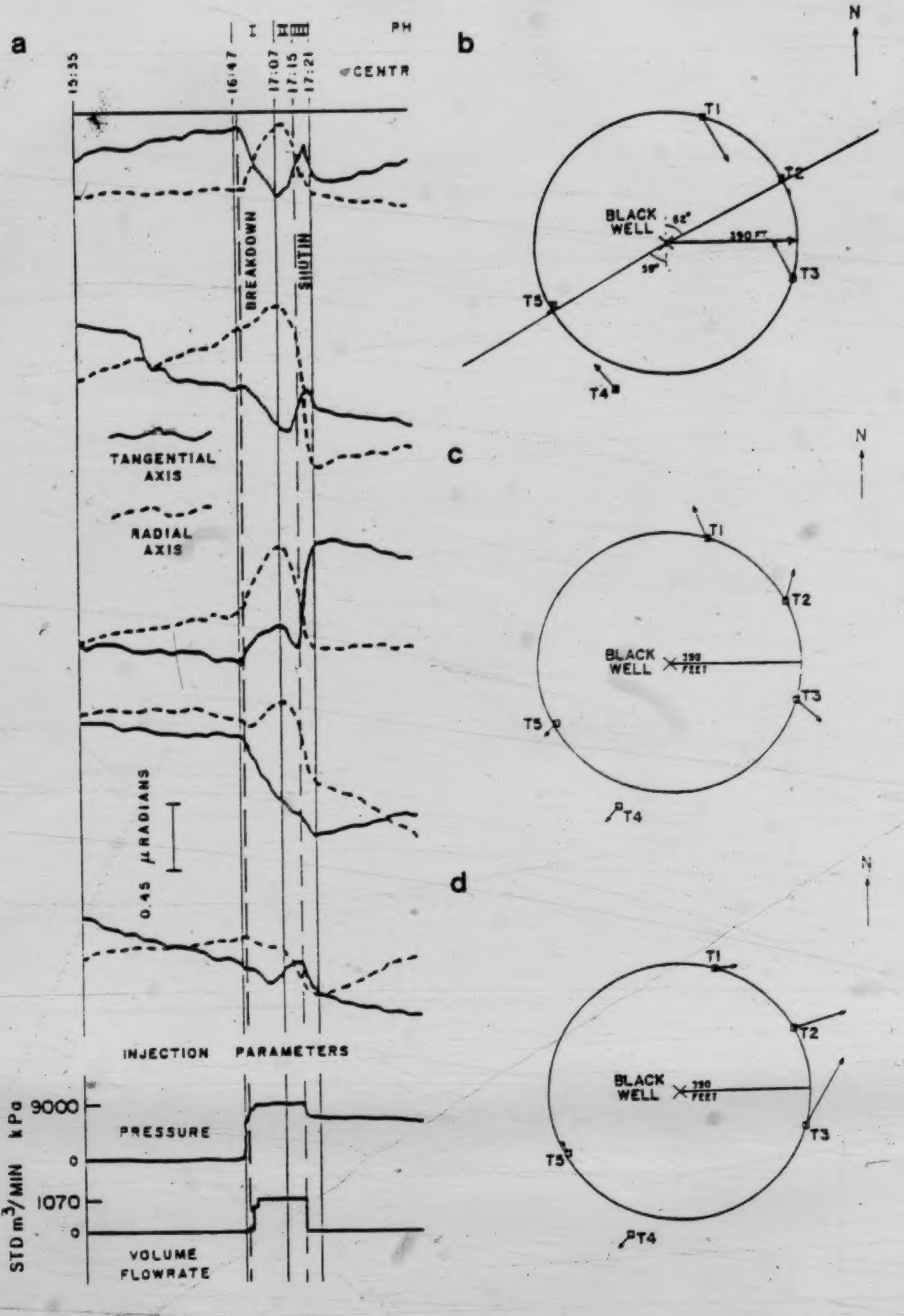

Fig.2.1.6 ..... Examples of surface tilt changes due to nitrogen gas injection (from Evans et al., 1980).

assuming the center of the fracture remains at the depth of injection during growth of the fracture, the height and dip angle of fracture can be estimated from the relative amplitudes of the surface tilts. It was concluded that the observed tilt changes of Phase I could be reproduced almost exactly by a suitable pressurized fracture of half-length 183 m having a dip to the northwest 87 degrees.

The procedure of taking the ratio of the observed tilts to the predicted tilts is used to eliminate the uncertainty of the other unknown fracture parameters, such as driving pressure and elastic constants. Assuming the appropriate bounds on the shear modulus, $6.9x10^{3}$-$17.0x10^{3}$ MPa, and the Poisson's ratio of 0.25, the bounds on driving pressure were estimated as 45-265 KPa. These values are understood to represent the possible range of average pressure operating in the fracture. Initial formation breakdown occurred under modest pumping rates at a downhole pressure of 6.204 MPa, which thereafter increased to 8.962 MPa as a result of some increase of injection rate. Assuming this breakdown pressure is approximately equal to the in-situ stress normal to the fracture plane, a simple computation suggests that a driving pressure of 2.758 MPa acted in the fracture. It is, however, not necessary that such a high pressure extends appreciable distances from the wellbore. Indeed, consideration of the fracture toughness of rock makes it extremely unlike that driving pressures operating near remote fracture edges exceed hundreds of KPa. Consequently, the values of driving pressure deduced from both of the surface tilts and the breakdown pressure suggest that pressure gradients exist in the fracture.

Two hypotheses were presented to explain the transition of the observed tilts. First, a comparison with the tilt vectors of Phase I and II reveals an approximate reversal in trend on instruments located in the northeast quadrant and suggests a partial collapse of the fracture opened during the initial phase. This can be anticipated if the fracture intersects a natural fracture system at the end of Phase I. Also the sharpness of the reversals of the instruments #1, #2 and #3 suggests that this intersection would have occured to the north-east of the wellbore. However, the tilt vectors from instruments #4 and #5 do not conform well to this scheme.

An alternative interpretation is that the fracture ceased to grow vertically at the end of Phase I and instead, flipped over into the horizontal plane. Physically this could occur if there was a major change of the minimum principal stress direction, such as that from horizontal to vertical. The depth, D, at which the change of the principal stress direction is possible was calculated from

$$P_h(z) = P_h(0) + \frac{\nu \cdot z \cdot \Delta P_v}{1 - \nu} \qquad (2.1.10)$$

where Ph(z) is the horizontal principal stress at depth z, $z\Delta Pv$ is the vertical principal stress at depth z, ΔPv is the overburden pressure gradient and ν is Poisson's ratio. At first, Ph(0) is calculated by using the appropriate values of ν , Pv(z)=zΔPv (overburden pressure), Ph(z) (breakdown pressure) and z (injection depth). Next, the depth D is estimated by the relation

$$D = \frac{P_h(0)}{\Delta P_v - P_v \cdot \nu / (1-\nu)} \qquad (2.1.11)$$

which is obtained by substitution of Ph(z)=Pv(z) in Eq.2.1.10. The calculated depth D for this site is 170 m. This value fits well with the result from the analysis of Phase I, that is, the center depth of the nearly vertical fracture is 335 m, and the half-length of the fracture is 183 m. It was also pointed out that this estimated depth places the top of the fracture near a lithologic boundary.

(4) M. D. Wood Inc. (1979)

A fourth example presents the measurement and analysis of surface tilt responses associated with four hydraulic fractures produced in horizontally bedded oil shale formation and a subsequent injection of explosive slurry into these fractures. This field experiment was conducted near Rock Spring, Wyoming, in 1978.

The four hydraulic fractures were produced separately at slightly different depths of 124-118 m in a well during one month. The explosive slurry was injected through four wells, each feeding one fracture, three months after the last hydraulic fracturing operation. The period of each of the hydraulic fracturing and explosive injection operations was on the order of 20-30 minutes. Eight tiltmeters were installed in a circular array at a radius of 48.8 m from the injection well. One instrument was 76.3 m away from the injection well.

The measured tilt changes from the initiation of the fluid injection to the shut-in are shown in Fig.2.1.7a for the hydraulic fracturing, and in Fig.2.1.7b for the explosive injection. The fact that the radial tilt changes, in all cases, are non-uniform indicates that the fractures are not penny-shaped, but have irregular boundaries. From the sense of the radial tilts, each fracture was regarded as horizontal. Whereas the relative magnitudes of the radial tilts differs for the four hydraulic fractures, the overall forms of the tilt fields are much the same, but are considerably different from the form of the tilt field due to the explosive injection.

To make analysis of the measured tilts tractable, the radial tilt changes at eight instrument sites were individually assumed to have been produced by a horizontal penny-shaped fracture. The result is eight different radii for each fracture, which were regarded as an estimate of the fracture boundary. The computation of the radius of the fractures is based upon the same method as one used in the second example cited previously. The value of fracture toughness used in the calculations is 373 KPa$\sqrt{m}$, and the shear modulus and the Poisson's ratio are 3.3×10^3 MPa and 0.16, respectively.

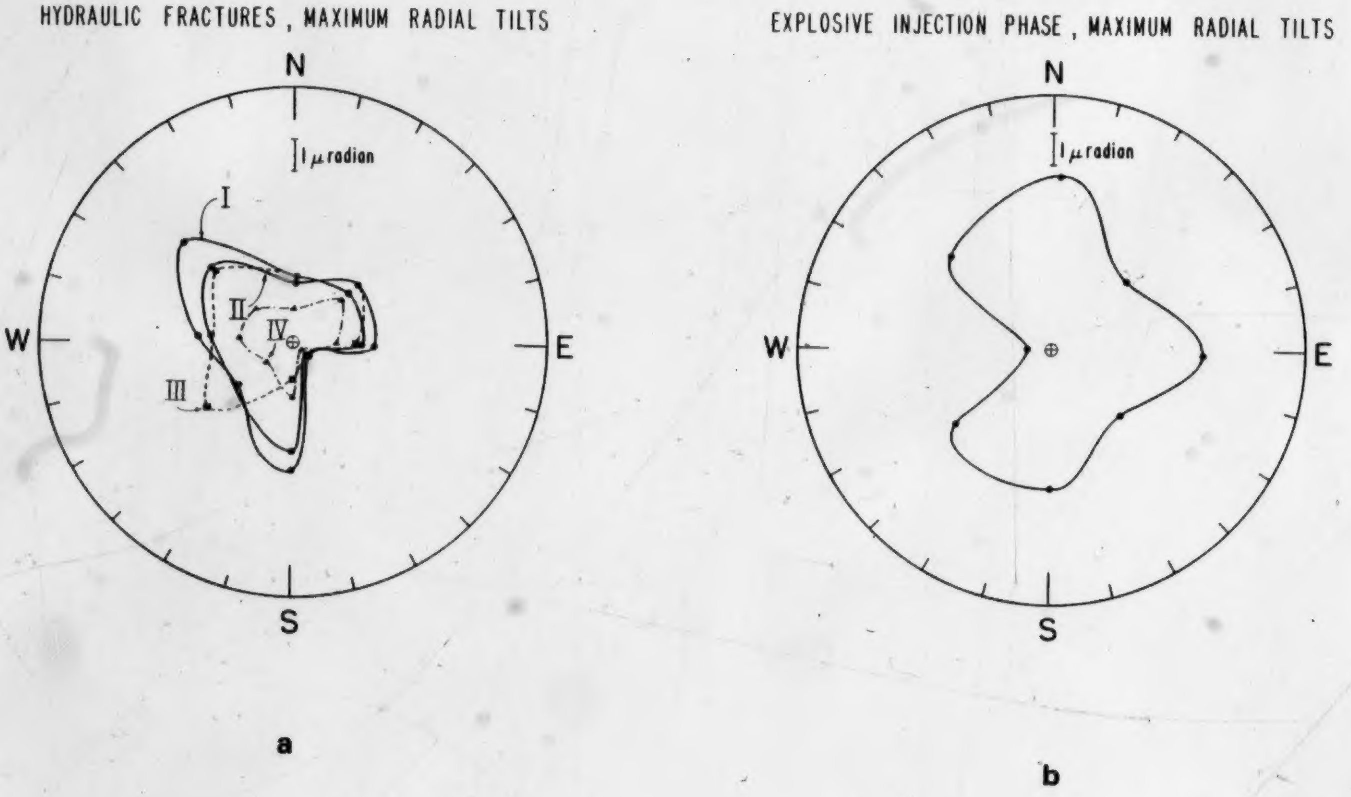

Fig.2.1.7 ..... Examples of surface tilt changes due to (a) hydrauric fracturing operations and (b) an explosive injection (from M.D.Wood Inc., 1980).

(5) Some other examples of ground deformation monitoring for the purpose of delineating the form of hydraulic fractures are,

i) Tilt measurements in tunnel for hydraulic fractures produced near a tunnel in bedded ash fall tuff at a depth of 415 m in Nye Country, Nevada, (M.D.Wood et al, 1981)

ii) Tilt measurements for massive hydraulic fractures at a depth of about 1500 m in Wattenburg gas field, Colorado, (M.D.Wood et al, 1981).

Except for an example cited in (1), the other field experiments with tiltmeter surveys were conducted by M.D.Wood. Inc. (The present name is Fracture Technology Inc.), California, on and after 1978.

Table 2.1.1a and b ..... The major content of the past field experiments in which surface deformation measurements were used to investigate hydraulic fractures.

Index of references
(1) Ren Jen Sun, 1969
(2) Holzhausen et al., 1980
(3) Evans et al., 1980
(4) M.D.Wood Inc., 1979

Index No. of Reference	Location Rock Type, Date		Injection Depth	Injection Materials	Injection Volume	Injection Priod	Calculated Fracture Volume	Survey Data and Magnitude
(1)	ORNL Shale 1960	Sep.3	285 m	(1) water (2) explosive slurry	(1) 3.2-3.4 m^3 (2) 346 m^3	(1) 6 min (2) 660 min	The calculation of fracture radii is based on the injection volume	uplift (max.) (1) N/A (2) 4 mm
		Sep.10	212 m	(1) N/A (2) explosive slurry	(1) N/A (2) 503 m^3	(1) N/A (2) 530 min		uplift (max.) (1) N/A (2) ¬ 12 mm
(2)	Cold Lake Alberta, Oil-sands, 1979		308-317 m	(1) cold water (2) steam	(1.1)+(1.2) 19 m^3 (1.3) 32 m^3 (2) 3650 m^3 calculated in terms of water	(1.1) 7.5 hr (1.2) 2.0 hr (1.3) 3.7 hr (2) 50 days intermittently	radius:volume 40m 6.3 m^3 162m 103.7 m^3	tilt (μradians) (1.1) N/A (1.2) N/A (1.3) N/A (2) 8 events (2.1) 0.95 (2.2) 0.49 (2.3) 0.41 (2.4) 0.13 (2.5) 0.65 (2.6) 0.19 (2.7) 0.96 (2.8) 1.31
(3)	Know Country Ohio, Oil shale, 1979		322-341 m and 305-314 m	Nitrogen	400 m^3 calculated in terms of in-situ volume	28 min	(1) N/A (2) N/A	tilt (μradians) (1) 0.3 (2) 0.2 (3) 0.5
(4)	Rock Spring Wyoming, Oil shale, 1979		(1) 407 ft (2) 340 (3) 393 (4) 386 (5) 407-386	(1)-(4) water (5) explosive slurry	(1) 146 bbl (2) 104 (3) 85 (4) 96 (5) 163	(1) 30 min (2) 30 (3) 30 (4) 30 (5) 18.5	(1) 103 bbl (2) 82 (3) 66 (4) 35 (5) N/A	tilt (μradians) (1) 2.64 (2) 2.48 (3) 2.13 (4) 1.36 (5) 2.36 (radial tilt)

Table 2.1.1a

Index No.	Fracture Shape	Calculated Fracture Size (meter)	Overburden Pressure	Breakdown Pressure <>=estimate at the bottom	Pressure History	
					after breakdown	
(1)	(1) and (2) horizontal penny-shape	radius (1) 13.6-16 (2) 57-86	7.57 MPa from density	(1) 10.4 MPa <13.1 MPa> (2) 15.9 MPa <16.3 MPa>	(1)→9.3→11.3 (2)→11.8→13.8	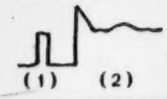
	(1) and (2) horizontal penny-shape	radius (1) N/A (2) 64-88	5.59 MPa from density	(1) N/A (2) 15.2 MPa <17.5 MPa>	(1) N/A (2)→13.8→15.9	N/A
(2)	(1) vertical	(1) N/A		(1) N/A		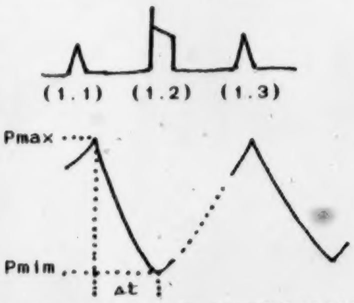
	(2) horizontal penny-shape	(2.1) (2.2) 65-107 (2.3) 60-100 (2.4) 40- 66 (2.5) 72-119 (2.6) 46- 76 (2.7) 83-140 (2.8) 91-162	minimum possible 6.035 MPa from breakdown pressure	(2) Pmax (2.1) 9.36 (2.2) 8.06 (2.3) 8.38 (2.4) 8.20 (2.5) 8.22 (2.6) 8.05 (2.7) 8.00 (2.8) 8.50	Pmin Δt 6.70 1:50 7.16 2:38 7.06 1:14 7.70 2.42 7.00 1:39 7.86 1:05 6.69 4:03 6.80 4:40	
(3)	(1) vertical,2-D (2) horizontal	(1) 183 (2) N/A	6.204 MPa from breakdown pressure	6.204 MPa	8.96 MPa	
(4)	(1)-(5) horizontal	(1) 215 (2) 202 (3) 185 (4) 145 (5) N/A (mean value)	N/A	N/A	N/A	N/A

Table 2.1.1b

2.2 Inception of Hydraulic Fracture

The inception of hydraulic fracture has been mainly examined from the stand point of the occurence of tensile failure on the wall of wellbore. There is also a possibility that the hydraulic fracture breaks out as shear failure. The wall of wellbore or the surrounding formation must contain some pre-existing cracks. Some wells must allow the injected fluid to flow into the formation. Circumstances of well-fracturing can not be limited to a stereotyped form. Various criteria have been proposed regarding fracture initiation from each of these stand points. Here I will review some of those criteria.

(I) Criterion based on tensile strength of smoothed well

The criterion proposed first by Hubbert et al.(1957) is that fracturing will start at points on the wall of wellbore where the effective stress is equal to or greater than the tensile strength of the rock. Based on this criterion, we can predict the direction and critical pressure of the fracture inception, if the circumstances around the wellbore are consistent with simple models. In order to understand the stress field around an injection well, we have to take into consideration at least four kinds of effects. These effects arise from (1) the regional tectonic stresses, (2) the injection pressure, (3) the formation fluid pressure and (4) the fluid flow through the porous rock from the wellbore into the formation. In the following, it is assumed that rock around the wellbore is infinite, elastic, homogeneous and isotropic, and is under a nonhydrostatic state of regional stresses with one of the regional principal stresses acting parallel to the vertical axis of the wellbore.

First, the wellbore is approximated by an infinitely long vertical cylinder of radius a, in a very large rectangular plate of infinite thickness on which edges the horizontal stresses σ_x and σ_y act, as shown in Fig.2.2.1.

The stress field around the cylindrical hole due to the horizontal compressive stresses, σ_x and σ_y , is given by

$$S_{rr}^{(1)} = \frac{\sigma_x + \sigma_y}{2} \left(1 - \frac{a^2}{r^2} \right) + \frac{\sigma_x - \sigma_y}{2} \left(1 - \frac{4a^2}{r^2} + \frac{3a^4}{r^4} \right) \cos 2\theta$$

$$S_{\theta\theta}^{(1)} = \frac{\sigma_x + \sigma_y}{2} \left(1 + \frac{a^2}{r^2} \right) - \frac{\sigma_x - \sigma_y}{2} \left(1 + \frac{3a^2}{r^4} \right) \cos \theta \qquad (2.2.1)$$

$$S_{\theta r}^{(1)} = \frac{\sigma_y - \sigma_x}{2} \left(1 + \frac{2a^2}{r^2} - \frac{3a^4}{r^4} \right) \sin 2\theta$$

where compression is considered as positive.

Next, let us consider the stress field around a cylindrical ring subjected to the internal pressure P (Fig.2.2.2). The stress field with the boundary conditions

$$S_{rr}^{(2)}(r=a) = P \quad , \quad S_{rr}^{(2)}(r=b) = 0 \qquad (2.2.2)$$

is given by

$$S_{rr}^{(2)} = \frac{a^2}{b^2-a^2} \frac{P}{r^2} - \frac{a^2}{b^2-a^2} P$$

$$(2.2.3)$$

$$S_{\theta\theta}^{(2)} = -\frac{a^2 b^2}{b^2-a^2} \frac{P}{r^2} - \frac{a^2}{b^2-a^2} P$$

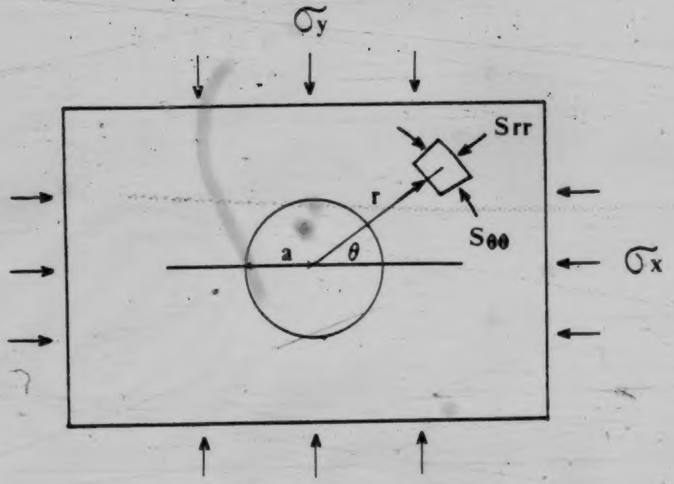
σy
Srr
r
Sθθ
a
θ
σx

Fig.2.2.1 ..... A cylindrical cavity subjected to far-field stresses.

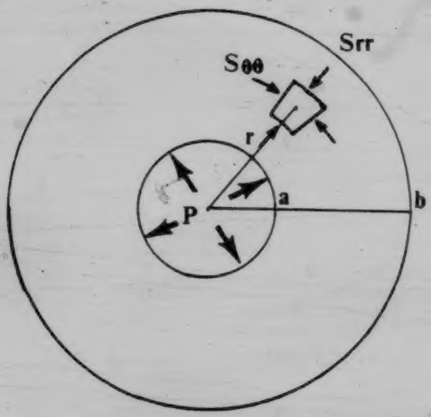
Srr
Sθθ
r
P
a
b

Fig.2.2.2 ..... A cylindrical cavity subjected to an internal pressure.

$$S_{\theta r}^{(2)} = 0$$

The total stress field around the hole subjected to the internal pressure P and the far-field horizontal principal stresses σ_x and σ_y is obtained by superposing Eqs.2.2.1 and 2.2.3. When the outer radius b is considered to be very large in comparison with the inner radius a, the total stresses at the wall of wellbore, r=a, are expressed in the simple form

$$\begin{aligned} T_{ij}^{(1)} &= S_{ij}^{(1)} + S_{ij}^{(2)} \\ T_{rr}^{(1)} &= P \\ T_{\theta\theta}^{(1)} &= (\sigma_x + \sigma_y) - 2(\sigma_x - \sigma_y)\cos 2\theta - P \\ T_{\theta r}^{(1)} &= 0 \end{aligned} \qquad (2.2.4)$$

Here we assume that fracturing will first occur at points on the boundary of wellbore where some stress is equal to or greater than the tensile strength To of the rock. Eq.2.2.4 indicates that the only stress which can become tensile at r=a is the tangential component, $T_{\theta\theta}^{(1)}$, and that the point which stress will first become tensile is $\cos 2\theta = -1$, ($\theta = \pm\pi/2$) , and the stress is given by

$$3\sigma_x - \sigma_y - P$$

where $\sigma_x < \sigma_y$ has been assumed. The fracture will start along a plane normal to the direction of the minimum principal stress. Denoting the critical pressure which overcomes the tensile strength of the rock by Pc, we have a criterion of the fracture initiation

$$P_c \geq 3\sigma_x - \sigma_y + T_o \qquad (2.2.5)$$

(Hubbert et al., 1957).

Eq.2.2.5 is revised when the presence of pore pressure is taken into consideration. The difference between the internal pressure P and the initial pore pressure P_o will be denoted by

$$P_w = P - P_o \tag{2.2.6}$$

and the effective stresses of σ_x and σ_y by

$$\begin{aligned} \sigma_{xx} &= \sigma_x - P_o \\ \sigma_{yy} &= \sigma_y - P_o \end{aligned} \tag{2.2.7}$$

(cf., in general, Eq.2.2.7 is given by $\sigma_{ij}^{effective} = \sigma_{ij}^{total} - k\delta_{ij}P_o$). Then the effective stresses around the hole in porous media of pore pressure P_o, caused by the far-field stresses σ_x and σ_y and the internal pressure P, are given by

$$T_{ij}^{(2e)} = S_{ij}^{(1e)} + S_{ij}^{(2e)} \tag{2.2.8}$$

where $S_{ij}^{(1e)}$ is obtained by replacing σ_x and σ_y in Eq.2.2.1 with σ_{xx} and σ_{yy}, and $S_{ij}^{(2e)}$ is obtained by replacing P in Eq.2.2.3 with Pw. Consequently, the criterion of the fracture initiation is given by

$$\begin{aligned} &P_c \geq 3\sigma_{xx} - \sigma_{yy} + T_o \\ \text{or}\quad &P_c \geq 3\sigma_x - \sigma_y - 2P_o + T_o \end{aligned} \tag{2.2.9}$$

(Haimson et al., 1967, Eq.12), where Pc is the critical value of Pw. As shown tacitly in the above discussions, as long as such an infinitely long vertical cylindrical hole is used as a model of well-fracturing, there is no prediction of the occurrence of horizontal fracture.

In an open-hole well-fracturing procedure, the prospective producing horizon is packed off and fluid is introduced into this zone. Kehle (1964) modelled the circumstances of well-fracturing by a band of uniform pressure and two bands of uniform shear stress acting in a cylindrical cavity as shown in Fig.2.2.3, and obtained the conclusion, from numerical analyses in which the radius of the hole was taken to be 0.21 m; that, for any packer length (1.5, 3.0 and 4.6 m) and any pressure interval (from 1.5 to 15.2 m at 1.52 m increments), the magnitude of the induced tangential and vertical stresses due to the shear bands is negligible (at most a few percent) in comparison with those caused by the band of pressure. Fig.2.2.4 shows the result for the case of packer length 3.0m.

Two interesting regions of induced stress are, (1) either end of the pressurized interval where the tangential stress is zero and the vertical stress is approximately 94 percent of the pressure, and (2) the central part (about 80 percent) of the packed-off interval where the tangential stress equals the pressure and the vertical stress is zero. The induced stresses in the central region of the packed-off interval is shown to be almost identical to those predicted when the cylindrical hole is loaded along its entire length.

The induced stresses on the wall of wellbore, are summarized as follows.

In the central region of the packed-off interval,

$$S^{(3)}_{rr} = P \quad , \quad S^{(3)}_{\theta\theta} = -P \quad , \quad S^{(3)}_{zz} = 0 \qquad (2.2.10a)$$

in the very ends of the interval

$$S^{(3)}_{rr} = P \quad , \quad S^{(3)}_{\theta\theta} = 0 \quad , \quad S^{(3)}_{zz} = -0.94\ P \qquad (2.2.10b)$$

and other components are zero.

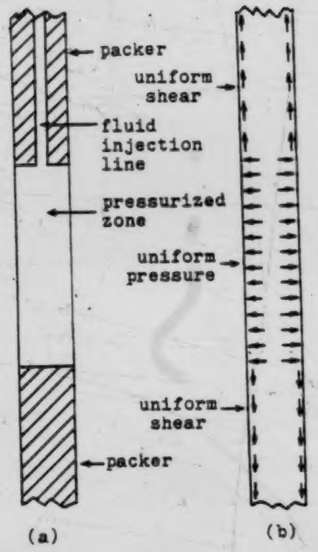
packer
uniform shear
fluid injection line
pressurized zone
uniform pressure
uniform shear
packer
(a)
(b)

Fig.2.2.3 ..... Schematic diagram of (a) hydraulic fracturing set-up and (b) associated boundary stress assumed by Kehle.

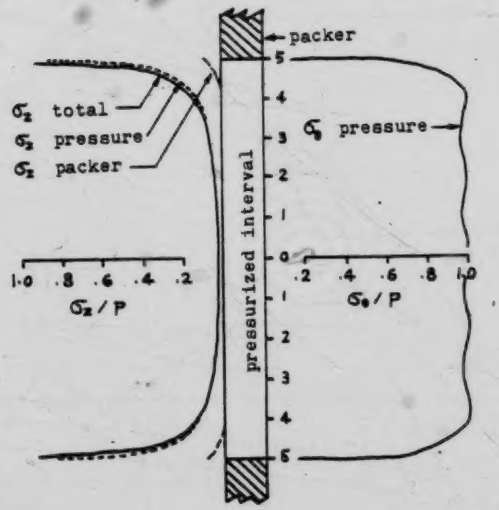

Fig.2.2.4 ..... Vertical and tangential stresses induced at the wall of the hole due to stresses in Fig.2.2.3. (from Kehle, 1964).

The total stresses at r=a, $T_{ij}^{(3)}$, are given by superposing Eq.2.2.1 and Eq.2.2.10.

$$T_{ij}^{(3)} = S_{ij}^{(1)} + S_{ij}^{(3)} \tag{2.2.11}$$

When the pore pressure P_o is considered, the effective stresses of $T_{ij}^{(3)}$ are expressed in the form

$$T_{ij}^{(3e)} = S_{ij}^{(1e)} + S_{ij}^{(3e)} \tag{2.2.12}$$

where $S_{ij}^{(3e)}$ is obtained by replacing P in Eq.2.2.10 with Pw of Eq.2.2.6. The concrete expression of $T_{ij}^{(3e)}$ is, in the central region,

$$\begin{aligned} T_{rr}^{(3e)} &= P_w \\ T_{\theta\theta}^{(3e)} &= 3\sigma_{xx} - \sigma_{yy} - P_w \qquad (\text{ at } \theta = \pm\pi/2) \\ &= 3\sigma_x - \sigma_y - P_w - 2P_o \\ T_{zz}^{(3e)} &= \sigma_{zz} = \sigma_z - P_o \end{aligned} \tag{2.2.13a}$$

and in the end region,

$$\begin{aligned} T_{rr}^{(3e)} &= P_w \\ T_{\theta\theta}^{(3e)} &= 3\sigma_{xx} - \sigma_{yy} \qquad (\text{ at } \theta = \pm\pi/2) \\ &= 3\sigma_x - \sigma_y - 2P_o \\ T_{zz}^{(3e)} &= \sigma_{zz} - 0.94\,P_w = \sigma_z - P_o - 0.94(P - P_o) \end{aligned} \tag{2.2.13b}$$

(Kehle, Eq.37), where σ_{zz} is the effective stress of the vertical component σ_z of the regional stresses.

From Eq.2.2.13, we observe that, besides the tangential stress $T_{\theta\theta}^{(3e)}$ in the central region, the vertical stress $T_{zz}^{(3e)}$ in the edge region can become tensile. This suggests a possibility that horizontal fracturing takes place. The critical pressure Pc for the occurrence of a horizontal fracture is given by

$$P_c \geq \frac{\sigma_{zz} + T_o}{0.94} \quad \text{or} \geq \frac{\sigma_z + T_o - P_o}{0.94} \tag{2.2.14}$$

Next we will suppose that fluid flows from the borehole into the surrounding formation. To simplify the flow problem, the wellbore is again assumed to be an infinitely long cylindrical cavity. It is also assumed that the formation has uniform permeability so that the fluid flow is axisymmetric, and that the injection fluid has properties similar to those of the formation pore fluid, and that the fluid flow obeys Darcy's law.

The effect of the fluid penetration is demonstrated by the stresses $S_{ij}^{(4)}$ caused by the pressure distribution P(r) in the formation under the condition of steady flow and with the boundary conditions

$$S_{rr}^{(4)}(r=a) = S_{rr}^{(4)}(r=b) = 0 \tag{2.2.15a}$$

$$P(r=a) = P \quad , \quad P(r=b) = 0 \tag{2.2.15b}$$

The stress tensor $S_{ij}^{(4)}$ due to the pressure P(r) is given by, in terms of the radial displacement u,

$$\begin{aligned} S_{rr}^{(4)} &= \lambda\Delta + 2\mu\frac{du}{dr} - (3\lambda+2\mu)\alpha P \\ S_{\theta\theta}^{(4)} &= \lambda\Delta + 2\mu\frac{u}{r} - (3\lambda+2\mu)\alpha P \\ S_{zz}^{(4)} &= \lambda\Delta - (3\lambda+2\mu)\alpha P \\ \Delta &= \frac{du}{dr} + \frac{u}{r} \end{aligned} \tag{2.2.16}$$

and other stress components are zero, where λ and μ are Lame's constants, and α is a material constant. Since we are supposing the state of steady flow, the pressure distribution P(r) satisfies the Laplace equation. The boundary conditions Eq.2.2.15b determine a solution of this differential equation.

$$P(r) = P \log(b/a) / \log(b/r) \qquad (2.2.17)$$

On the other hand, the boundary conditions Eq.2.2.15a determine a solution of a differential equation in terms of u, which derives from the equilibrium equation. Finally, the stresses $S_{ij}^{(4)}$ are given by

$$S_{rr}^{(4)} = \frac{\alpha E P}{2(1-\nu)\log(b/a)} \left\{ -\log\frac{b}{r} - \frac{a^2}{b^2-a^2}\left(1-\frac{b^2}{r^2}\right)\log\frac{b}{a} \right\}$$

$$S_{\theta\theta}^{(4)} = \frac{\alpha E P}{2(1-\nu)\log(b/a)} \left\{ 1-\log\frac{b}{r} - \frac{a^2}{b^2-a^2}\left(1+\frac{b^2}{r^2}\right)\log\frac{b}{a} \right\}$$

$$S_{zz}^{(4)} = \frac{\alpha E P}{2(1-\nu)\log(b/a)} \left\{ 1-2\log\frac{b}{r} - \frac{2a^2}{b^2-a^2}\log\frac{b}{a} \right\} \qquad (2.2.18)$$

(cf., Takeuchi, P149). When b is considered to be very large compared with a, the stresses Eq.2.2.18, at r=a, are simplified in the form

$$\begin{aligned} S_{rr}^{(4)} &= 0 \\ S_{\theta\theta}^{(4)} &= \alpha E \frac{1-2\nu}{1-\nu} P \qquad (2.2.19) \\ S_{zz}^{(4)} &= \alpha E \frac{1-2\nu}{1-\nu} P \end{aligned}$$

The total stress field is obtained by the superposition of the stresses $S_{ij}^{(1e)}$ due to the far-field regional stresses σ_x and σ_y, $S_{ij}^{(2e)}$ due to the pressure difference Pw, $S_{ij}^{(4)}$ due to the fluid penetration and the initial pore pressure P_o.

$$T_{ij}^{(4)} = S_{ij}^{(1e)} + S_{ij}^{(2e)} + S_{ij}^{(4)} + P_o \qquad (2.2.20)$$

For convenience, let

$$\alpha E \frac{1-2\nu}{1-\nu} = \beta(1-2\nu) = 2\eta \ , \quad \beta = 1 - \frac{C_r}{C_b} \qquad (2.2.21)$$

(cf., Rice et al., 1976, p239) where Cr and Cb are the rock matrix compressibility and the rock bulk compressibility, respectively. Then the stresses $T_{ij}^{(4)}$ are given by

$$\begin{aligned} T_{rr}^{(4)} &= P_w + P_o \\ T_{\theta\theta}^{(4)} &= (\sigma_{xx} - \sigma_{yy}) - 2(\sigma_{xx} + \sigma_{yy}) \cos 2\theta - P_w + 2\eta P_w + P_o \\ T_{zz}^{(4)} &= \sigma_{zz} + P_o + 2\eta P_w \end{aligned} \qquad (2.2.22)$$

From Eq.2.2.22, the minimum value of $T_{\theta\theta}^{(4)}$ is found at $\theta = \pm \pi/2$,

$$T_{\theta\theta}^{(4),min} = 3\sigma_{xx} - \sigma_{yy} - P_w + 2\eta P_w + P_o \qquad (2.2.23)$$

The effective stress of $T_{\theta\theta}^{(4),min}$ is

$$T_{\theta\theta}^{(4),min} - (P_w + P_o) = 3\sigma_{xx} - \sigma_{yy} - 2P_w + 2\eta P_w \qquad (2.2.24)$$

The critical value Pc of the pressure difference Pw, which will break the wall of wellbore, is now given by

$$P_c \geq \frac{3\sigma_x - \sigma_y - 2P_o - T_o}{2(1-\eta)} \qquad (2.2.25)$$

(Haimson et al., 1967, Eq.10).

When the induced vertical stress $T_{zz}^{(4)}$ in Eq.2.2.19 is combined with $T_{zz}^{(3e)}$ of the Kehle's model (Eq.2.2.13b), the critical pressure of the occurence of horizontal fracture is given by

$$P_c \geq \frac{T_o + \sigma_{zz}}{1.94 - 2\eta} \qquad (2.2.26)$$

As $\phi < \beta < 1$ where ϕ is the porosity of rock, and $0 < \nu < 0.5$ for rock, it follows $0 < 2\eta < 1$. The comparisons between Eqs.2.2.25 and 2.2.9 for the horizontal fracture and between Eqs.2.2.26 and 2.2.14 for the vertical fracture suggest that the fluid penetration causes the inception of either type of the fractures at lower injection pressure than that for the non-penetration case. It is also suggested that very rapid pressurization leads to a higher fracture pressure than needed when pressurized fluid is allowed sufficient time to penetrate the walls of the wellbore.

Heat conduction through solids gives rise to stresses and displacements analogous to those caused by fluid flow through porous media. Therefore, the above discussions can be applied to estimate thermoelastic effects associated with, for example, hot fluid injections. The stress field due to non-stationary fluid flow has been studied by Rice et al.(1976) in more general form.

(II) Criterion based on fracture toughness of notched well

The previous criterion is based on a critical tensile stress fracture and neglect of consideration of cracks in the wall of the wellbore. Here, I will refer to a criterion of fracture initiation which is based on linear elastic fracture mechanics and allows pre-existing cracks on the wellbore.

Assume a cylindrical hole of radius a with two radially opposed cracks of length L subjected to an internal pressure P and the far-field stresses σ_1 and σ_3 , as shown in Fig.2.2.5. The stress intensity factor Ki at the crack tip is given by

$$K_1 = P\sqrt{\pi L}\, F(L/a) - (\sigma_1 \cos^2\alpha + \sigma_3 \sin^2\alpha) F(L/a)\sqrt{\pi L} + (\sigma_1 \cos 2\alpha - \sigma_3 \cos 2\alpha) G(L/a)\sqrt{\pi L} \qquad (2.2.27)$$

(Abou-Sayed et al., 1978, Eq.10), where F(L/a) and G(L/a) are shown in Table 2.2.1. Let Kic and Pc respectively denote the fracture toughness and the critical pressure for crack advance. From Eq.2.2.26, the critical condition of the crack extension is expressed in the form

$$P_c = I(\alpha)(\sigma_1 - \sigma_3) + \sigma_3 + \frac{K_{1c}}{F(L/a)\sqrt{\pi L}}$$

$$I(\alpha) = \cos^2\alpha - \frac{G(L/a)}{F(L/a)} \cos 2\alpha \qquad (2.2.28)$$

The function $I(\alpha)$ is shown in Fig.2.2.6. Eq.2.2.28 states several features of the fracture initiation under the circumstances of the wellbore with such pre-existing small cracks.

If $\sigma_1 = \sigma_3$, the orientation of the pre-existing crack does not contribute to the critical pressure, and only the length of crack influences the critical pressure by a factor of $K_{1c} / F(L/a)\sqrt{\pi L}$, suggesting that fracturing in the wellbore with larger cracks will start at lower pressure. If $I(\alpha) = 0$, the critical pressure depends on either principal stress.

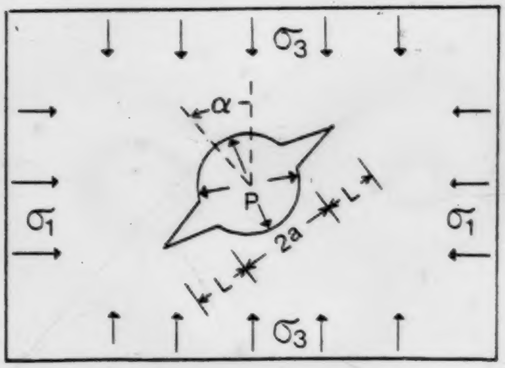

Fig.2.2.5 ..... Crack in a borehole wall subjected to far-field stresses and internal pressure.

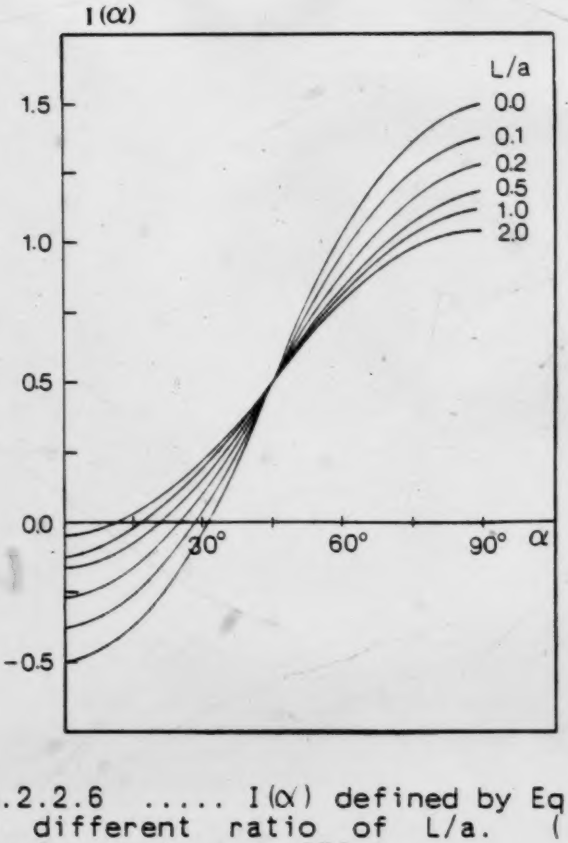

Fig.2.2.6 ..... I(α) defined by Eq.2.2.28 for different ratio of L/a. (from Abou-Sayed et al., 1978).

L/a	One Crack		Two Crack	
	G(L/a)	F(L/a)	G(L/a)	F(L/a)
0.0	3.39	2.26	3.39	2.26
0.1	2.73	1.98	2.73	1.98
0.2	2.30	1.82	2.41	1.83
0.3	2.04	1.67	2.15	1.70
0.4	1.86	1.58	1.96	1.61
0.5	1.73	1.49	1.83	1.57
0.6	1.64	1.42	1.71	1.52
0.8	1.47	1.32	1.58	1.43
1.0	1.37	1.22	1.45	1.38
1.5	1.18	1.06	1.29	1.26
2.0	1.06	1.01	1.21	1.20
3.0	0.94	0.93	1.14	1.13
5.0	0.81	0.81	1.07	1.06
10.0	0.75	0.75	1.03	1.03
	0.707	0.707	1.00	1.00

Table 2.2.1 ..... Tabulation of the function F and G in Eq.2.2.27 (from Paris and Sih, 1965).

If $\alpha = 0$, i.e., the orientation of the pre-existing cracks is perpendicular to the direction of the minimum principal stress axis, the crack advances most easily. If $\alpha = \pi/2$, the maximum pressure is required to advance the crack, because $I(\alpha) > I(\beta)$, $\alpha > \beta$ from Fig.2.2.6. When the case of L/a=0.2 is examplified, the difference of the critical pressures for $\alpha = 0$ and $\alpha = \pi/2$ is given by $1.5(\sigma_1 - \sigma_3)$, where $I(\alpha=\pi/2) = 1.25$ and $I(\alpha=0) = -0.25$ are read from Fig.2.2.6. On the other hand, if the crack length is considered to be large enough compared with the radius of wellbore, a , i.e., $L/a \sim \infty$, it follows that $I(\alpha=0) \sim I(\alpha=\pi/2)$, hence there is no difference between these critical pressures.

If $\alpha = 0$ and $L \sim 0$ (say, L/a=0.1),

$$2P_c \sim 3\sigma_3 - \sigma_1 + 2K_{1c}/2.26\sqrt{\pi L} \qquad (2.2.29)$$

where the value 2.26 comes from Table 2.2.1. It is observed that Pc in Eq.2.2.29 is related to $3\sigma_3 - \sigma_1$ by factor 2, whereas in Eq.2.2.9 the factor is 1, and that Eq.2.2.29 holds true without regard to the existence of pore pressure. It is noted that Eqs.2.2.27-29, in principle, can not used for the case L=0 and there is no consideration of the stress intensity factor for shearing mode.

(III) **Mohr-Coulomb criterion for shear failure**

Coulomb (1733) proposed a criterion that when shear failure takes place across a plane, the normal stress and the shear stress across this plane are related by

$$|\tau| \geq S_0 + \mu_i \sigma \qquad (2.2.30)$$

where S_0 is a constant which is regarded as the inherent shear strength of the material, and μ_i is a constant which is called the coefficient of internal friction of the material. The coefficient μ_i is usually expressed as

$$\mu_i = \tan\phi \qquad (2.2.31)$$

and ϕ is called the angle of internal friction.

The two-dimensional case will be considered. The normal stress σ and shear stress τ acting across a plane perpendicular to the $\sigma_1-\sigma_3$ -plane and making an arbitrary angle α with the direction of least principal stress σ_3, (Fig.2.2.7a), are

$$\begin{aligned} 2\sigma &= (\sigma_1+\sigma_3) + (\sigma_1-\sigma_3)\cos 2\alpha \\ 2\tau &= (\sigma_1-\sigma_3)\sin 2\alpha \end{aligned} \qquad (2.2.32)$$

A very convenient method of graphically representing these expressions, known as the Mohr diagram, is obtained by plotting values of normal and shear stress with respect to σ - τ -coordinate axes for all possible values of the angle α, (Fig.2.2.7b). Then the relation of Eq.2.2.30 is represented by a straight line, for example, AB in Fig.2.2.7b.

Eq.2.2.30 suggests that failure will not take place if the values of σ and τ so found lie below the line AB, and failure will take place if the circle on σ_1 and σ_3 as diameter just touches AB. The substitution of Eq.2.2.32 into Eq.2.2.30 gives another expression for this failure

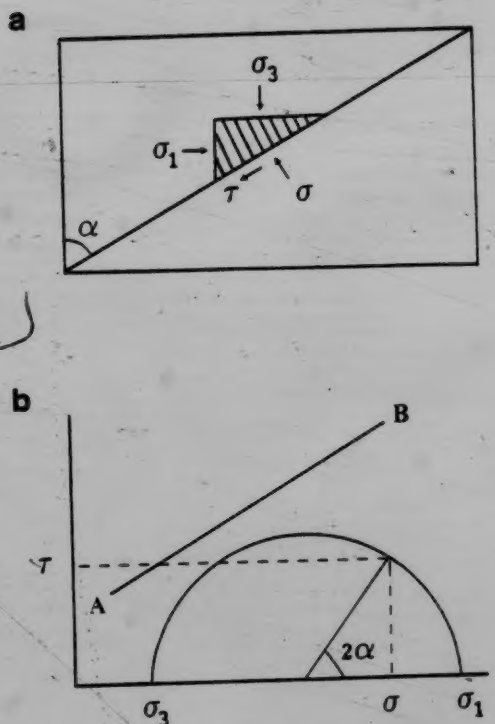
a
σ_3
σ_1
τ
σ
α
b
B
τ
A
2α
σ_3
σ
σ_1

Fig.2.2.7 ..... The Mohr diagram in 2-D.

criterion

$$\sigma_1\left[(\mu_i^2+1)^{\frac{1}{2}}+\mu_i\right]-\sigma_3\left[(\mu_i^2+1)^{\frac{1}{2}}-\mu_i\right] \geq 2S_0$$

$$\text{at } \alpha = \pm(\pi/4+\phi) \quad \text{i.e.,} \quad \cot 2\alpha = \pm 2\mu_i \qquad (2.2.33)$$

When the presence of pore pressure P_0 is taken into consideration, Eq.2.2.30 is revised as

$$|\tau| \geq S_0+\mu_i(\sigma-P_0) \qquad (2.2.34)$$

As suggested by a shift of the Mohr circle in the left direction along σ -axis in the Mohr diagram, an increase of the pore pressure P_0 accelerates the occurence of failure.

Mohr (1900) replaced the criterion Eq.2.2.30 by a functional relation characteristic of material

$$|\tau| \geq f(\sigma) \qquad (2.2.35)$$

The curve of $f(\sigma)$ is called the Mohr envelope, and obtained experimentally as the envelope of the Mohr circles corresponding to failure under a variety of conditions. With regard to the function $f(\sigma)$, the coefficient of internal friction is defined by

$$\mu_i = \frac{\partial|\tau|}{\partial\sigma} = \tan\phi \qquad (2.2.36)$$

The angle of internal friction has values usually between 20-50 degrees and most commonly not far from 30 degrees ($\mu_i \sim 0.6$). The Mohr envelope is usually concave downward. At sufficiently high pressures, nearly all rocks deform plastically, and the Mohr envelopes becomes approximately parallel to the σ -axis.

The tangential and normal stresses acting on a plane with an arbitrary orientation relative to three principal stress axes can easily be seen from the Mohr's representation of stress in three dimensions (Fig.2.2.8). As long as the failure strength through the body of the rock of interest is assumed to be characterized by unique values of S_0 and μ_i in Eq.2.2.30 or a unique function f in Eq.2.2.35, the Mohr-Coulomb criterion basically states that (1) possible failure planes are always parallel to the axis of the intermediate principal stress, and (2) this stress does not affect the angle of the failure plane. It is so because the line $|\tau| = S_0 + \mu_i \sigma$ or the curve $|\tau| = f(\sigma)$ will first touch a point on the circle on σ_1 and σ_3 as diameter, and this circle represents a plane of $\varphi = 0$. Past laboratory experiments (e.g., Mogi, 1971; Handin et al., 1967), however, have pointed out that the above statement (2) does not necessarily hold true. This will be described later.

Most sedimentary and metamorphic rock is anisotropic. Representing the anisotropy by the presence of a plane of weakness, its effect on strength can be seen by using the Mohr's diagram. The inherent shear strength and the coefficient of internal friction in the place of weakness will be denoted by Sw and μ_w , respectively. In Fig.2.2.9, let the point P, the line AB $\tau = S_w + \mu_w \sigma$ and the line CD $\tau = S_0 + \mu_0 \sigma$ respectively be a stress state on the plane of weakness under the principal stresses σ_1 , σ_2 and σ_3 , the critical condition of the failure in the plane of weakness and that through the body of the material. Suppose, now, that the principal stresses are changed up to σ_1' , σ_2'

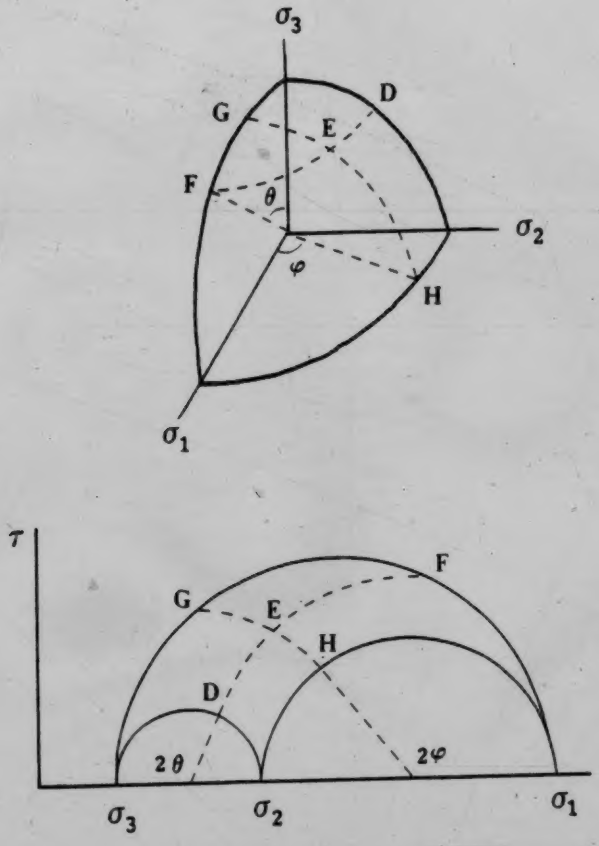
σ3
D
G
E
F
θ
σ2
φ
H
σ1
τ
F
G
E
H
D
2θ
2φ
σ3
σ2
σ1

Fig.2.2.8 ..... The Mohr diagram in 3-D.

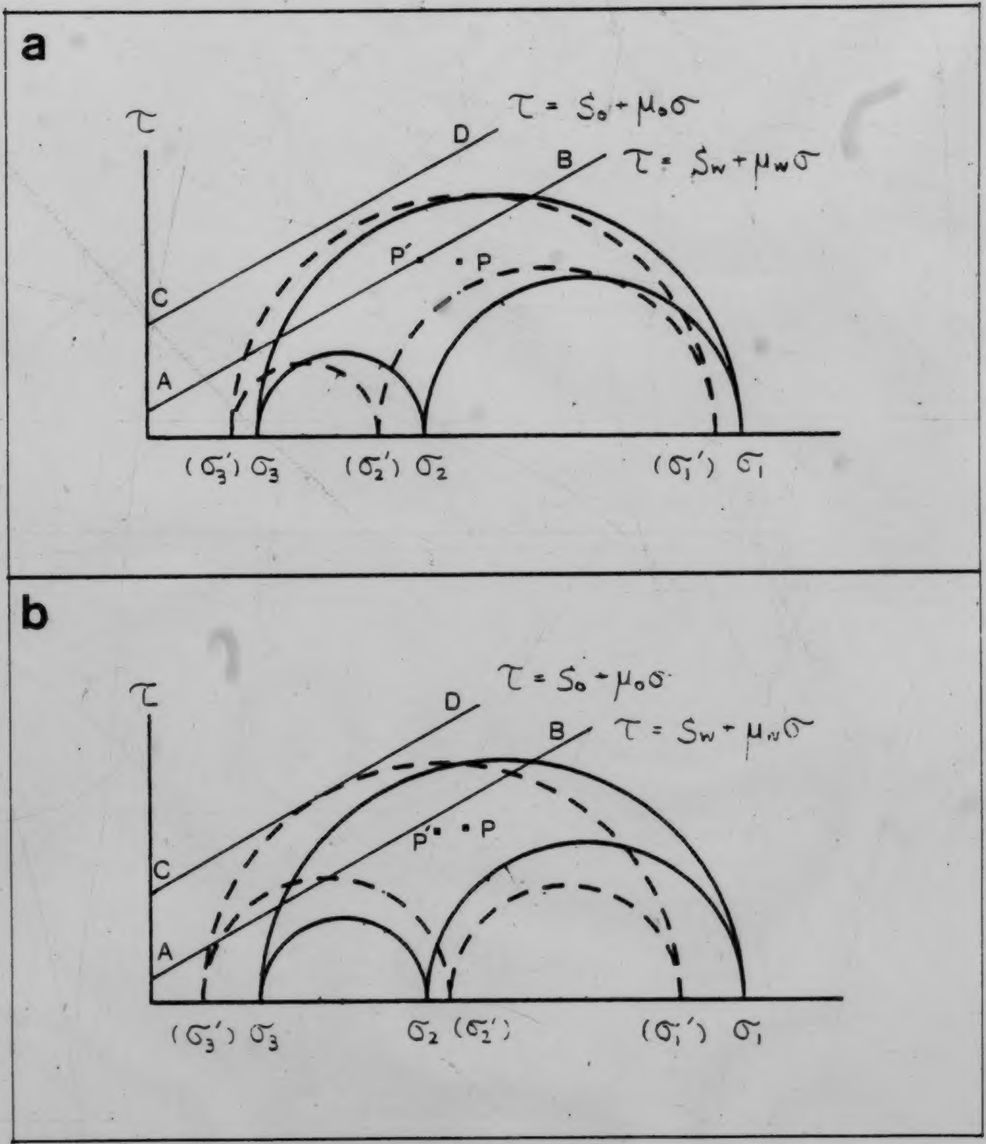
a
τ
$\tau = S_0 + \mu_0\sigma$
$\tau = S_w + \mu_w\sigma$
D
B
C
A
P'
P
$(\sigma_3')\ \sigma_3$
$(\sigma_2')\ \sigma_2$
$(\sigma_1')\ \sigma_1$
b
τ
$\tau = S_0 + \mu_0\sigma$
$\tau = S_w + \mu_w\sigma$
D
B
C
A
P'
P
$(\sigma_3')\ \sigma_3$
$\sigma_2\ (\sigma_2')$
$(\sigma_1')\ \sigma_1$

Fig.2.2.9 ..... Mohr diagrams for discussion of (a) failure in a plane of weakness and (b) failure through a body.

and σ_3' as shown in Fig.2.2.9a. The point P will move to the point P', and will touch the line AB. Failure first becomes possible in the plane of weakness. On the other hand, there is another possibility that failure first occurs through the body regardless of the presence of the weakness, as a result of, for example, the changes of three principal stresses as shown in Fig.2.2.9b.

Extremity of anisotropy is represented by the presence of a discontinuity in the material such as a joint, crack or fault. Byerlee (1977) points out that the frictional strength can be expressed by the relation

$$\begin{aligned} \tau &= 0.85\sigma \quad &;\quad & 0.5 < \sigma < 2 \text{ kbar} \\ \tau &= 0.5 + 0.6\sigma \quad &;\quad & 2.0 < \sigma < 20 \text{ kbar} \end{aligned} \qquad (2.2.37)$$

and that this relation almost holds without regard to types of rock, temperature, presence of gouge between discontinuity surfaces, and roughness of the surfaces, i.e., regardless of smoothed surfaces, pre-made shear failure surfaces or interlocking surfaces made by tensile forces. The frictional strength under the presence of pore pressure P_o is expressed by the relation

$$\tau = 0.1 + 0.6(\sigma - P_o) \qquad (2.2.38)$$

(Byerlee, 1967).

Criteria of shear failure may be expressed in the general form

$$f(\sigma_1, \sigma_2, \sigma_3) = 0 \qquad (2.2.39)$$

One of the failure criteria which take account of the effect of the intermediate principal stress is the von Mises criterion proposed as a yield criterion, and is expressed by

$$(\sigma_1-\sigma_2)^2+(\sigma_2-\sigma_3)^2+(\sigma_3-\sigma_1)^2 = 2\sigma_o \qquad (2.2.40)$$

where σ_o is a value characteristic of material. The von Mises criterion has the physical interpretation that yield occurs when the strain energy reaches a value characteristic of material. On the other hand, it has been shown that the relation

$$\frac{1}{3}\left\{(\sigma_1-\sigma_2)^2+(\sigma_2-\sigma_3)^2+(\sigma_3-\sigma_1)^2\right\} = g(\sigma_1+\sigma_3) \qquad (2.2.41)$$

explains rock failure well, and the function g is regarded to be a monotonically increasing and almost linear function, (Mogi, 1971). From the facts that the planes of failure are observed always parallel to the intermediate principal stress axis and that $(\sigma_1+\sigma_3)/2$ is related to the mean stress acting on a failure plane, this failure criterion is interpreted such that failure will occur when the shear strain energy reaches a critical value which varies with the mean stress. Past observations (e.g., Mogi,1972) also indicate that the angle of the failure plane relative to σ_1 or σ_3 axis depends on the magnitude of σ_2, whereas the Mohr-Coulomb criterion can not predict the effect of σ_2 on the failure.

2.3 Fracture Orientation Changes

Two examples of the change of fracture orientation have been seen in Section 2.1-(2) and (3). It might be a rather common phenomenon that a fracture changes its orientation in the process of growth. Some factors of fracture orientation changes are reviewed here.

Holzhausen et al. (1980) reported the initial formation of a vertical fracture caused by cold-water injection and the subsequent growth of horizontal fractures during steam injections. The orientation change was interpreted as a result of thermal expansion of the surrounding materials during the steam injections, which led to the build-up of horizontal stresses around the initial vertical fracture and resulted in a stress state where the horizontal stresses exceeded the vertical stress compression.

Without the thermal effect, change of fracture orientation can be explained from the more general standpoint of a change in the minimum principal stress direction around an initial fracture due to subsequent fluid injections. Dusseault (1980) explained the change of fracture orientation as follows. "If the injection rate is relatively rapid, then energy dissipation due to viscous traction on the walls of the fracture can result in thick fracture generation with rapid local overstressing, particularly near the injection point. It is believed that the minimum principal stress is increased to a value somewhat higher than the intermediate principal stress before reinjection takes place. Fractures thereafter tend to recur by fluid injection in the direction approximately orthogonal to the original plane." The numerical analyses of Dusseault et al. (1980) indicate more clearly that regional stress changes can be brought about by massive injection volume, change of fracture orientation is extremely likely, and thermal input enhances this probability. The numerical analyses are based on a vertical fracture model in layered media with the assumptions of reasonable material property and geometry related to the application of hydraulic fracturing in the Cold Lake oil sands region.

Evans et al. (1980) reported that a significant change of the surface tilt responses during the continuous injection operation suggested a possibility of the transition of the fracture orientation from vertical to horizontal. The transition was interpreted in connection with the in-situ minimum principal axis direction varying with the depth. The top depth of the initial near-vertical fracture calculated from the measured tilt responses coincided with a depth estimated by the analysis of the in-situ overburden stress gradient, i.e., the depth where the minimum principal stress direction changes from horizontal to vertical. Although it can not be simply concluded that the latter depth equals just the depth of the occurrence of the horizontal fracture, as a rule the spatial variation of pre-existing stress field, could be a major factor in fracture orientation changes.

Lithologic factors also must control the propagation of fracture. Evans et al. (1980) remarked that the calculated top depth of the vertical fracture corresponds to a lithologic boundary, and the overlying lithology must have acted a barrier to prevent the propagation of the vertical fracture. Dusseault (1980) described as follows. "It is said for the Athabasca oil sands region that, in those areas where horizontal fractures are originally created, the fractures tend to climb upward at angles of 10 to perhaps as high as 25 degrees. The tendency for a horizontal fracture to climb has often been explained in terms of density; if air or gas is injected, it is assumed that there is a tendency for fractures to climb upward because of the buoyancy of the air or gas. Another explanation exists: in a material with variably oriented anisotropies (bedding planes, joints), fractures will tend to climb along appropriately oriented bedding features and other lithologic discontinuities." Even if the uncertain lithologic factors are not considered, the tendency for a horizontal fracture to turn upward can be predicted theoretically, as shown below.

Several workers in fracture mechanics have proposed theories which incorporate the magnitudes of stress intensity factors at crack tip, Ki (for open mode) and Kii (for shearing mode), and predict the propagation direction (e.g., Sih, 1972, Erdorgan and Aksogan, 1974). These theories state that a non-zero value of Kii should result in propagation out of the original plane of the fracture in directions governed by the sign of Kii. In the following, I will refer to two of these theoretical predictions. One of them observes the non-zero Kii resulting from the mechanical interaction between the free-surface and a fracture. The other analyzes the stress intensity factors of a fracture subjected to the internal pressure and non-hydrostatic regional stresses.

Pollard et al. (1979) used a two-dimensional fracture model, and analyzed the stress intensity factors at the crack tips of an internally pressurized plane fracture under hydrostatic far-field stresses in a semi-infinite region. The analyses led to the prediction that a shallow fracture, whose original plane is not vertical, tends to turn upward at the ends and propagates toward the free-surface.

Assume an infinitely long fracture in an infinite region. The stress intensity factors at the tips of this fracture are given by

$$K_I = P\sqrt{a} \quad (\equiv K_\infty), \quad K_{II} = 0 \qquad (2.3.1)$$

where P is the uniform internal pressure and a is the half-length of the fracture. If the depth of the fracture, d, is sufficiently large compared with the half-length, the fracture may be assumed to be located in an infinite region. Such a fracture should propagate in its own plane, because Kii=0.

For shallow fractures, the mechanical interaction with the free-surface must not be negligible. Fig.2.3.1 shows the

Fig.2.3.1 ..... Stress intensity factors at the edge of an infinitely long (2-D) fracture subjected to a uniform internal pressure. (a)= a vertical fracture (b)= a horizontal fracture (from Pollard et al., 1979).

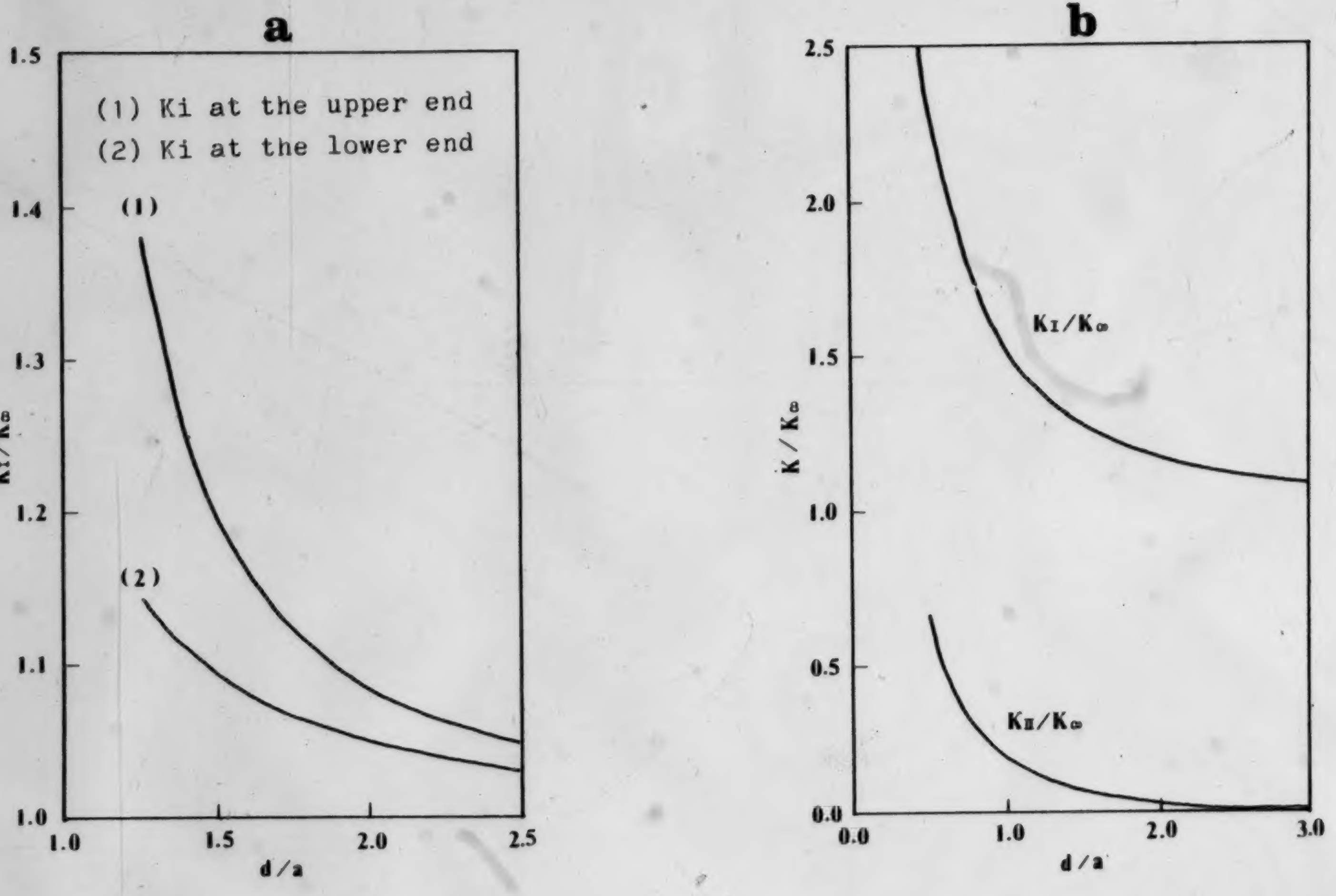
a
(1) Ki at the upper end
(2) Ki at the lower end
(1)
(2)
KI/K∞
1.0
1.1
1.2
1.3
1.4
1.5
1.0
1.5
2.0
2.5
d/a
b
KI/K∞
KII/K∞
K/K∞
0.0
0.5
1.0
1.5
2.0
2.5
0.0
1.0
2.0
3.0
d/a

stress intensity factors normalized by K_∞ and plotted versus the ratio d/a. In the case of vertical fractures (Fig.2.3.1a), symmetry about the long axis of the fracture makes Kii zero, but the values of Ki increase sharply as d/a decreases to a limit of 1.0. Because of Kii=0, the vertical fracture should propagate in its own vertical plane. The fact that the value of Ki at the upper end of the vertical fracture exceeds that at the lower end suggests that the fracture preferentially propagates upward. In the case of horizontal fractures (Fig.2.3.1b), the values of Ki at both ends are equal and sharply increase as d/a decreases toward zero. Non-zero Kii are now observed. The values of Kii at both ends are equal but opposite in sign, and sharply increase as d/a decreases. The existence of non-zero Kii and the signs of Kii at both ends suggest that a shallow horizontal fracture should turn upward at both ends and propagate toward the free-surface (Fig.2.3.2). It has been also observed that varying the inclination, at constant d/a, does not result in large variation in stress intensity factors, except where the upper end of fracture is very near the free-surface. An inclined fracture also will proceed out of the original plane, generally tending toward the free-surface at both ends, as suggested by the non-zero Kii and the signs.

The comparison of the magnitudes of Ki in Fig.2.3.1a and b indicates that, for comparable d/a, Ki for a horizontal fracture is greater than that for a vertical

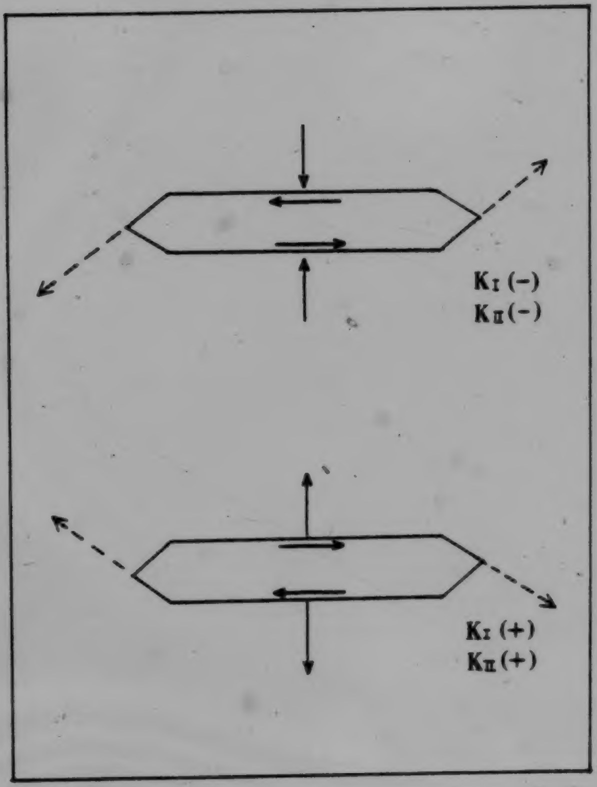
$K_I(-)$
$K_{II}(-)$
$K_I(+)$
$K_{II}(+)$

Fig.2.3.2 ..... Interpretation of signs of stress intensity factors and propagation directions of a fracture.

fracture, except where the depth is very close to the surface.

An assumption of uniform pressure acting on fracture walls is more or less at variance with reality, especially when the frictional interaction between viscous fluid and fracture walls is considered (e.g., McClain, 1969). Fig.2.3.3 shows the difference of the stress intensity factors resulting from a type of pressure gradient in a fracture from those resulting from uniform pressurization. This figure indicates that the magnitudes of Ki and Kii for a fracture characterized by the symmetric linear pressure gradient are less than those for a fracture characterized by the uniform pressure. On the other hand, it has been observed that the ratio Kii/Ki for the former model is greater than that for the latter model. This suggests that a horizontal fracture maintained by the pressure with such a gradient should tend to propagate toward the ground at higher angles than those in which the pressure is essentially uniform.

When a symmetric, linear distribution of driving pressure is given by

$$P(x) = P_o - \Delta P\,|x|\ , \quad P(a) = 0\ ; \quad 0 \le |x| \le a \qquad (2.3.2)$$

the stress intensity factors for a deeply buried fracture (i.e., the fracture may be assumed to be in an infinite region) are given by

$$K_I = (P_o - 2a\Delta P/\pi)\sqrt{a}\ , \quad K_{II} = 0 \qquad (2.3.3)$$

(Lachenbruch, 1961, Pollard, 1976). In the case in which P_o

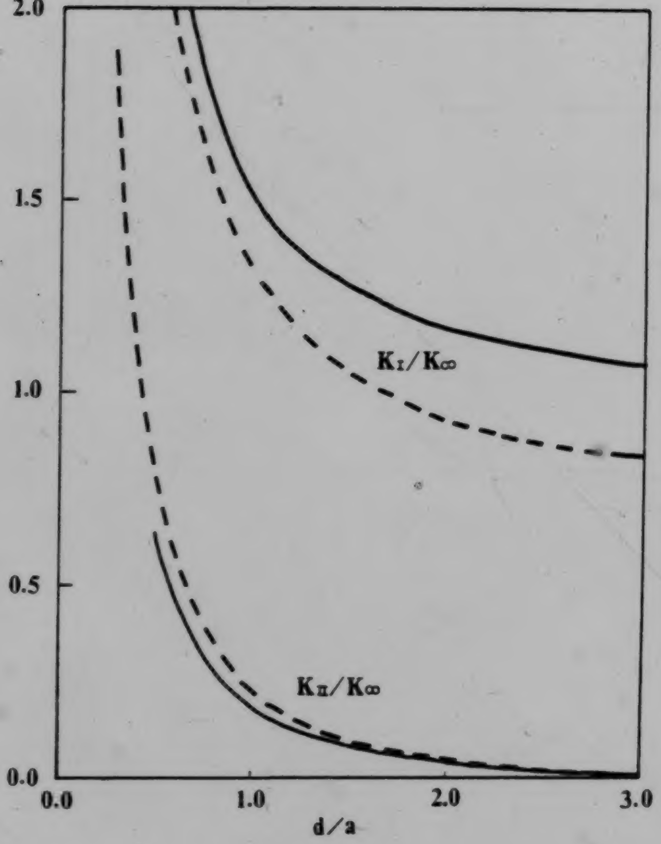

Fig.2.3.3 ..... Stress intensity factors for horizontal fractures subjected to uniform pressure (solid lines) and linear pressure (broken lines) distributions. (from Pollard et al., 1979).

is taken to be twice P in Eq.2.3.1, the total force operating in the fracture is same as that for the model of uniform pressurization. Simple computation indicates that the ratio Eq.2.3.3/Eq.2.3.1 in terms of Ki is about 0.726.

The stress intensity factor at the tips of a horizontal penny-shaped fracture is shown in Table 2.3.1, in which K_∞ is the stress intensity factor (Mode I) for a penny-shaped fracture in an infinite region (cf., Section 2.1).

Next, it is shown that fluid injection into a wellbore with a pre-existing crack of an arbitrary orientation relative to the direction of far-field stresses tends to make the cracks extend in a direction which is more nearly perpendicular to the direction of the minimum principal stress than the original plane was. This is predicted by strain energy release rate hypothesis (cf., Abou-Sayed et al., 1978). Consider a crack of length 2L oriented at an arbitrary angle α relative to the direction of the minimum principal stress, as shown in Fig.2.3.4. The stress intensity factors Ki and Kii for the pre-existing crack subjected to the internal pressure P are given by

$$K_I = (\pi L)^{\frac{1}{2}}(P - \sigma_1 \sin^2\alpha - \sigma_3 \cos^2\alpha) \tag{2.3.4}$$

$$K_{II} = (\pi L)^{\frac{1}{2}} \cdot {}^1/_2 \cdot (\sigma_1 - \sigma_3) \sin 2\alpha \tag{2.3.5}$$

(Rice, 1968), where σ_1 and σ_3 are the maximum and minimum compressive far-field principal stresses, respectively. If the crack extends in an arbitrary direction γ , the corresponding release rate $\Gamma(\gamma)$ is given by

d/a	K_I / K_∞	K_{II} / K_∞
1.05	1.2042	0.0899
1.10	1.1863	0.0822
1.20	1.1561	0.0640
1.30	1.1320	0.0514
1.667	1.0759	0.0248
2.50	1.0275	0.0082
5.00	1.00399	0.00062

a=radius of fracture
d=depth of fracture
$K_\infty = \frac{2}{\pi} P \sqrt{a}$, P=internal pressure

Table 2.3.1 ..... Stress intensity factors for a horizontal penny-shaped fracture (from Kassir and Sih, 1975, p225).

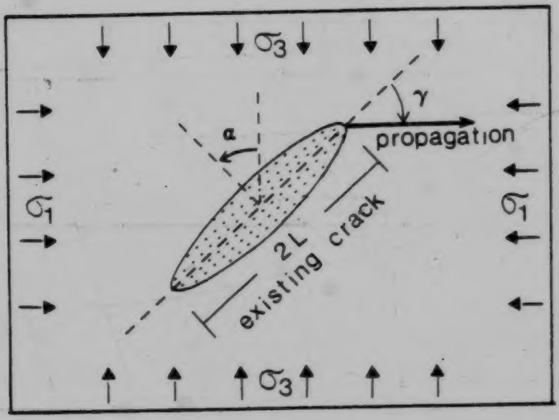
σ3
γ
α
propagation
σ1
σ1
2L
existing crack
σ3

Fig.2.3.4 ..... Skewed crack under far-field stresses and internal pressure.

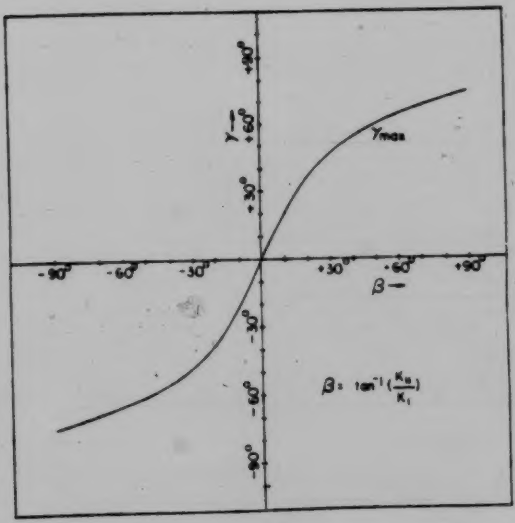

Fig.2.3.5 ..... Orientation of an extending crack which maximizes energy release rate (from Abou-Sayed et al.,1978).

$$\Gamma(\gamma) = \frac{4(1-\nu^2)}{E} \cdot \frac{1}{3+\cos^2\gamma} \cdot \left(\frac{\pi-\gamma}{\pi+\gamma}\right)^{\gamma/\pi}$$

$$\times \left[(1+3\cos^2\gamma)K_I^2 + 8\sin\gamma\cos\gamma\, K_I K_{II} + (9-5\cos^2\gamma)K_{II}^2 \right] \quad (2.3.6)$$

(Hussain et al., 1974), where E and ν denote Young's modulus and Poisson's ratio of the material, respectively. The crack will be assumed to advance in such a direction that $\Gamma(\gamma)$ becomes a maximum. Then the relationship between the direction of crack advance γ_{max} and the ratio K_{II}/K_I is given by Fig.2.3.5.

Substitution of Eqs.2.3.4 and 2.3.5 into Eq.2.3.6 reveals that Γ is proportional to the crack length. Therefore, if the crack advances at a prescribed finite value of $\Gamma(\gamma_{max})$, the conditions for such a sufficiently long open crack to be stationary are satisfied only when

$$\Gamma(\gamma) = 0 \quad \text{hence} \quad K_I = K_{II} = 0 \qquad (2.3.7)$$

From Eqs.2.3.4 and 2.3.5, this condition is expressed as

$$P = \sigma_1 \sin^2\alpha + \sigma_3 \cos^2\alpha \qquad (2.3.8)$$

and

$$(\sigma_1 - \sigma_3)\sin 2\alpha = 0 \qquad (2.3.9)$$

If σ_1 and σ_3 are not equal, Eq.2.3.9 implies that

$$\alpha = 0 \quad \text{or} \quad \alpha = \pm\pi/2$$

The former case, $\alpha = 0$, corresponds to the situation that the pressure P equals the minimum compressive stress σ_3 , whereas the latter case , $\alpha = \pm\pi/2$, corresponds to the situation that the pressure p is equal to the maximum compressive stress σ_1.

Now consider a problem; to which direction of these two stationary conditions does the pre-existing crack of neither $\alpha = 0$ nor $\alpha = \pm\pi/2$ extend more likely ? We are considering a crack tending to open due to the internal pressure, hence $K_1 > 0$. Since $\sigma_1 > \sigma_3$, Eq.2.3.5 indicates that Kii is positive for α in the interval $(0, \pi/2)$, whereas Kii is negative for α in the interval $(-\pi/2, 0)$. This observation and Fig.2.3.5 indicate that for α in the interval $(0, \pi/2)$, the predicted angle Υ of the extending crack is positive, whereas Υ is negative for α in the interval $(-\pi/2, 0)$. Consequently, this maximum energy release rate hypothesis predicts that the pre-existing crack tends to extend in a direction which is more nearly perpendicular to the direction of the minimum compressive stress.

3. Theoretical Size of Surface Deformations

In the following, a fracture is assumed to be produced in an isotropic, homogeneous, semi-infinite elastic medium.

3.1 A horizontal penny-shaped fracture

Analytical expressions for the surface deformation due to a horizontal penny-shaped fracture have been obtained by Ren Jen Sun (1969). In this fracture model, it is assumed that the surface of fracture is maintained by uniform pressure of injected fluid, and that fluid flow into the rock adjacent to the fracture is so small that the rock can be regarded as impermeable.

The surface deformations at distance r from the center of a fracture at depth d and of radius a in a semi-infinite elastic medium of Young's modulus E, Poisson's ratio ν are given by

Uplift =

$$U = f \cdot a \cdot \left(\sqrt{k}\sin\frac{\theta}{2} - \frac{d}{a\sqrt{k}}\cos\frac{\theta}{2}\right) \tag{3.1.1}$$

Horizontal displacement =

$$R = f \cdot r \cdot d \cdot \left\{ \frac{a + a\sqrt{k}\sin\frac{\theta}{2}}{\left(d + a\sqrt{k}\cos\frac{\theta}{2}\right)^2 + \left(a + a\sqrt{k}\sin\frac{\theta}{2}\right)^2} - \frac{d\sqrt{k}\cos\frac{\theta}{2} - a\sqrt{k}\sin\frac{\theta}{2} + ak\cos\frac{\theta}{2}}{\left(d\sqrt{k}\cos\frac{\theta}{2} - a\sqrt{k}\sin\frac{\theta}{2} + ak\cos\theta\right)^2 + \left(a\sqrt{k}\cos\frac{\theta}{2} + d\sqrt{k}\sin\frac{\theta}{2} + ak\sin\theta\right)^2} \right\} \tag{3.1.2}$$

Tilt =

$$T = \frac{dU}{dr} \qquad (3.1.3)$$

Horizontal strain =

$$S = \frac{dR}{dr} \qquad (3.1.4)$$

where

$$k = \left[\left(\frac{r^2}{a^2} + \frac{d^2}{a^2} - 1 \right)^2 + \left(\frac{2d}{a} \right)^2 \right]^{\frac{1}{4}} \qquad (3.1.5)$$

$$\theta = \tan^{-1}\left(\frac{2ad}{r^2+d^2-a^2} \right) \qquad (3.1.6)$$

$$f = \frac{8(1-\nu^2)}{\pi E} P \qquad (3.1.7)$$

and P is the internal pressure of fracture (Ren Jen Sun, 1969, Eqs.16 and 17).

The internal pressure P may be expressed as

$$P = P_o - \rho\gamma d \qquad (3.1.8)$$

where P_o is the injection pressure and $\rho\gamma d$ is the overburden pressure, ρ is the density of overburden and γ is gravitational acceleration. The fracture model with the assumption of uniform pressurization has a stress concentration of infinity at the edge of fracture. When the fact that the stress must be finite is taken into consideration (cf. Eq.2.1.5), the relationship between the overburden pressure, the injection pressure and the internal pressure can be written

$$P = \frac{8(1-\nu^2)}{\pi E} \left[1 - \left(\frac{P_o - \rho\gamma d}{P_o} \right)^2 \right] (P_o - \rho\gamma d) \qquad (3.1.9)$$

where P is the average of the internal pressure over the entire surface of fracture. As long as the average pressure is assumed to act uniformly on the entire surface of fracture, the analytical solutions, Eq.3.1.1-Eq.3.1.7, can be used for the calculation of the surface deformations for this model.

Green (1949) and Sneddon (1946) studied the deformation field due to a penny-shaped fracture normal to the surface subjected to the uniform internal pressure in an infinite elastic medium. In order to obtain the solution for the semi-infinite medium, we put an image source of the actual fracture at a symmetric position with respect to the free-surface, and obtain a stress field which satisfies one of the boundary conditions in terms of the stresses on the free-surface, i.e., $\sigma_{n,t}=0$ where n and t denote the normal and tangential directions of the free-surface. In this case, the other boundary condition, i.e., $\sigma_{n,n}=0$ on the free-surface remains unsatisfied. Subsequently we have to solve the so called "Boussinesq problem". Namely we need to obtain a new stress function which satisfies the boundary conditions of $\sigma_{n,t}=0$ and the normal load as equal and opposite to the normal stress resulting from the superposition of the original and image fields on the free-surface. Eq.3.1.1-Eq.3.1.7 are obtained by this procedure. Turning to the boundary conditions of the fracture plane, the image source and the new stress function give rise to additional stresses which are neither constant nor vanish on the entire fracture plane. This implies a discrepancy from the initially specified magnitude and uniformity of the internal pressure of the fracture. Accordingly Eq.3.1.1-Eq.3.1.7 are not exact solutions to the surface deformations due to the fracture normal to the surface subjected to uniform internal pressure in the semi-infinite elastic medium. In order to obtain more exact solutions, the procedure - derive another stress function which reduces the additional stresses on the fracture plane, and solve the subsequent "Boussinesq problem" - should be repeated.

Fig.3.1.1 is an example of theoretical surface deformations due to a horizontal penny-shaped fracture. General features of the surface deformations are;

(1) The maximum value of uplift occurs above the center of fracture, and the amplitude decreases monotonically to zero at infinite distance from the center of fracture.

(2) The radial displacement has zero value just above the center of fracture and increases its amplitude to reach the maximum value at some distance from the center of fracture, and after that, decreases to zero at infinity.

(3) The tilt field shows a pattern similar to that of the radial displacement except for an opposite sign.

(4) The horizontal strain has the positive maximum value just above the center of fracture and has the negative minimum value at some distance from the center of fracture, and after that, increases its amplitude gradually to zero at

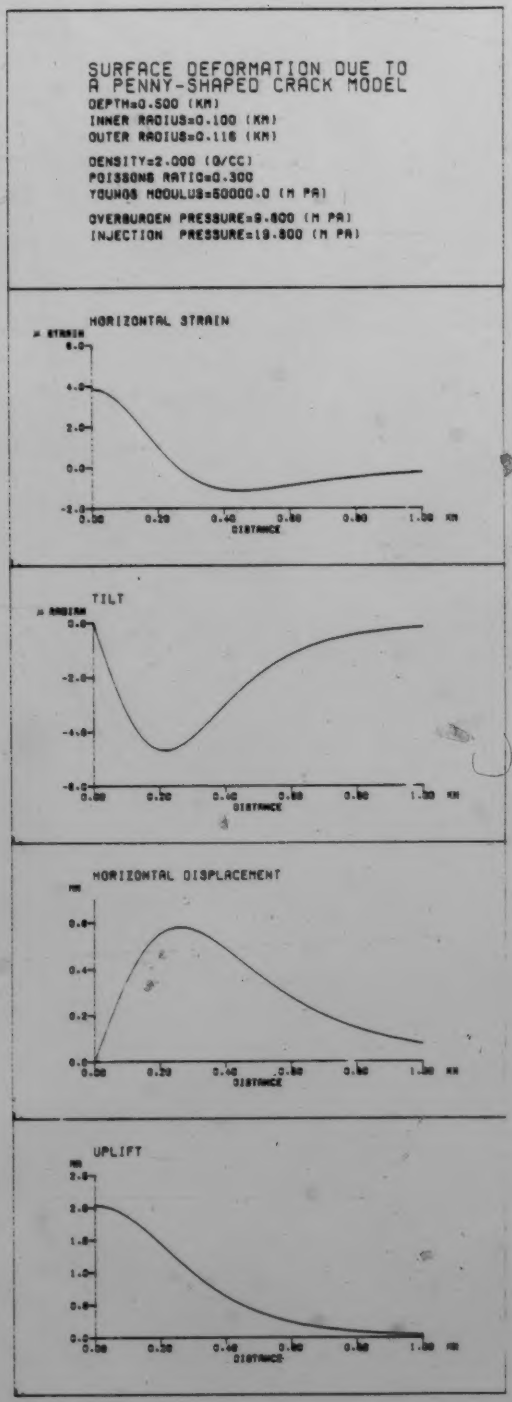

SURFACE DEFORMATION DUE TO A PENNY-SHAPED CRACK MODEL

DEPTH=0.500 (KM)
INNER RADIUS=0.100 (KM)
OUTER RADIUS=0.116 (KM)

DENSITY=2.000 (G/CC)
POISSONS RATIO=0.300
YOUNGS MODULUS=50000.0 (M PA)

OVERBURDEN PRESSURE=9.800 (M PA)
INJECTION PRESSURE=19.800 (M PA)

Fig.3.1.1 ..... Surface deformation fields due to a horizontal penny-shaped fracture.

infinity.

Figs.3.1.2a-2d show the maximum and minimum values of the uplift, horizontal displacement, tilt and horizontal strain due to a fracture with various values of radius a and depth d. The uplift and horizontal displacement fields can be expressed in the general form

$$f\ d\ g(\ a/d\ ,\ r/d\ )$$

and the tilt and horizontal strain fields, in the form

$$f\ g(\ a/d\ ,\ r/d\ )$$

where f depends only on the internal pressure and the elastic constants of material, and g denotes a functional relation of each deformation field and the geometrical parameters of a fracture and observation points. The function g relates to the shape of the surface deformation fields, and the quantity f relates to the amplitude of the fields. Therefore the quantity f will be designated as the "amplitude factor" of fracture. The amplitude factor f and the function g are non-dimensional. In Fig.3.1.2, the variation of a and d is given by the parameter a/d. The values in these figures are calculated by setting

$$f = 1.0 \quad , \quad d = 1.0 \text{ km}$$

For fractures at arbitrary depth d, the vertical axis of Fig.3.1.2a (uplift) and Fig.3.1.2b (horizontal displacement) should be multiplied by the factor d (in km).

The following descriptions hold true for fractures for which $0.05 \leq a/d \leq 1.0$, Fig.3.1.2 ..... The amplitude of extrema of the surface deformation due to a horizontal penny-shaped fracture.

a ... Maximum of uplift
b ... Maximum of horizontal displacement
c ... Maximum of tilt
d ... Maximum and minimum of strain

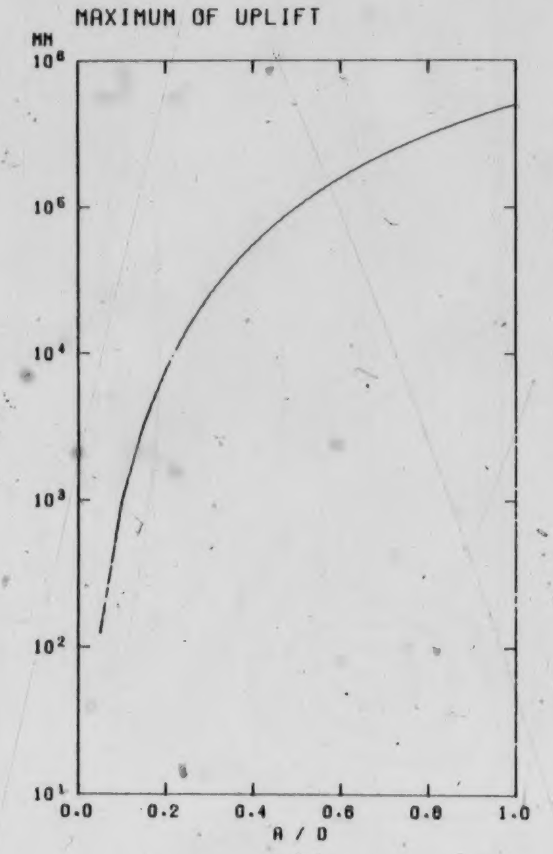

Fig.3.1.2a

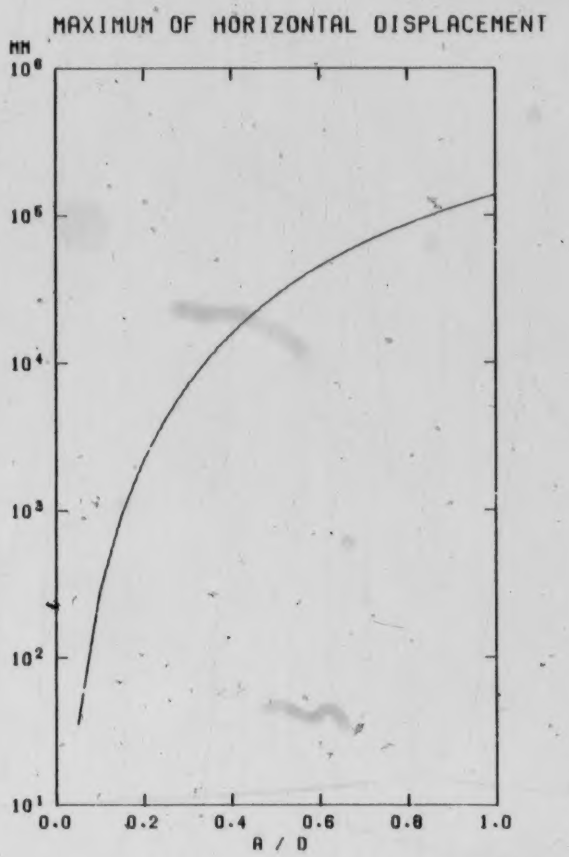

Fig.3.1.2b

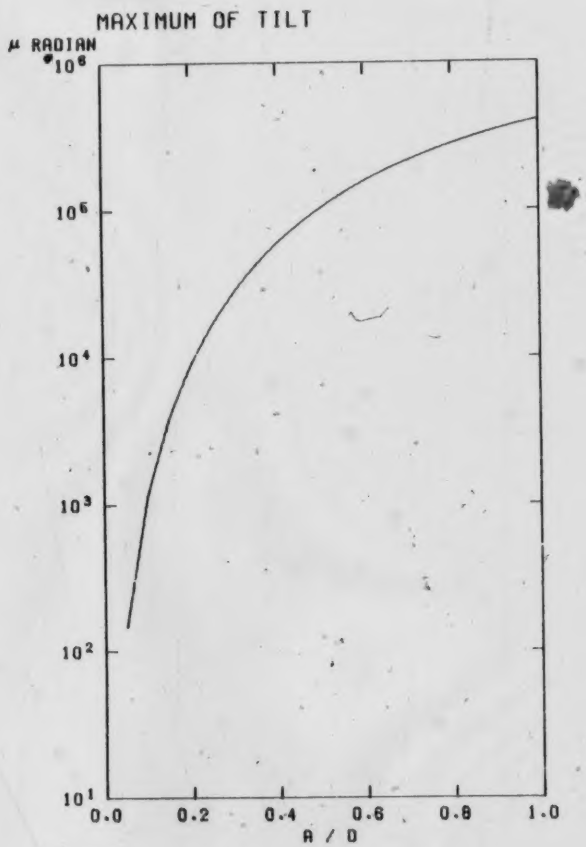

Fig.3.1.2c

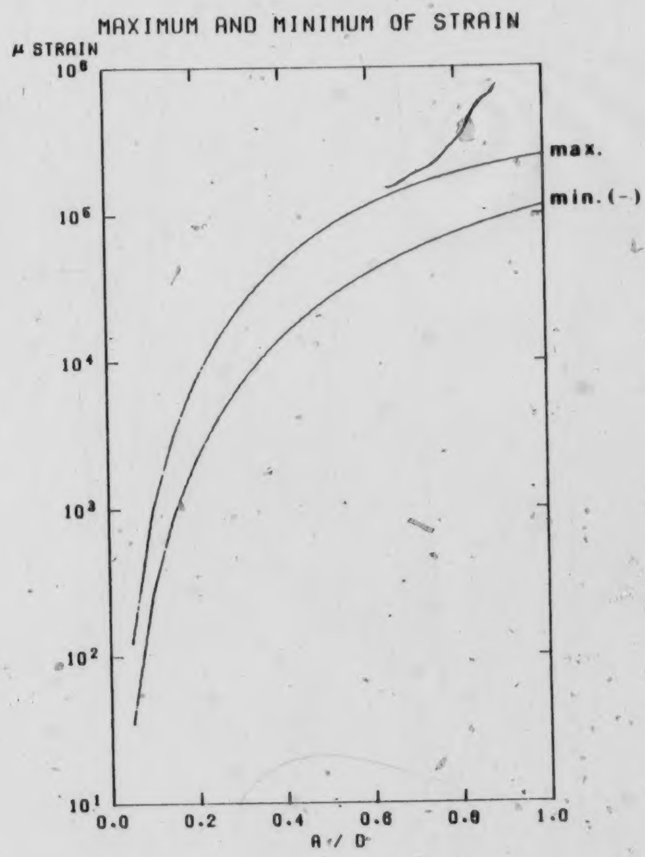

Fig.3.1.2d

$$\frac{\text{Max. of radial displacement}}{\text{Max. of uplift}} = 0.28 \pm 0.01 \qquad (3.1.10)$$

$$\frac{\text{Max. of strain } (\mu\text{strain})}{\text{Max. of tilt } (\mu\text{radians})} = 1.0(\tfrac{a}{d}=0.05) \sim 0.47(\tfrac{a}{d}=1.0) \qquad (3.1.11)$$

$$\frac{\text{Max. of uplift (mm)}}{\text{Max. of tilt } (\mu\text{radians})} = (1.0 \pm 0.2)d \qquad (3.1.12)$$

$$\frac{\text{Min. of strain}}{\text{Max. of strain}} = 0.28(\tfrac{a}{d}=0.05) \sim 0.48(\tfrac{a}{d}=1.0) \qquad (3.1.13)$$

In Eq.3.1.12, d must have the unit of km.

These relations show that the ratios depend only weakly if at all on a/d. This suggests that it is very hard to estimate a/d (or a when d is known) by the ratios of extrema of different kinds of data. Eq.3.1.10 indicates that the measurement accuracy of the radial displacements should be at least four times of that of the uplifts, from the aspect of detectability. Similarly the measurements of horizontal strain should be about twice as accurate as the tilt measurements, as shown in Eq.3.1.11. The relation of Eq.3.1.12 indicates that, when the depth of fractures is about 1 km, the magnitude of the tilts in microradians and the uplifts in millimeters is comparable, but the former becomes larger than the latter by the factor d (in km) for shallower fractures. However the above remarks hold true only when the observations are near the extrema of each deformation field. As shown later, the locations of extrema of the tilt and horizontal strain fields depend on the fracture parameters. Therefore, in the situation where the observations are restricted within a narrow region above the center of fracture, the uplift and the strain responses might yield greater detectability than others.

Fig.3.1.3 shows where the extrema in tilt, horizontal displacement (or zero strain) and horizontal strain occur in terms of various values of a/d. We might expect that the location of an extremum indicates the fracture parameter a/d, or the radius a of fracture when the depth d is known. Fig.3.1.3 shows that fractures with $a/d < 0.5$ do not yield remarkably different locations, but those with $a/d > 0.5$ yield some difference in locations which depends linearly on the parameter a/d. However, larger values of a/d do not give sharp extrema. Therefore, from the aspect of practical application, it seems hard to estimate the radius of fracture (or a/d) by finding the extrema or nodes.

Table 3.1.1 shows estimates of the magnitude of amplitude factor f for the fractures of depth 50 - 1000 m . The calculation is based on Eq.3.1.9. This table contains three cases of $\Delta P = 1$ MPa, $\Delta P = 10$ MPa and ΔP=infinity, where ΔP is the difference between the injection pressure P_0 and the overburden pressure $\rho \gamma d$, i.e.,

$$\Delta P = P_0 - \rho \gamma d \qquad (3.1.14)$$

The upper limit of f, which corresponds to the case $\Delta P = \infty$ MPa, can be estimated by the following equations. Letting x be the ratio $P_0 / \rho \gamma d$, Eq.3.1.9 can be expressed in the form

$$f = f_1 \cdot f_2 \cdot f_3$$

where

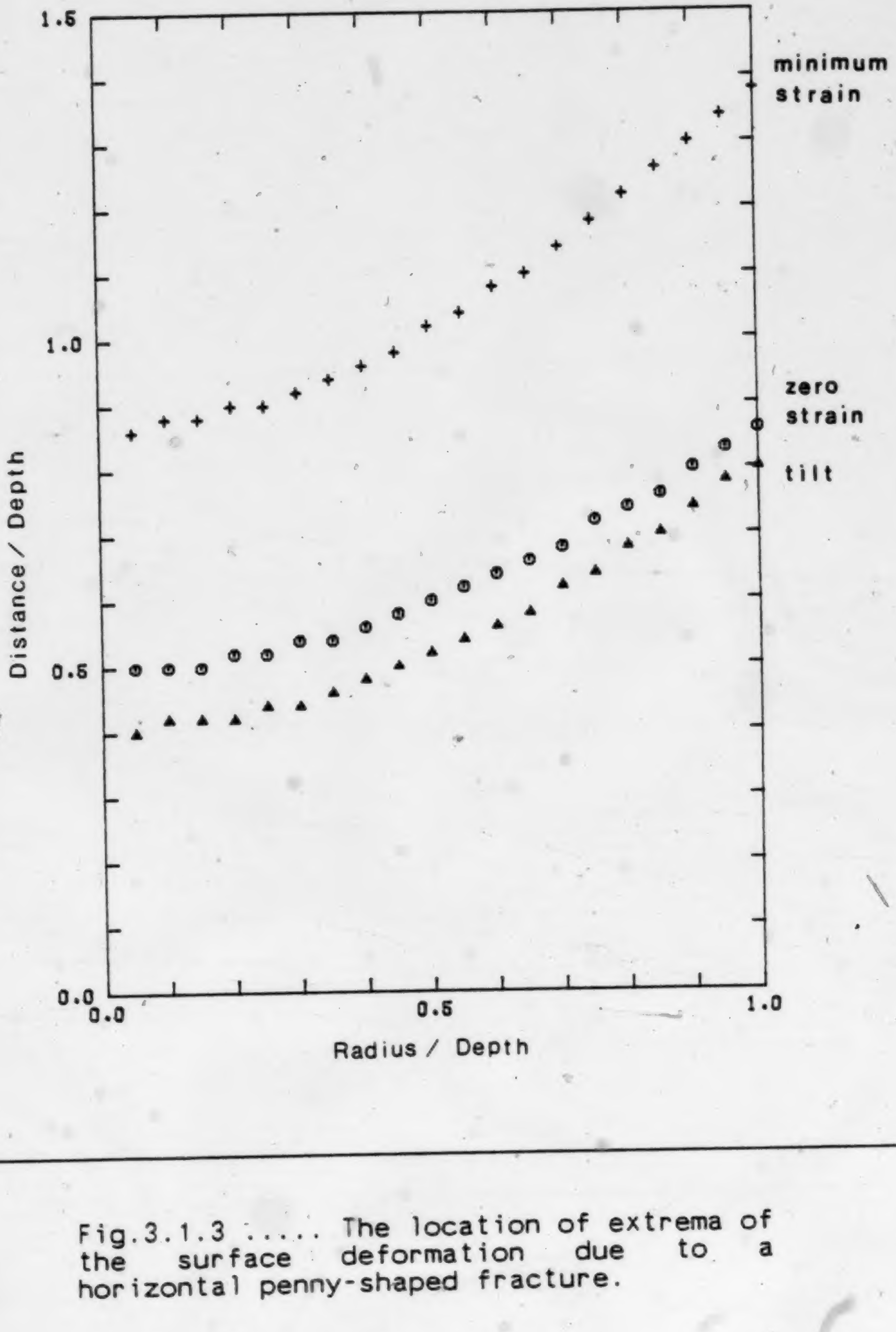

Fig.3.1.3 ..... The location of extrema of the surface deformation due to a horizontal penny-shaped fracture.

DEPTH(M)	P=1 MPA	P=10 MPA	$\Delta P=\infty$
50.	0.181E-03	0.446E-03	0.522E-03
100.	0.210E-03	0.774E-03	0.104E-02
150.	0.220E-03	0.102E-02	0.157E-02
200.	0.224E-03	0.122E-02	0.209E-02
250.	0.226E-03	0.137E-02	0.261E-02
300.	0.228E-03	0.149E-02	0.313E-02
350.	0.229E-03	0.159E-02	0.366E-02
400.	0.229E-03	0.168E-02	0.418E-02
450.	0.230E-03	0.175E-02	0.470E-02
500.	0.230E-03	0.181E-02	0.522E-02
550.	0.230E-03	0.186E-02	0.575E-02
600.	0.231E-03	0.190E-02	0.627E-02
650.	0.231E-03	0.194E-02	0.679E-02
700.	0.231E-03	0.197E-02	0.731E-02
750.	0.231E-03	0.200E-02	0.783E-02
800.	0.231E-03	0.202E-02	0.836E-02
850.	0.231E-03	0.204E-02	0.888E-02
900.	0.231E-03	0.206E-02	0.940E-02
950.	0.231E-03	0.208E-02	0.992E-02
1000.	0.231E-03	0.210E-02	0.104E-01

Table 3.1.1 ..... Estimates of the amplitude factor of the surface deformation due to a horizontal penny-shaped fracture, based on Eq.3.1.9.

$$f_0 = \rho \gamma d$$

$$f_1 = \frac{8(1-\nu^2)}{\pi E} \qquad (3.1.15)$$

$$f_2 = (2x-1)(x-1)/x^2$$

We observe that

$$f_2(x \to \infty) = 2$$

Then the upper limit of the amplitude factor is given by

$$f_{max} = 2 \cdot f_0 \cdot f_1$$

According to the fracture model from which Eq.3.1.9 derives, the radius of the fracture is expressed as a function of the internal pressure, as shown Eq.2.1.6. An infinite internal pressure gives a finite amplitude factor, but simultaneously makes the radius of fracture infinite. Therefore, the finite value of the amplitude factor does not imply finite amplitude of ground responses.

In Table 3.1.1, the density ρ, Poisson's ratio ν and Young's modulus E are so chosen that

$$\rho = 2.3 \text{ g/cc}, \quad \nu = 0.3, \quad E = 10^4 \text{MPa}$$

For most rocks, Young's modulus E ranges from 10^3 MPa (soft rock) to 10^4 MPa. As shown by Eq.3.1.15, the uncertainty of E affects estimates of the amplitude factor (hence the magnitude of surface deformations), whereas the variation of ν does not remarkably change estimates of the amplitude factor.

3.2 An Inclined Fracture

The surface deformation due to an inclined (penny-shaped or rectangular) plane fracture (Mode I, tensile) is discussed from the aspect of the computation as well as the variability of the displacement field in terms of the change of source parameters.

The displacement field was calculated by numerical integration of the fundamental equations (Maruyama, 1964, page 330) for the surface displacements due to a point source. These equations derive from elastic theory of dislocation, and assume that both Lame's constants have equal values. The following four problems are examined; (1) Variations due to spacing of points by which a fracture plane is subdivided for numerical integration. (2) Dependence of the surface displacement on the size of fracture plane. (3) Variation of the surface displacement with the dip-angle of fracture. (4) Difference of the surface displacements resulting from different dislocation distributions.

For numerical integration, the selection of lattice size is one of the problems. Table 3.2.1 shows the surface displacements calculated by using several lattice sizes. Fig.3.2.1a shows the geometry of the rectangular fracture (a=b=0.4 km) used for the calculations which were made at places along x-axis and y-axis. Supposing that the computations resulting from the finest spacing (21x21) are nearly equal to the exact values of the displacements, the

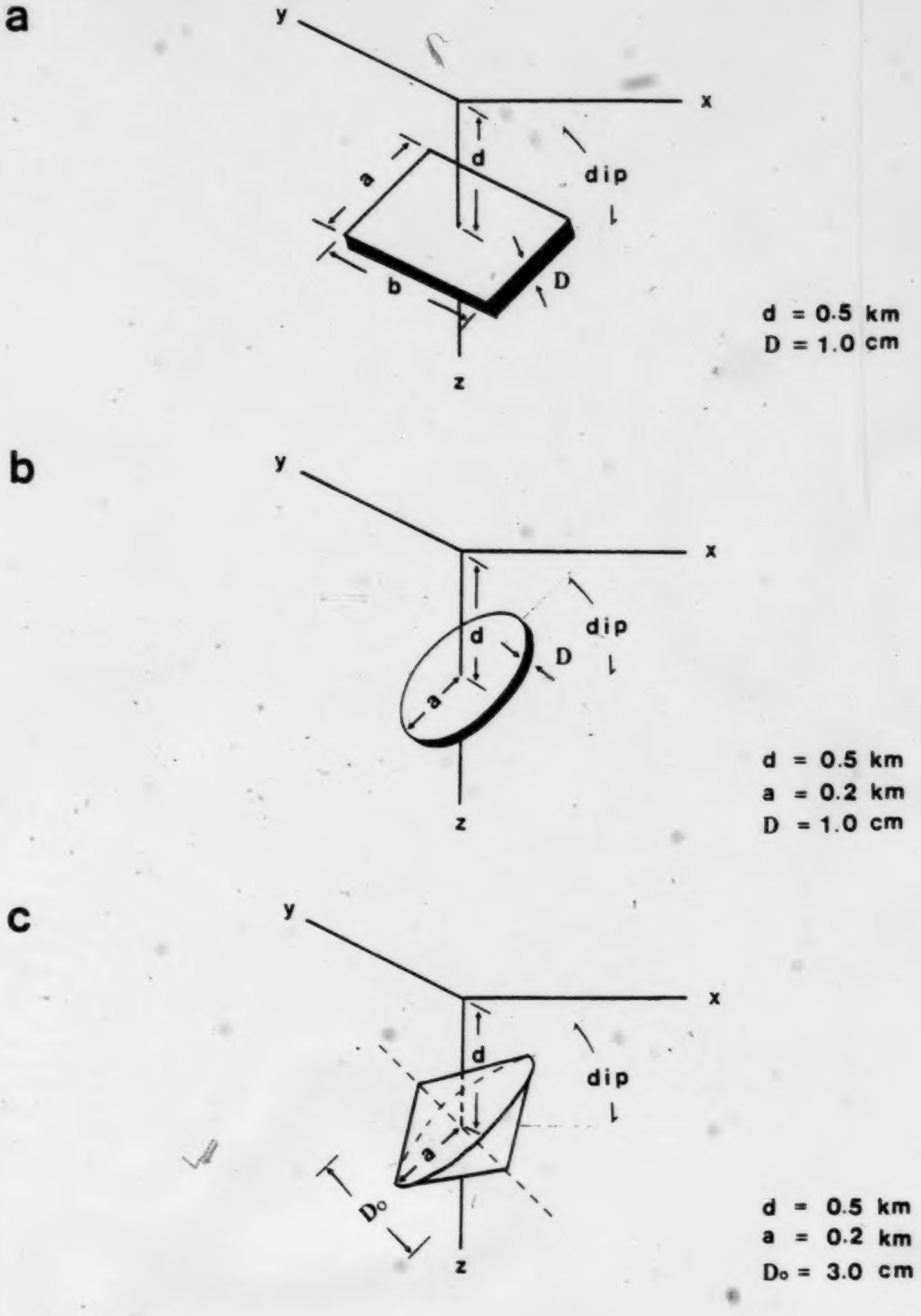
a
y
x
d
dip
a
b
D
z
d = 0.5 km
D = 1.0 cm
b
y
x
d
dip
D
a
z
d = 0.5 km
a = 0.2 km
D = 1.0 cm
c
y
x
d
dip
a
Do
z
d = 0.5 km
a = 0.2 km
Do = 3.0 cm

Fig.3.2.1 ..... The geometry of model fractures.

HORIZONTAL FRACTURE

(1) HORIZONTAL DISPLACEMENT (X-DIRECTION)

along X-axis

	0.0 KM	0.2 KM	0.4KM	0.6 KM	0.8 KM	1.0 KM
1 X 1	0.0	0.843	0.710	0.394	0.204	0.109
3 X 3	0.0	0.662	0.641	0.394	0.211	0.113
5 X 5	0.0	0.610	0.635	0.393	0.211	0.114
11 X 11	0.0	0.605	0.632	0.393	0.211	0.114
21 X 21	0.0	0.604	0.632	0.393	0.211	0.114

(2) UPLIFT

along X-axis

1 X 1	3.06	2.11	0.887	0.329	0.128	0.0547
3 X 3	2.46	1.89	0.919	0.360	0.141	0.0593
5 X 5	2.43	1.87	0.921	0.363	0.142	0.0598
11 X 11	2.41	1.86	0.921	0.364	0.142	0.0599
21 X 21	2.41	1.86	0.921	0.364	0.142	0.0600

VERTICAL FRACTURE

(1) HORIZONTAL DISPLACEMENT (X-DIRECTION)

along X-axis

	0.0 KM	0.2 KM	0.4 KM	0.6 KM	0.8 KM	1.0 KM
1 X 1	0.0	0.0911	0.393	0.508	0.472	0.394
3 X 3	0.0	0.146	0.459	0.527	0.470	0.387
5 X 5	0.0	0.153	0.464	0.528	0.469	0.387
11 X 11	0.0	0.157	0.467	0.529	0.469	0.387
21 X 21	0.0	0.157	0.467	0.529	0.469	0.387

(2) HORIZONTAL DISPLACEMENT (Y-DIRECTION)

along Y-axis

1 X 1	0.0	0.119	0.133	0.101	0.0695	0.0476
3 X 3	0.0	0.120	0.137	0.102	0.0696	0.0474
5 X 5	0.0	0.121	0.137	0.102	0.0696	0.0474
11 X 11	0.0	0.121	0.137	0.102	0.0696	0.0474
21 X 21	0.0	0.121	0.137	0.102	0.0696	0.0474

(3) UPLIFT

along X-axis

1 X 1	-0.255	0.110	0.393	0.346	0.234	0.148
3 X 3	-0.258	0.173	0.397	0.321	0.213	0.136
5 X 5	-0.259	0.180	0.397	0.318	0.212	0.135
11 X 11	-0.259	0.183	0.396	0.317	0.211	0.135
21 X 21	-0.259	0.183	0.396	0.317	0.211	0.135

(4) UPLIFT

along Y-axis

1 X 1	-0.255	-0.180	-0.0681	-0.00637	0.0177	0.0248
3 X 3	-0.258	-0.186	-0.0682	-0.00415	0.0195	0.0260
5 X 5	-0.259	-0.186	-0.0680	-0.00394	0.0196	0.0261
11 X 11	-0.259	-0.187	-0.0680	-0.00384	0.0197	0.0261
21 X 21	-0.259	-0.187	-0.0680	-0.00382	0.0197	0.0261

UNIT = MM

Table 3.2.1 ..... Dependence of computations of surface displacements due to a rectangular fracture on spacings of points in numerical integration.

crudest spacing (3x3) in this analysis yields a maximum discrepancy of less than 10 percent of the exact values, and a spacing of (5x5) reduces the maximum discrepancy to a few percent. The assumption of a point source (1x1) results in the maximum discrepancy of about 50 percent. The spacings of (3x3) and (5x5) are about 0.26 x depth and 0.16 x depth of the fracture, respectively. In the following calculations, all the grids are square and grid intervals are taken to be 0.08 km.

Fig.3.2.2 shows the variation of the shape of the displacement fields (uplift and x-componenent of horizontal displacement) in terms of the change of one of the size parameters of the fracture. The calculations are based on rectangular fractures (horizontal and vertical) with a fixed value of a (=0.4 km) and two different values of b (=0.24 km and 1.68 km). The profiles in Fig.3.2.2 are along x-axis in Fig.3.2.1.

Fig.3.2.2a shows the normalized amplitudes relative to the maximum value for the uplifts due to a horizontal fracture. The horizontal displacements due to a horizontal or a vertical fracture and the uplifts due to a vertical fracture respectively do not show maximum amplitudes at fixed coordinates, which do not necessarily coincide with one of the calculation points specified. As a reference, the horizontal displacements due to the horizontal fracture, normalized by the maximum amplitude of the calculations, are shown in Fig.3.2.2b. Fig.3.2.2c shows the uplifts due to the

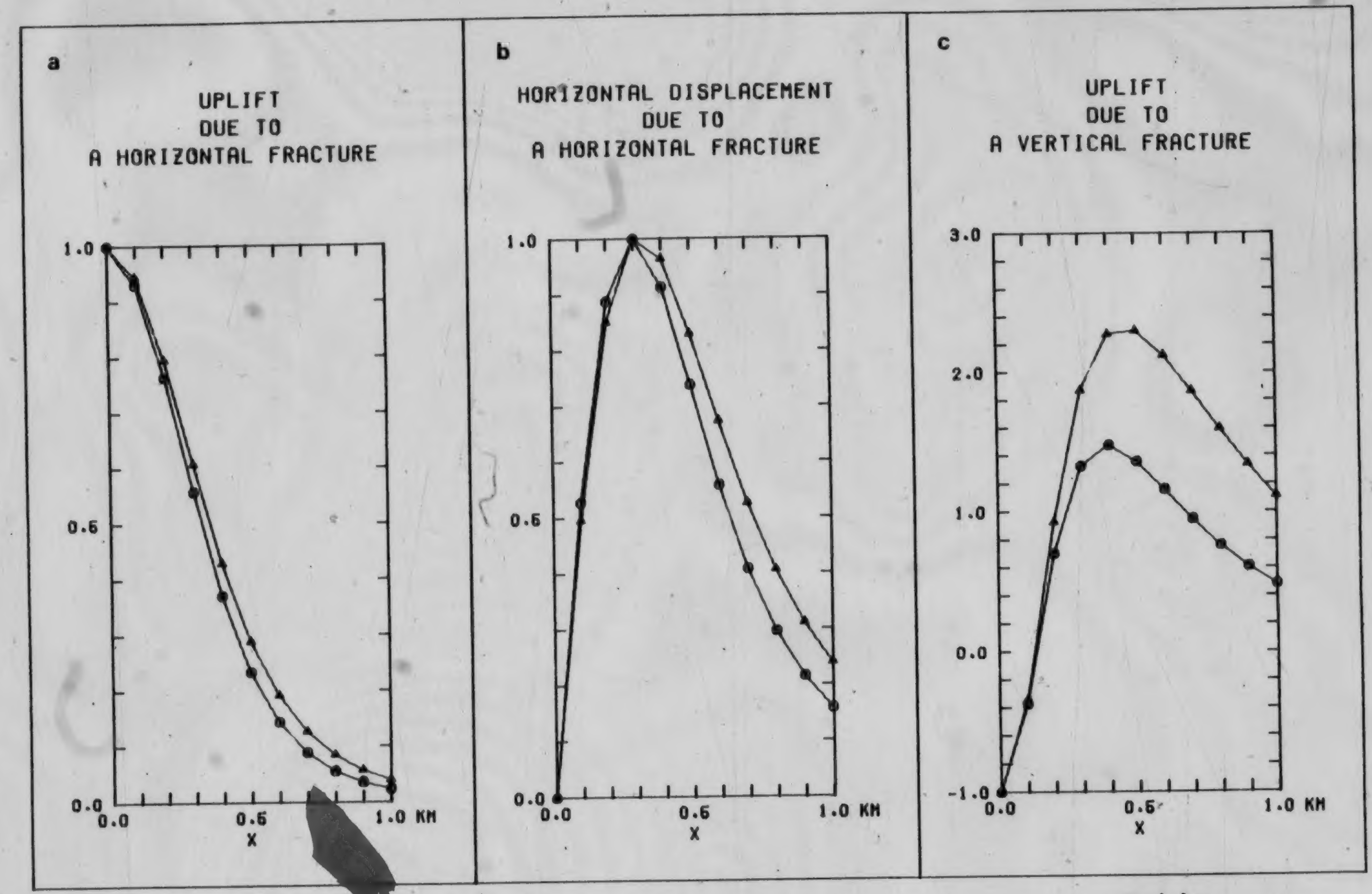

Fig.3.2.2 ..... Variation of the shape of displacement fields in terms of a change of a size parameter of a rectangular fracture.

a = 0.4 km
b = 0.24 km (○)
1.68 km (△)

vertical fracture, normalized by the amplitude at the place above the center of the fracture.

It can been seen from Fig.3.2.2 that, without regard to the difference of the size parameter b, the resulting displacement fields have an almost similar shape along the profile, which is perpendicular to the direction of the size parameter b. In order to examine the similarity of the shapes of the two displacement fields resulting from different values of b, we may evaluate the cross correlation of these two data arrays. The cross correlation for each of the four different displacement fields is shown in Table 3.2.2, which demonstrates that the shape of the surface displacements along the profile depends only weakly if at all on the size b. It is also observed from Table 3.2.2 that the vertical fracture can reflect the change of the size parameter b in the shape of the surface displacement fields more sensitively than the horizontal fracture does.

The above observations suggest that, as long as observations are made along such a profile, they do not provide enough information to determine the size parameter b. In order to estimate this dimension of the fracture, observations in the direction of fracture strike (y-axis in Fig.3.2.1) should be available. On the other hand, the above mentioned weak dependence implies that a 2-D fracture model can be used for the determination of the other source parameters. Even if the overall shape of a deformation field depends to some extent on the variation of b (for example,

	Vertical Fracture	Horizontal Fracture
Uplift	0.9806	0.9982
Horizontal Displacement	0.9894	0.9941

Table 3.2.2 ..... Cross-correlations of two displacement fields resulting from different values of the size parameter b.

the uplifts due to a vertical fracture shown in Fig.3.2.2c, which yield the lowest correlation in Table 3.2.2), the shape of the deformation field over a relatively small measurement area (for example, x=0.0 - 0.2 km) can become independent of variation of b, and the relative amplitudes can be expected to be conserved. If the deformation field over the small area responds well to changes of the other source parameters such as length a and dip-angle of the fracture, 2-D fracture models can be used for the determination of these parameters. It should, however, be taken into consideration that the small size of a must not result in significant change in the shape of displacement fields due to changes of its value, and that the estimate of displacement dislocation or driving pressure directly depends on the absolute magnitude of observed displacements. The maximum amplitude of the displacement fields due to each of the fractures with various values of b is shown in Table 3.2.3.

Fig.3.2.3 shows the uplift, horizontal displacement, tilt and horizontal strain fields due to a penny-shaped fracture with a dip-angle of 60 degrees, radius 0.2 km and the geometry shown in Fig.3.2.1b. The latter two fields were calculated by applying bicubic spline analysis to the former two fields, respectively (IMS Library, Subs. IBCICU and DBCEVU).

Figs.3.2.4a and 4b illustrate the profiles of the uplift and the horizontal displacement (x-component) along

	Vertical Fracture		Horizontal Fracture	
Size Parameter b (km)	Uplift (mm)	Horizontal Displacement (mm)	Uplift (mm)	Horizontal Displacement (mm)
b=0.24	0.252 (-0.171)	0.328	(1.57)	0.439
b=0.40	0.397 (-0.259)	0.528	(2.43)	0.690
b=0.88	0.678 (-0.382)	0.978	(3.89)	1.17
b=1.68	0.864 (-0.376)	1.34	(4.49)	1.41

( ) : at x=0

Table 3.2.3 ..... Variation of the maximum amplitude of surface displacements with changes of the size parameter b.

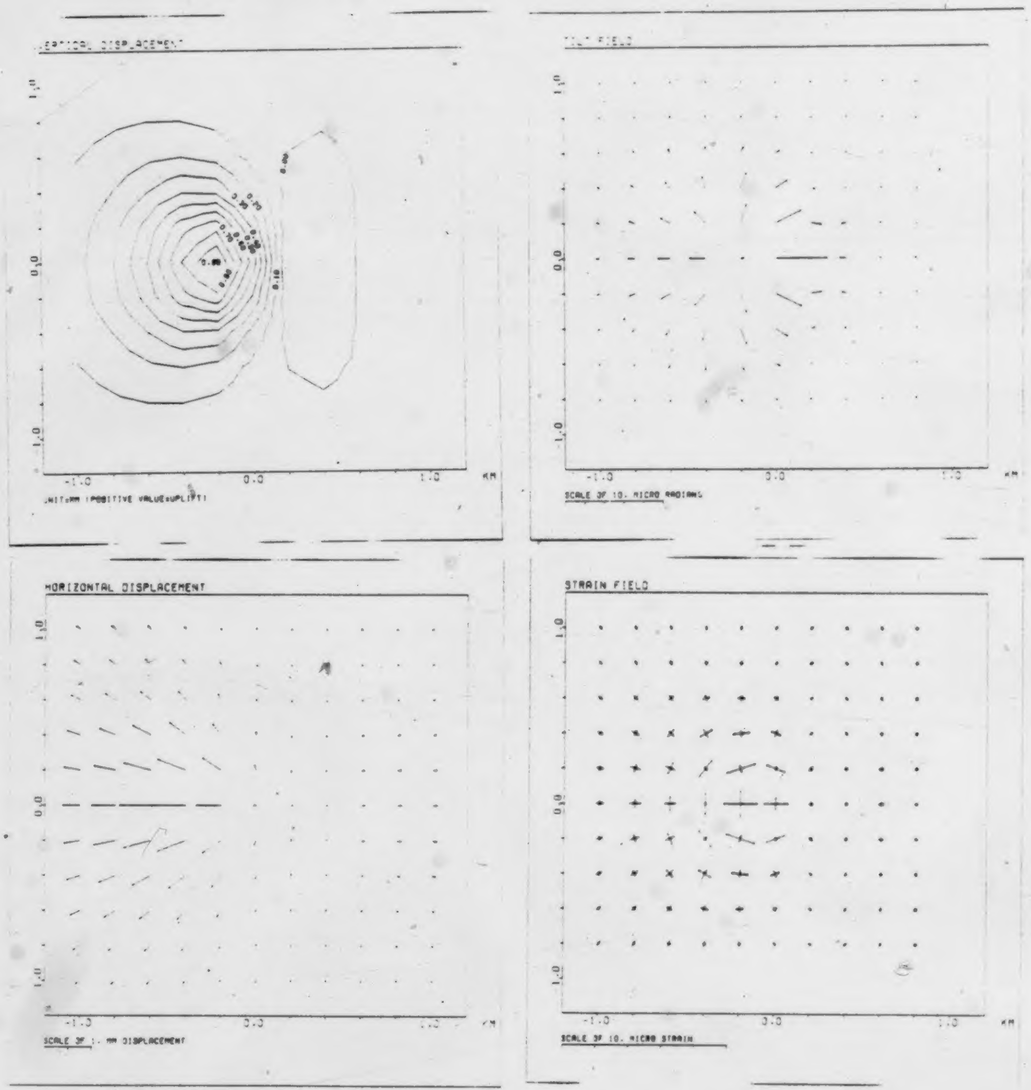

Fig.3.2.3 ..... Surface deformation fields due to an inclined penny-shaped fracture with a dip-angle 60 degrees and characterized by a constant displacement dislocation.

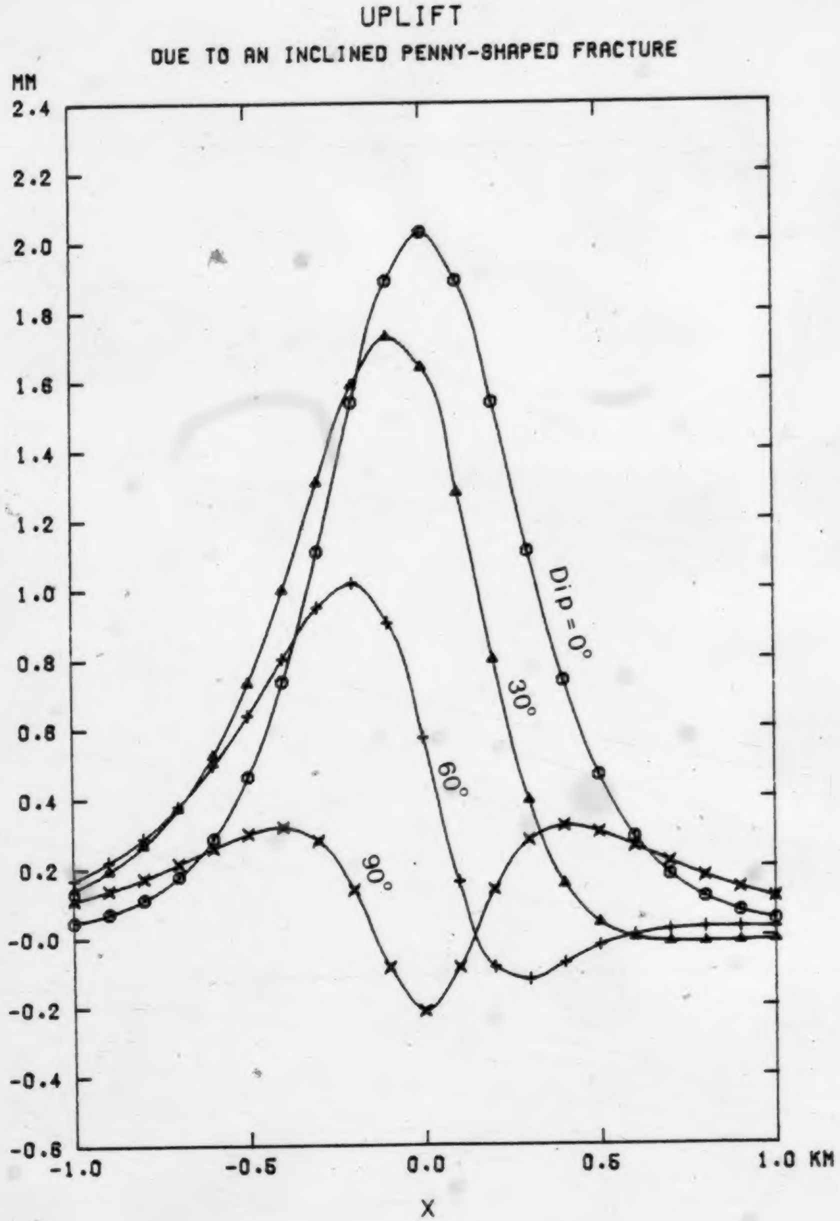

Fig.3.2.4a ..... Variation of surface uplifts due to an inclined penny-shaped fracture with various dip-angles.

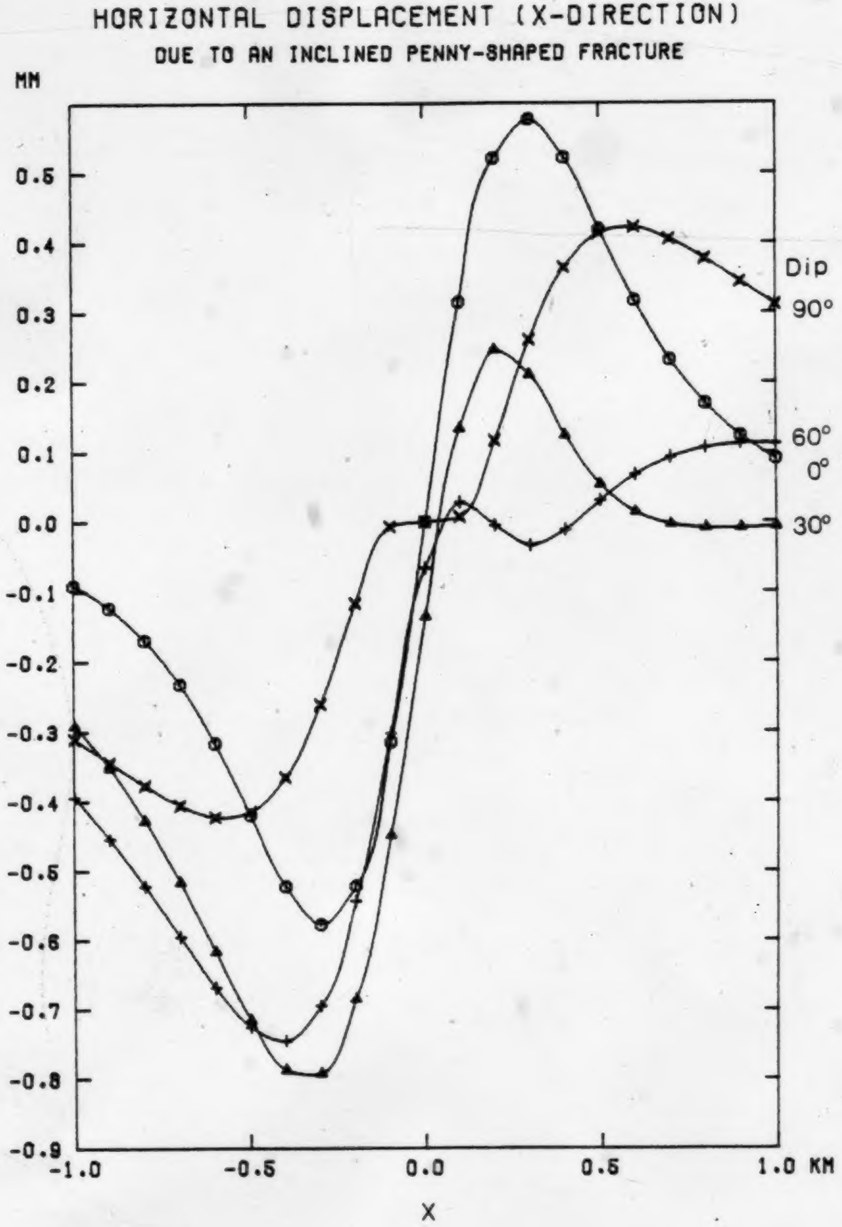

Fig.3.2.4b ..... Variation of surface displacements (horizontal) due to an inclined penny-shaped fracture with various dip-angles.

the x-axis due to a fracture with the same geometry as the one shown in Fig.3.2.1b and with various dip-angles (Dip=0, 30, 60 and 90 degrees). These figures show that the displacement fields due to an inclined fracture are very sensitive to the change of dip-angle.

The assumption of constant displacement dislocation on the plane of fracture is at variance with real conditions. Here the displacement dislocation will be given by the symmetric and linear distribution

$$D(r) = D_0 - \Delta D|r| \quad , \quad 0 \leq |r| \leq a$$

where r is distance from the center of fracture to the center of grid cell, and a is the radius of fracture (Fig.3.2.1c).

Fig.3.2.5 shows the difference between the magnitudes of the surface displacements due to each of the two model fractures, one of which is characterized by the constant displacement dislocation and the other is by the symmetric, linear displacement dislocation. The geometry of the former model fracture is same as one in Fig.3.2.1b, and the distribution of displacement dislocation for the latter model was given by D_0 =30 mm and ΔD=30mm/0.2km, which yields an identical cavity for the two model fractures.

In Fig.3.2.5, a square in each grid represents a calculation point, and the shadow shows the degree of the difference in percent between the amplitudes of the resulting two displacement fields. A large difference of the amplitudes occurs at the places where the displacement is

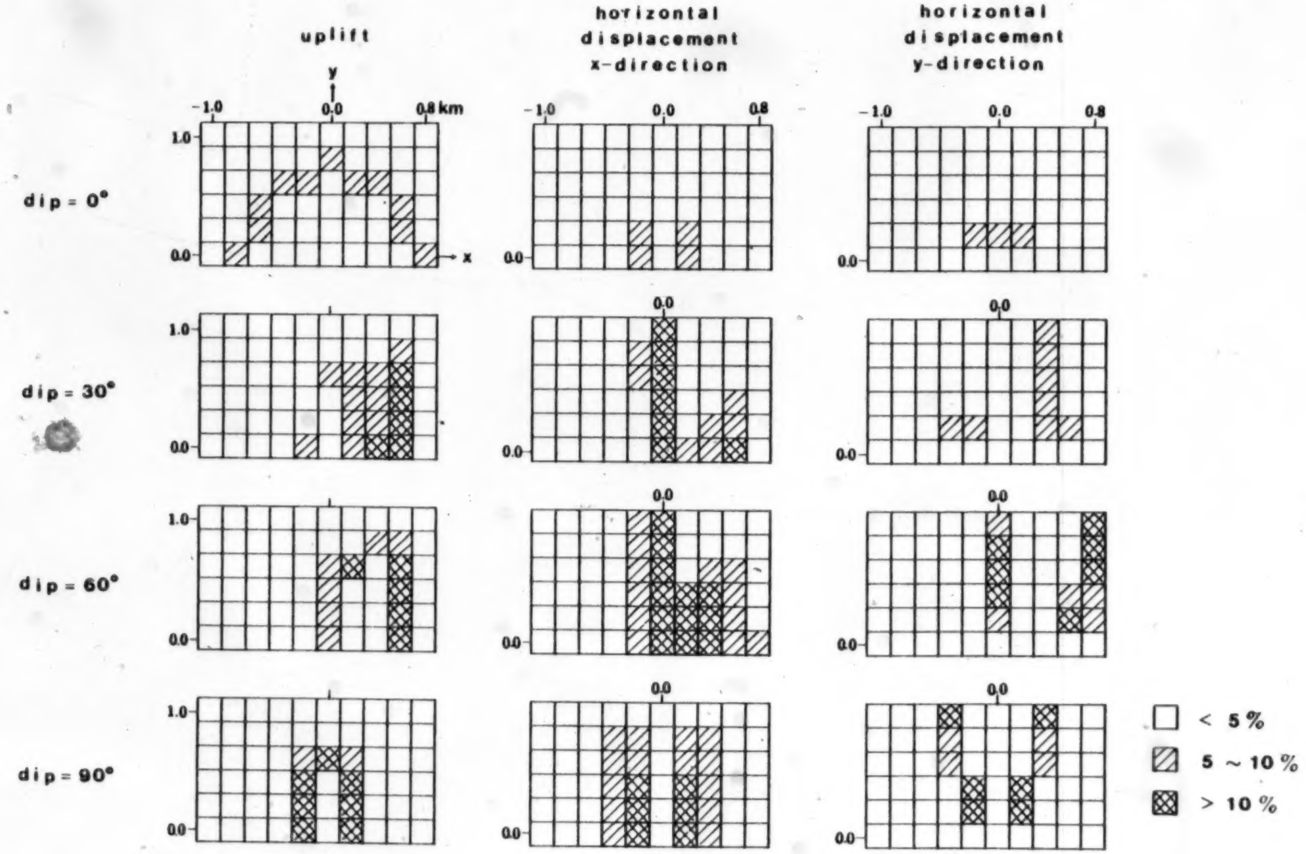

Fig.3.2.5 ..... Difference of surface displacements resulting from different dislocation distributions, constant and linear symmetric.

very small or the spatial gradient of the fields is steep.

In general, changes in the displacement dislocation on the fracture plane do not significantly change the overall shape or the amplitude of the surface displacements. This implies that appropriate selection of the observation points for an inversion analysis permits us to adopt the simple fracture model characterized by constant displacement dislocation. It is also seen from Fig.3.2.5 that, if strike and dip direction of a fracture can be inferred roughly in an experimental site, observations over the half-area in the dip direction across the strike above the fracture center (i.e., the region of $x < 0$ in Fig.3.2.1) might provide useful information for an analysis based on the simple dislocation model. The assumption of uniform pressurization in a fracture results in the separation of fracture walls having elliptical cross section. The characterization of displacement dislocation distribution by an elliptical form can be easily assumed to yield displacement fields similar to those resulting from a constant displacement dislocation distribution.

The above results are concerned with a particular case, (a typical length of a fracture)/(depth)=0.4. The variability of the surface deformation fields in terms of changes of the source parameters such as dip-angle and dislocation distribution should be examined in view of the methods which will be used for inversion analyses.

3.3 A Shear Fault Model

In the previous two sections, surface deformation has been discussed by assuming that a tensile fracture will be produced by hydraulic fracturing. As described in Chapter 2, there is also a possibility that hydraulic fracture breaks out as shear failure or as combination of shear and tensile failures. It is necessary to understand the ground response associated with the presence of shear cracks.

Analytical expressions for the surface displacements due to an inclined rectangular shear fault model with constant slip have been obtained by Manshinha and Smylie (1971), under the simplification that both Lame's constants are equal. An example of the surface deformation fields due to this fracture model is shown in Fig.3.3.1. The tilt and horizontal strain fields were calculated by applying bicubic spline analysis to the uplift and horizontal displacement fields, respectively.

We have to observe that the tilt and uplift fields in Fig.3.3.1 show roughly circular shapes. If we assume that hydraulic fracturing must always cause tensile failure, we would incorrectly infer from such roughly circular deformation fields that the induced fracture must be horizontal and have a circular or square shape. The example in Fig.3.3.1 also demonstrates that measurements of the horizontal displacement and strain fields are indispensable to determine source parameters of the fracture. These suggest that use of a particular kind of deformation

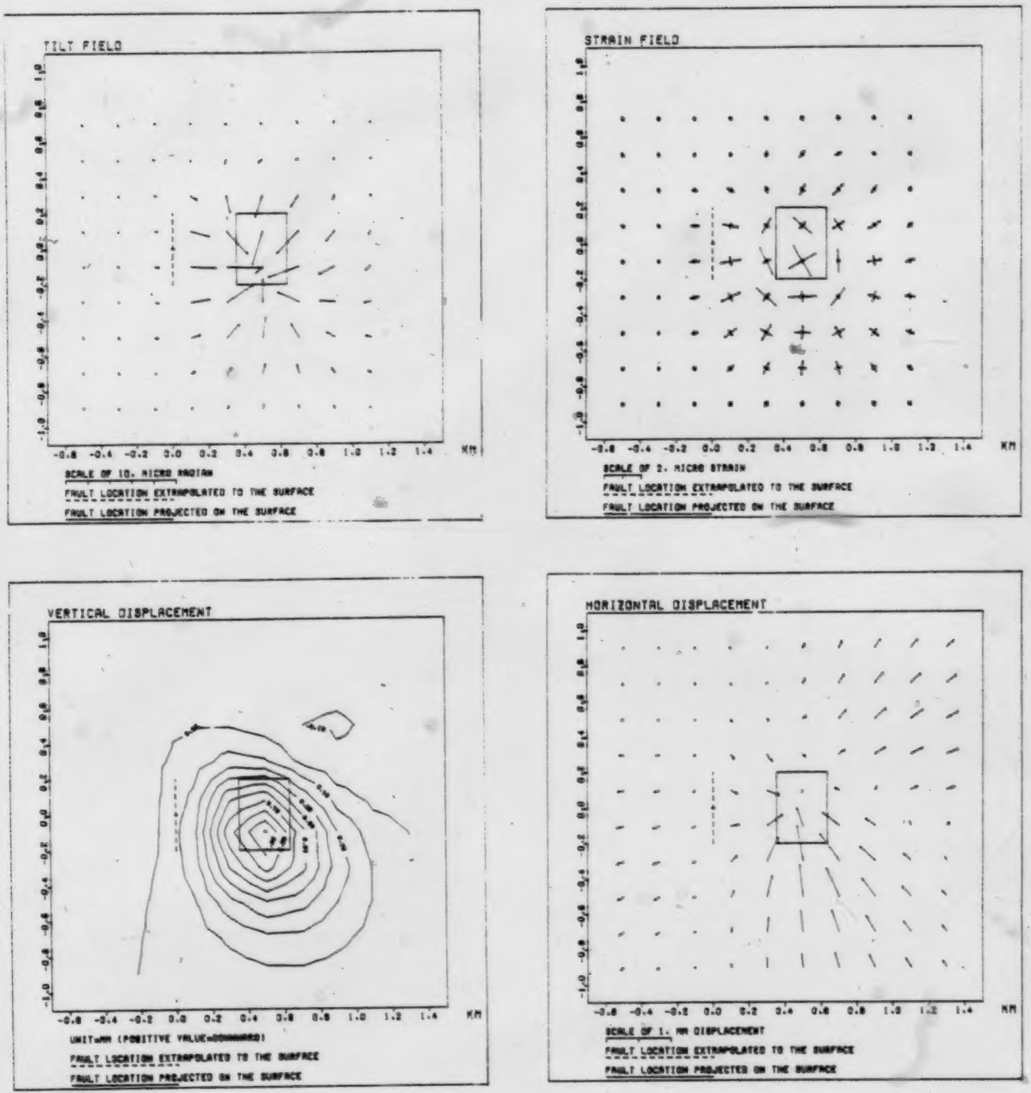

SEISMIC FAULT MODEL
FAULT PARAMETERS
SLOPE DISTANCE TO THE TOP =0.5 (KM)
SLOPE DISTANCE TO THE BOTTOM=0.9 (KM)
STRIKE SLIP=0.7 (CM) LEFT LATERAL
DIP SLIP=0.7 (CM)
DIP ANGLE=45.0 (DEGREE)

Fig.3.3.1 ..... Surface deformation fields due to an inclined rectangular shear fault model.

measurements, limitation of the number and inadequate deployment of measurement points can not provide enough information to delineate the form of fractures.

4. Determination of Source Parameters of a Horizontal Penny-shaped Fracture

4.1 Basic Procedure

One of the possible measurements at a measuring point at distance r from the center of a fracture of radius a, amplitude factor f and at depth d can be expressed in the form

$$G = f\,g(a, d, r)$$

As seen from Eq.3.1.1-Eq.3.1.7, the function g (and G) are highly non-linear with respect to the unknown parameters, a and d. The depth of fracture, d, may be usually regarded as a known parameter because the depth of formation of the fracture is controlled. However, there is no evidence that the fracture is induced at the position centering around the depth of fracturing operation. Therefore it is more general to regard the depth of fracture as one of the unknown parameters.

For simplicity, it is assumed that the depth is a known parameter. The function g is still non-linear with respect to the parameter a. Here we observe that the parameter f appears linearly in the observation equation. We assume several arbitrary values of a, for example, at an increment of Δa, and apply the least-squares procedure to a set of measurements. We can determine f for each of the assumed values of a. Then we obtain the least-squares errors resulting as a function of a, E(a). We may expect a particular value of a which yields the minimum value of E(a). This value of a might possibly indicate the rough estimate of the actual radius of the fracture. If the observed data is noise-free, this particular value of a should indicate the exact value (within the certainity of Δ a) of the fracture radius. In practice, we can not expect any field data without noise. Here I discuss the degree of resolution for the fracture radius when measurements are disturbed by noise. In other words, the problem is to understand how well the surface deformation delineates the changes of the source parameters.

4.2 Resolution - Basic Concept

Let a_0 and $\overset{o}{f}$ respectively be the true value of the radius and the amplitude factor of a fracture considered. Suppose one of the possible measurements at the j'th measuring point of distance r yields the value G'_j due to the fracture. We can express G'_j in terms of the actual response of the surface, $\overset{o}{f}\,\overset{o}{g}_j$, and a "noise component", N, in the form

$$G'_j = \overset{o}{f}\,\overset{o}{g}_j + N_j \tag{4.2.1}$$

where

$$\overset{o}{g}_j = g(\, a_0 \,,\, r_j \,)$$

When we assume an arbitrary value of a, we have the model equation

$$G_j = f\, g(\, a \ , r_j\,) =: f\, \overset{\bullet}{g}_j \qquad (4.2.2)$$

in which the unknown parameter f appears linearly. Then we can apply the least-squares procedure to a set of measurements G'_j , $j=1\sim J$, in terms of the model equation.

$$\begin{aligned} &E(a_\circ, a) = \sum_j (\, G'_j - f\overset{\bullet}{g}\,)^2 \rightarrow 0 \\ &\partial E/\partial a = 0 \end{aligned} \qquad (4.2.3)$$

It is straightforward to show

$$f = \frac{\sum (G_j' \cdot \overset{\bullet}{g}_j)}{\sum (\overset{\bullet}{g}_j)^2} = \frac{\sum (\overset{\circ}{f}\overset{\circ}{g}_j + N_j)\overset{\bullet}{g}_j}{\sum (\overset{\bullet}{g}_j)^2} \qquad (4.2.4)$$

Substitution of Eq.4.2.4 into Eq.4.2.3 yields the corresponding least-squares error

$$E(a_\circ, a) = \sum_j \left\{ G_j' - \frac{\sum_k (G_k' \overset{\bullet}{g}_k)}{\sum_k (\overset{\bullet}{g}_k)^2}\, \overset{\bullet}{g}_j \right\}^2 \qquad (4.2.5)$$

$$= \sum_j (\overset{\circ}{f}\overset{\circ}{g}_j + N_j)^2 - \frac{\left\{ \sum_k (\overset{\circ}{f}\overset{\circ}{g}_k + N_k)\overset{\bullet}{g}_k \right\}^2}{\sum_k (\overset{\bullet}{g}_k)^2} \qquad (4.2.6)$$

Using the notation for inner product

$$\langle A, B \rangle = \sum_j (A_j B_j) \qquad (4.2.7)$$

Eq.4.2.6 becomes

$$\begin{aligned} E(a_\circ, a) = \overset{\circ}{f}{}^2 &\left\{ \langle \overset{\circ}{g}, \overset{\circ}{g} \rangle - \frac{\langle \overset{\circ}{g}, \overset{\bullet}{g} \rangle^2}{\langle \overset{\bullet}{g}, \overset{\bullet}{g} \rangle} \right\} \\ +2f &\left\{ \langle \overset{\circ}{g}, N \rangle - \frac{\langle \overset{\circ}{g}, \overset{\bullet}{g} \rangle \langle \overset{\bullet}{g}, N \rangle}{\langle \overset{\bullet}{g}, \overset{\bullet}{g} \rangle} \right\} \\ + &\left\{ \langle N, N \rangle - \frac{\langle \overset{\bullet}{g}, N \rangle^2}{\langle \overset{\bullet}{g}, \overset{\bullet}{g} \rangle} \right\} \end{aligned} \qquad (4.2.8)$$

Substitution of $\overset{\circ}{g} = \overset{\bullet}{g}$ into Eq.4.2.8 yields

$$E(a_0,a_0) = \langle N,N \rangle - \frac{\langle \dot{g},N \rangle^2}{\langle \dot{g},\dot{g} \rangle} \qquad (4.2.9)$$

$E(a_0,a_0)$ corresponds to the least-squares error with respect to the true value of the fracture radius. From Eq.4.2.8 and Eq.4.2.9, we have

$$\begin{aligned} E(a_0,a) - E(a_0,a_0) = {} & \mathring{f}^2 \left(\langle \mathring{g},\mathring{g} \rangle - \frac{\langle \mathring{g},\dot{g} \rangle^2}{\langle \dot{g},\dot{g} \rangle} \right) \\ & + 2\mathring{f} \left(\langle \mathring{g},N \rangle - \frac{\langle \mathring{g},\dot{g} \rangle \langle \dot{g},N \rangle}{\langle \dot{g},\dot{g} \rangle} \right) \end{aligned} \qquad (4.2.10)$$

In Eq.4.2.10, the first term on the right hand side is always positive, whereas the sign of the second term can not be determined definitely because this term depends on the nature of function g and noise N. This suggests that $E(a_0,a)$ does not necessarily have the minimum value at $a=a_0$ (a_0 is the true value of the fracture radius).

Fig.4.2.1 schematically illustrates $E(a_0,a)$ and the concept of the resolution relating to this inversion scheme. In the practical analysis of the actual measurements G', the curve of $E(a_0,a)$ is obtained by calculating Eq.4.2.5, and eventually represented as discrete data series corresponding to discretely specified values of a.

Suppose we know the noise level, $\langle N,N \rangle$. We may represent the noise level by a horizontal straight line as shown in Fig.4.2.1. The curve of $E(a_0,a)$ and the line $\langle N,N \rangle$ should yield intersections, for example, at $a=a_1$ and $a=a_2$. We can not judge which point on the curve of $E(a_0,a)$

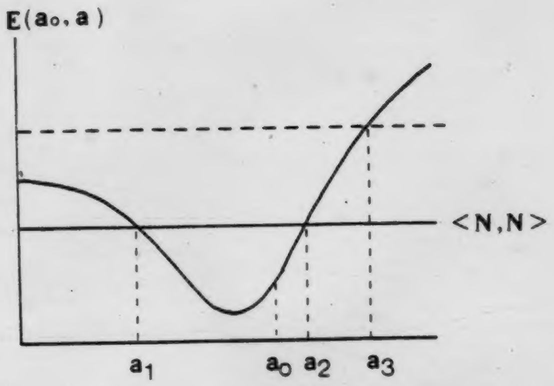

Fig.4.2.1 ..... The least-squares error as a function of an unknown non-linear parameter a.

corresponds to the true value of a, but from Eq.4.2.9 we understand just that the true value of a (=a_0) must lie so that

$$a_1 < a_0 < a_2$$

If the noise level is high, for example, as illustrated by the broken line in Fig.4.2.1,

$$0 < a_0 < a_3$$

In this case, the lower limit of the estimate of the fracture radius equals zero.

Here we will examine the range of a which satisfies the condition

$$E(a_0, a) < E(a_0, a_0) \qquad (4.2.11)$$

Eq.4.2.6 indicates that $E(a_0,a)$ has the minimum value zero when

$$\begin{aligned} & G_j' = \mathring{f}\mathring{g}_j + N_j = 0 , \quad j=1\sim J \\ \text{or} \quad & G_j' = \mathring{f}\mathring{g}_j + N_j = \pm\alpha\dot{g}_j , \quad j=1\sim J \end{aligned} \qquad (4.2.12)$$

where α is introduced as a constant. Substituting Eq.4.2.12 in the form

$$\mathring{g}_j = -N_j/\mathring{f} \quad \text{or} \quad \mathring{g}_j = (\pm\alpha\dot{g}_j - N_j)/\mathring{f} \qquad (4.2.13)$$

into the second brace of Eq.4.2.8 , it follows that

$$\begin{aligned} E(a_0, a) = {} & \mathring{f}^2 \left(\langle\mathring{g},\mathring{g}\rangle - \frac{\langle\mathring{g},\dot{g}\rangle^2}{\langle\dot{g},\dot{g}\rangle} \right) \\ & - \left(\langle N,N\rangle - \frac{\langle\mathring{g},N\rangle^2}{\langle\dot{g},\dot{g}\rangle} \right) = E' \end{aligned} \qquad (4.2.14)$$

E' represents the minimum of $E(a_0, a)$, which results from Eq.4.2.12. In general, the coupling between the noise and signals shown in Eq.4.2.12 may be excluded from the consideration. Accordingly, the inequality

$$E(\, a_\circ , a \,) \;>\; E' \tag{4.2.15}$$

is always satisfied. From Eq.4.2.9 and Eq.4.2.14, we can express the condition to satisfy Eq.4.2.11 in the form

$$\overset{\circ}{f}{}^2\left(\langle \overset{\circ}{g},\overset{\circ}{g}\rangle - \frac{\langle \overset{\circ}{g},\overset{\bullet}{g}\rangle^2}{\langle \overset{\bullet}{g},\overset{\bullet}{g}\rangle}\right) - 2\left(\langle N,N\rangle - \frac{\langle \overset{\bullet}{g},N\rangle^2}{\langle \overset{\bullet}{g},\overset{\bullet}{g}\rangle}\right) < 0 \tag{4.2.16}$$

Neglect the term of $\langle \overset{\bullet}{g},N\rangle^2/\langle \overset{\bullet}{g},\overset{\bullet}{g}\rangle$ (this is positive value), and rewrite Eq.4.2.16 as

$$\overset{\circ}{f}{}^2\left(\, \langle \overset{\circ}{g},\overset{\circ}{g}\rangle - \frac{\langle \overset{\circ}{g},\overset{\bullet}{g}\rangle^2}{\langle \overset{\bullet}{g},\overset{\bullet}{g}\rangle}\,\right) < 2\langle N,N\rangle \tag{4.2.17}$$

It is obvious from the above procedure that the values of a which satisfy Eq.4.2.17 simultaneously establish Eq.4.2.16 and Eq.4.2.11 as well. Let

$$\sigma_g = \left\{ \frac{1}{J}\left(\langle \overset{\circ}{g},\overset{\circ}{g}\rangle - \frac{\langle \overset{\circ}{g},\overset{\bullet}{g}\rangle^2}{\langle \overset{\bullet}{g},\overset{\bullet}{g}\rangle} \right) \right\}^{\frac{1}{2}} \tag{4.2.18}$$

$$\sigma_N = \left\{ \frac{1}{J} \langle N,N\rangle \right\}^{\frac{1}{2}} \tag{4.2.19}$$

Eq.4.2.17 can be expressed in the form

$$\overset{\circ}{f}\sigma_g(a_\circ,a) < \sqrt{2}\,\sigma_N \tag{4.2.20}$$

$\sigma_g(a_\circ,a)$ can be regarded as an indicator how the function $g=g(a,r)$ changes its overall shape (g_j, $j=1-J$) in terms of the changes of a. $\sigma_g(a_\circ,a)$ represents the degree of similarity between the figures of $\overset{\circ}{g}=g(a_\circ,r_j)$ and $\overset{\bullet}{g}=g(a\;,r_j)$, $j=1-J$. For example, let $J=2$, and

$$\overset{\bullet}{g}_1 = g(a\;,r_1) \qquad \overset{\circ}{g}_1 = g(a+\Delta a,r_1) \qquad \Delta g_1 = \overset{\circ}{g}_1 - \overset{\bullet}{g}_1$$

$$\overset{\bullet}{g}_2 = g(a\;,r_2) \qquad \overset{\circ}{g}_2 = g(a+\Delta a,r_2) \qquad \Delta g_2 = \overset{\circ}{g}_2 - \overset{\bullet}{g}_2$$

Then σ_g is given as

$$2\sigma_g = \frac{\dot{g}_1 \Delta g_2 - \dot{g}_2 \Delta g_1}{\dot{g}_1^2 + \dot{g}_2^2}$$

Consider the two figures shown in Fig.4.2.2. It is clear that the two polygons, ABCD and EFGH, are similar figures. Indeed, substitution of the values indicated in Fig.4.2.2 yields $\sigma_g = 0$. If J=1, the "shape" of g is just a line, and regardless of the variation of a, the shapes of g are always similar figures. Hence $\sigma_g = 0$. Eq.4.2.18 will be expressed in the form

$$J\sigma_g^2 = \langle \mathring{g}, \mathring{g} \rangle \left\{ 1 - \frac{\langle \mathring{g}, \dot{g} \rangle^2}{\langle \mathring{g}, \mathring{g} \rangle \langle \dot{g}, \dot{g} \rangle} \right\}$$

The second term in the brace is related to the cross-correlation between the two data arrays, $\mathring{g}$ and $\dot{g}$. Accordingly σ_g can be also considered as a sort of correlation function of g in terms of the dual variables, a and r.

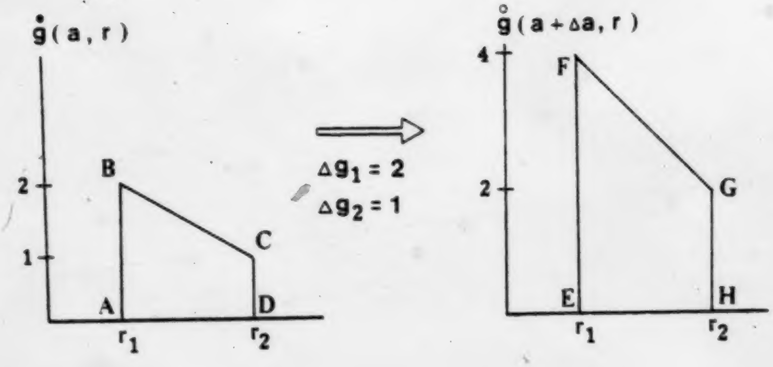

Fig.4.2.2 ..... Two polygons with "similar" shape.

4.3 The Resolution Related to the Model Functions g

I will evaluate σ_g using the model function g for the surface deformation fields due to the horizontal penny-shaped fracture, and examine whether or not the function g has the sufficient characteristics to satisfy the condition expressed by Eq.4.2.20 under a given noise level. It is noted that the theoretical estimate of the resolution should be made with respect to $\sqrt{2}\sigma_N$, whereas the resolution (error estimate) for the analysis of actual observed data should be evaluated against σ_N . .

Eq.4.2.20 indicates that large a variability of σ_g with changes of a is preferable in order to determine the radius of fracture accurately. $\sigma_g(a_o,a)$ depends on the fracture parameters, a and d, and the geometry of measuring points, r_j , j=1 ~ J. We need to understand how the function σ_g depends on these parameters. We are free to design the site configuration of measuring points, if the situation permits. It is natural to choose such a configuration of measuring points that yields as high a resolution as possible in the determination of fracture parameters.

The analytical evaluation of σ_g is difficult. In order to obtain $\sigma_g(a_o,a,J)$, the model field of $g(a,r_j)$, j=1 ~ J, was generated by the following specification.

$f = 1.0 \qquad d = 1.0$ (km)

$a_o = d/5$, $2d/5$, $3d/5$, $4d/5$, d

$a = d/20, 2d/20, 3d/20, , , , d \quad (\Delta a = d/20)$

$J = 10 , 20 , 30 , 40 , , , 100$

The interval of measuring points $(\Delta r) = d/50$

and $r_1 = 0.0$ (4.3.1)

In the following, the variables a_0 and a of the function σ_g (a_0, a, J) appear in the form

$$\sigma_g(\, a_0 \,, a_0 + \ell \Delta a, J \,)$$

$$a_0 = a/d \;,\; \Delta a = d/20 \;,\; \ell = 0, \pm 1, \pm 2, \cdots$$

The function σ_g for each of the uplift, the tilt, the horizontal displacement and the strain is identified by σ_U , σ_T , σ_R and σ_S .

Since the calculation of σ_g is based on the model data generated by f=1.0 and d=1.0 km, comparisons of σ_g for arbitrary values of f and d with noise level,(Eq.4.2.20), are made by

$$\begin{aligned} f \cdot d \cdot \sigma_U &< \sqrt{2}\, \sigma_{N,U} \\ f \cdot d \cdot \sigma_R &< \sqrt{2}\, \sigma_{N,R} \\ f \cdot \sigma_T &< \sqrt{2}\, \sigma_{N,T} \\ f \cdot \sigma_S &< \sqrt{2}\, \sigma_{N,S} \end{aligned} \qquad (4.3.2)$$

where $\sigma_{N,g}$ (g=U,T,R,S) denotes the noise level for the respective deformation field.

Fig.4.3.1 shows $\sigma_T(a_0=0.4, a, J=50)$. This figure illustrates general features of most σ_g with fixed values of a and J. The following features can be seen.

(1) σ_g behaves almost linearly with respect to $\pm \ell \Delta a$, especially in the region of $\ell > 0$ and small values of $-\ell$.

$$\sigma_g \propto \pm \ell \Delta a$$

(2) In general, σ_g has steeper slope for $\ell > 0$ than that for

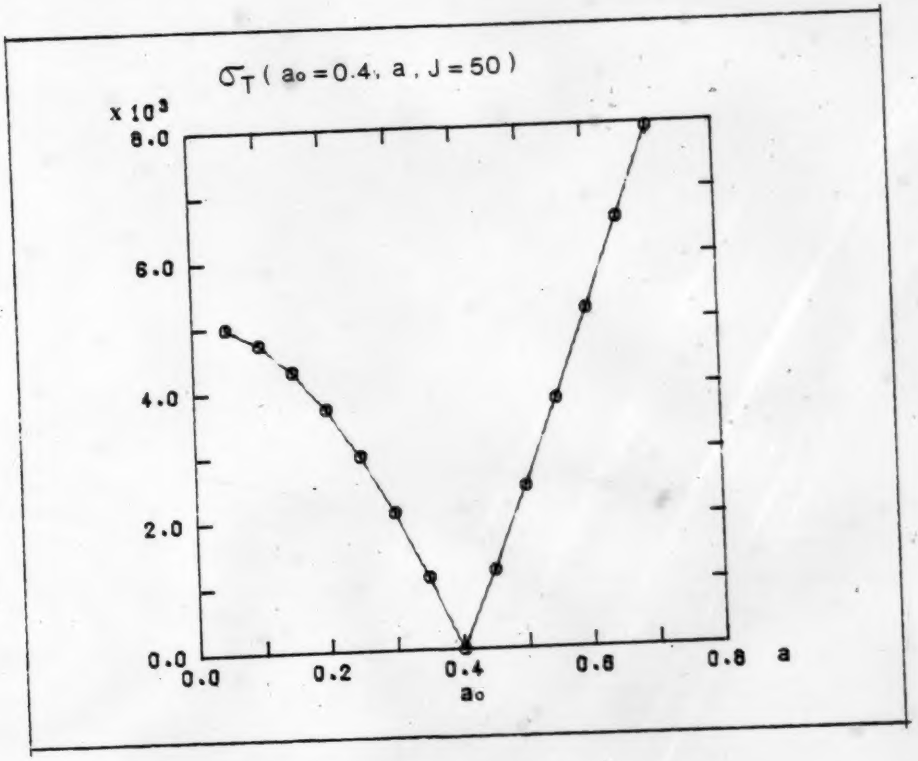

Fig.4.3.1 .....$\sigma_T(a_o,a,J)$

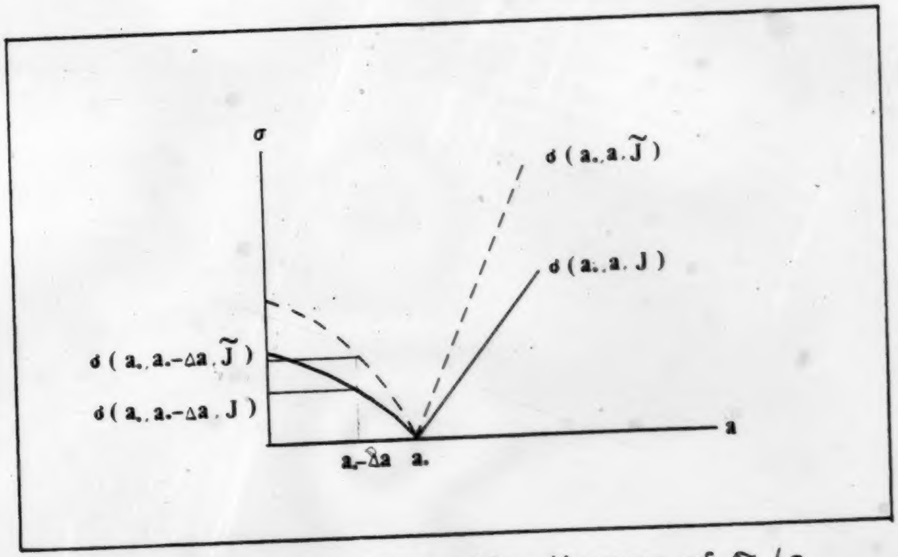
σ
σ (a₀, a, J̃)
σ (a₀, a, J)
σ (a₀, a₀−Δa, J̃)
σ (a₀, a₀−Δa, J)
a
a₀−δa
a₀

Fig.4.3.2 ..... Schematic diagram of $\sigma_g(a_o,a,J)$ showing its dependence on the number of measurement points, J.

0, i.e.,

$$\sigma_g(a_o, a_o - \ell\Delta a, J) < \sigma_g(a_o, a_o + \ell\Delta a, J)$$

This suggests higher resolution of the upper limit of "a" than that of the lower limit.

Fig.4.3.2 illustrates the dependence of σ_g on J (number of measurement points). σ_g has the steepest slope for a particular number of J, ($=\tilde{J}$). The following relations are found.

$$\tilde{J} = \begin{cases} 50 \sim 70 & \text{for } \sigma_U \\ 50 \sim 80 & \text{for } \sigma_T \\ 60 \sim 90 & \text{for } \sigma_R \\ 30 \sim 50 & \text{for } \sigma_S \end{cases} \qquad (4.3.3)$$

where a/d = 0.2 ~ 1.0. Since the parameter J corresponds to span length of measuring points, the above relations can be replaced by the relations between the length of the span, $\tilde{L}$, and the depth of fracture, d.

$$\tilde{L} = \tilde{J} \times \Delta\tau = \tilde{J} \times \frac{d}{50} = \begin{cases} (\ 1.0 \sim 1.4\ )d & \text{for } \sigma_U \\ (\ 1.0 \sim 1.6\ )d & \text{for } \sigma_T \\ (\ 1.2 \sim 1.8\ )d & \text{for } \sigma_R \\ (\ 0.6 \sim 1.0\ )d & \text{for } \sigma_S \end{cases} \qquad (4.3.4)$$

As shown by Eq.4.2.20, the larger value of σ_g is more desirable in order to obtain high resolution. Therefore $\tilde{L}$ will be referred to as the "optimum measuring span". It is obvious from the nature of this inversion method that a longer span of measuring points does not always yield higher resolution in the determination of the fracture parameters. The magnitude of the surface deformations all decrease toward zero at large distances from the center of fracture, and the overall shape of the surface deformation field becomes more "similar".

The above relations, Eq.4.3.3 or Eq.4.3.4, are illustrated by Figs.4.3.3a-d. These figures also indicate that $\sigma_g(a_0,a_0-\Delta a,J)$ of larger a_0 changes its value more drastically than that of smaller a_0 with changes of J. This feature is significant for σ_T and σ_R.

The ratio of $\sigma_g(a_0,a_0-\Delta a,\widehat{J})$ / $\sigma_g(a_0,a_0-\Delta a,J=10)$ is tabulated in Table 4.3.1. Suppose the tilt responses associated with a fracture at depth 500m and of radius a =100m ($a_0=0.2$), and the noise level such that the resolution of 1m (b_1 in Fig.4.3.4) for the fracture radius is attained by the optimum span of measuring points ($\tilde{L}=500$m). Then Table 4.3.1 (see *) indicates that, if the span length is J=10 (L=100m), the attainable resolution (b_2 in Fig.4.3.4) is as low as 20.9 m.

Next, comparisons between σ_U, σ_R, σ_T and σ_S are shown. The relation of Eq.3.1.12 has shown that the signal levels of uplift and tilt fields in terms of maximum amplitude are related by the factor (1.0±0.2)d in the ratio of uplift/tilt. On the contrary, the analysis of resolution factors results in the relations

$$\frac{d\,\sigma_U(a_0,a_0-\Delta a,J=10)}{\sigma_T(a_0,a_0-\Delta a,J=10)} = 2.00\ (a_0=0.2) \sim 4.98\ (a_0=1.0) \tag{4.3.5a}$$

Fig.4.3.3 ..... The curve of $\sigma_g(a_o, a_o - \Delta a, J)$ as a function of J.

a .... $\sigma_u(a_o, a_o - \Delta a, J)$
b .... $\sigma_R(a_o, a_o - \Delta a, J)$
c .... $\sigma_T(a_o, a_o - \Delta a, J)$
d .... $\sigma_3(a_o, a_o - \Delta a, J)$

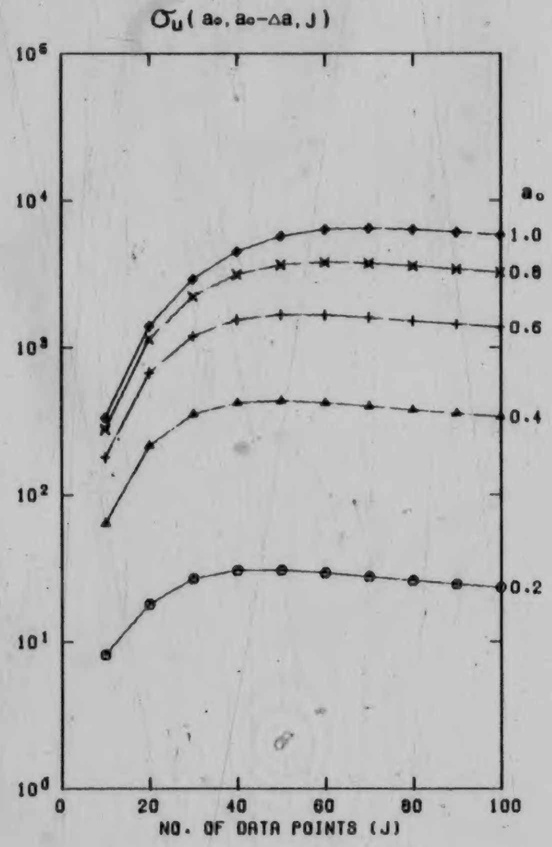

Fig.4.3.3a

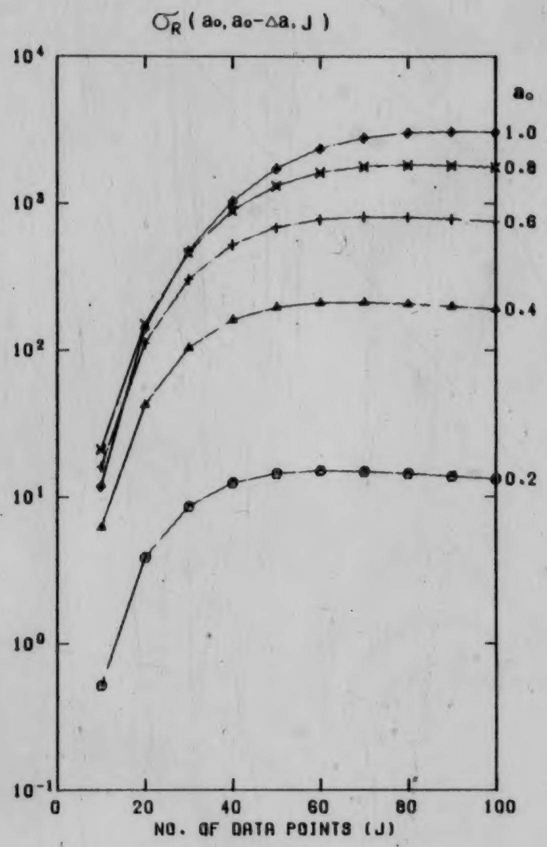

Fig.4.3.3b

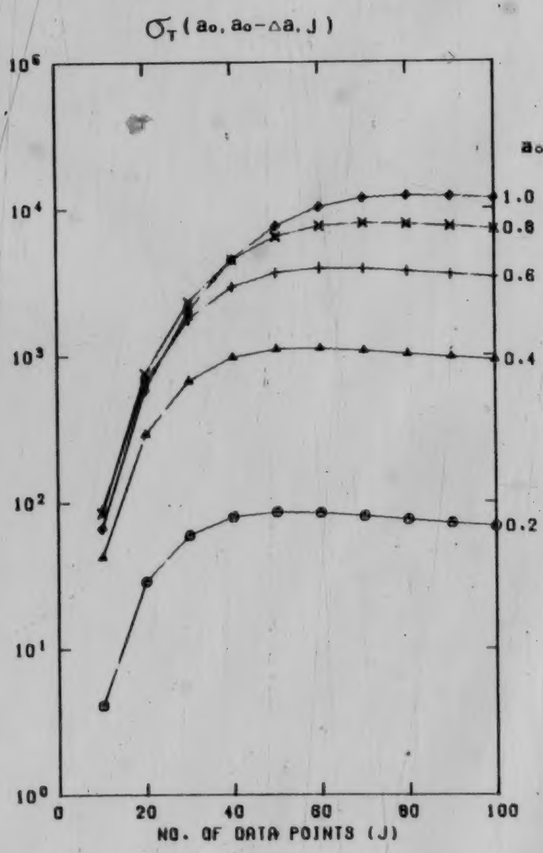

Fig.4.3.3c

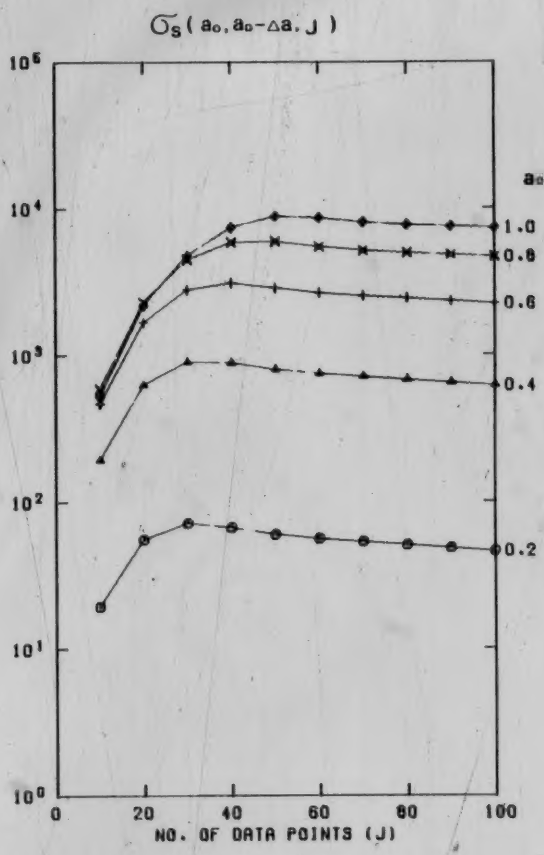

Fig.4.3.3d

a_0	σ_U	σ_T	σ_R	σ_S
0.2	3.77	20.9*	29.0	3.67
0.4	6.80	26.6	33.9	4.64
0.6	9.36	43.7	50.7	6.67
0.8	13.7	95.0	86.2	10.1
1.0	19.5	185.	259.	16.7

Table 4.3.1 .....$\sigma_g(a_0, a_0-\Delta a, \widetilde{J})/\sigma_g(a_0, a_0-\Delta a, J=10)$

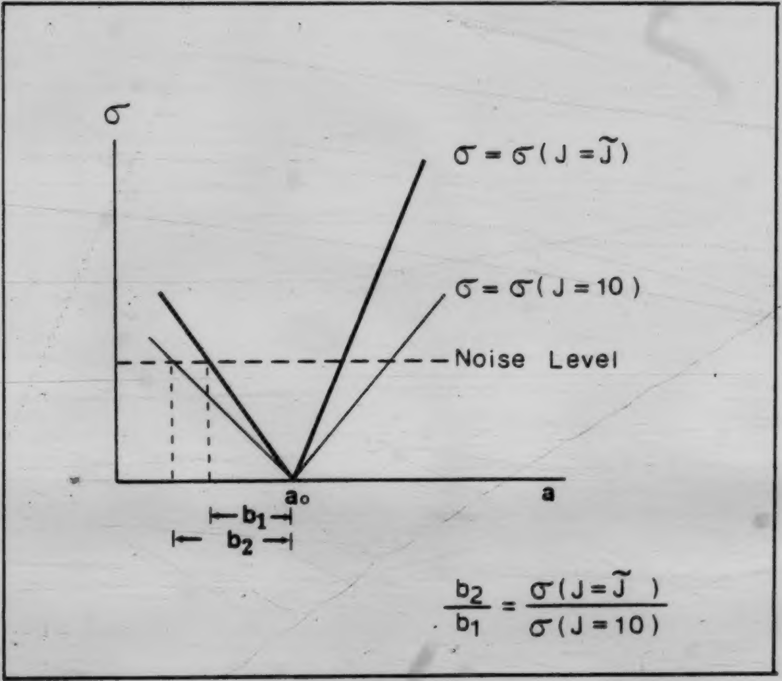
σ
$\sigma = \sigma(J = \widetilde{J})$
$\sigma = \sigma(J = 10)$
Noise Level
a_0
a
b_1
b_2
$\frac{b_2}{b_1} = \frac{\sigma(J=\widetilde{J})}{\sigma(J=10)}$

Fig.4.3.4 ..... Difference of resolution factors b resulting from changes of J.

$$\frac{d\,\sigma_U(a_0,a_0-\Delta a,J=\widetilde{J})}{\sigma_T(a_0,a_0-\Delta a,J=\widetilde{J})} = 0.36\ (a_0=0.2)\sim 0.52\ (a_0=1.0) \qquad \textbf{(4.3.5b)}$$

where d has units of km, and the ratios have units of mm/microradian.

Assume that the noise level of the uplift data in millimeters is comparable to that of the tilt data in microradians. Eq.4.3.5b suggests that, if measuring points are arranged to the optimum span, the analysis of the tilt responses can yield a more unambiguous solution than that of the uplift data, as long as the depth of fracture is shallower than 2 km - 3 km and the ratio of radius/depth is less than 1.0. On the other hand, Eq.4.3.5a suggests that, if measuring points are limited to a narrow area above the center of fracture, the uplift data can be more useful than the tilt data for the analysis of fractures at depths deeper than 250 m - 500 m.

The ratios of σ_S / σ_T show the relations

$$\begin{aligned}\frac{\sigma_S(a_0,a_0-\Delta a,J=10)}{\sigma_T(a_0,a_0-\Delta a,J=10)} &= 4.75\ (a_0=0.2)\sim 7.94\ (a_0=1.0)\\ \frac{\sigma_S(a_0,a_0-\Delta a,J=\widetilde{J})}{\sigma_T(a_0,a_0-\Delta a,J=\widetilde{J})} &= 0.84\ (a_0=0.2)\sim 0.71\ (a_0=1.0)\end{aligned} \qquad \textbf{(4.3.6)}$$

where the units are microradian/microstrain. The ratios of σ_U / σ_R show the relations

$$\begin{aligned}\frac{\sigma_U(a_0,a_0-\Delta a,J=10)}{\sigma_R(a_0,a_0-\Delta a,J=10)} &= 15.8\ (a_0=0.2)\sim 28.2\ (a_0=1.0)\\ \frac{\sigma_U(a_0,a_0-\Delta a,J=\widetilde{J})}{\sigma_R(a_0,a_0-\Delta a,J=\widetilde{J})} &= 2.05\ (a_0=0.2)\sim 2.12\ (a_0=1.0)\end{aligned} \qquad \textbf{(4.3.7)}$$

where the units are mm/mm. The above relations all show different feature from the relations of Eq.3.1.10-Eq.3.1.12.

Several examples of quantitative details of σ_g are shown in Figs.4.3.5a-5h. Table 4.3.2 particularly tabulates $\sigma_g (a_0=0.4, a_0-\Delta a, J)$. Assume we have surface deformation fields due to a fracture of radius 160m, amplitude factor 10^{-3} and at depth 400m. Table 4.3.3 gives the upper limit of the noise level which will allow determination of the radius of fracture within the certainty of ±20m from the measurements ($\Delta r = d/50 = 8m$). The values in this table are calculated by using Table 4.3.2 and Eq.4.3.2.

So far, the resolution functions σ_q have been evaluated by setting a configuration of measurement points, which should be discussed as a variable of σ_q. Here supposing the five types of measurement configuration shown in Fig.4.3.6, I examine which configuration yields the maximum resolution for each of the deformation fields of uplift, horizontal displacement and tilt. The results are summarized in Table 4.3.4. The optimum configuration, which yields the highest resolution, is shown in the column of "Best". Assuming that a resolution 20 percent lower than the highest resolution is the minimum acceptable measure, the corresponding reasonable configuration is shown in the column of "20 percent allowance".

The comparison of the resolution factors attained by the respective optimum configuration for the three

Fig.4.3.5 ..... The curve of $\sigma_g(a_0, a, J)$ as a function of a.

a .... $\sigma_U(a_0=0.2, a, J)$
b .... $\sigma_U(a_0=0.4, a, J)$
c .... $\sigma_R(a_0=0.2, a, J)$
d .... $\sigma_R(a_0=0.4, a, J)$
e .... $\sigma_T(a_0=0.2, a, J)$
f .... $\sigma_T(a_0=0.4, a, J)$
g .... $\sigma_S(a_0=0.2, a, J)$
h .... $\sigma_S(a_0=0.4, a, J)$

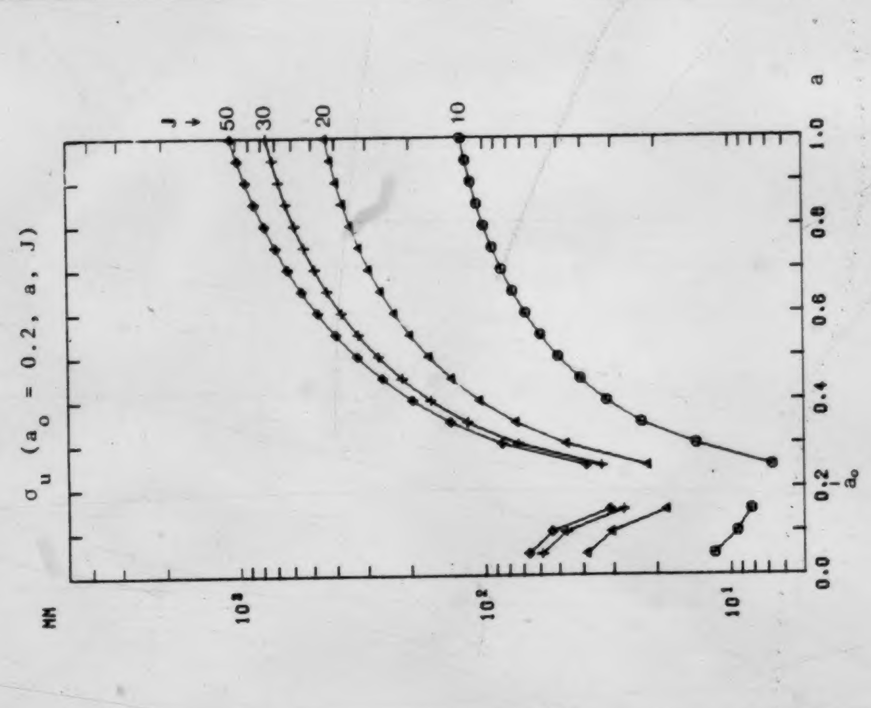

Fig.4.3.5a

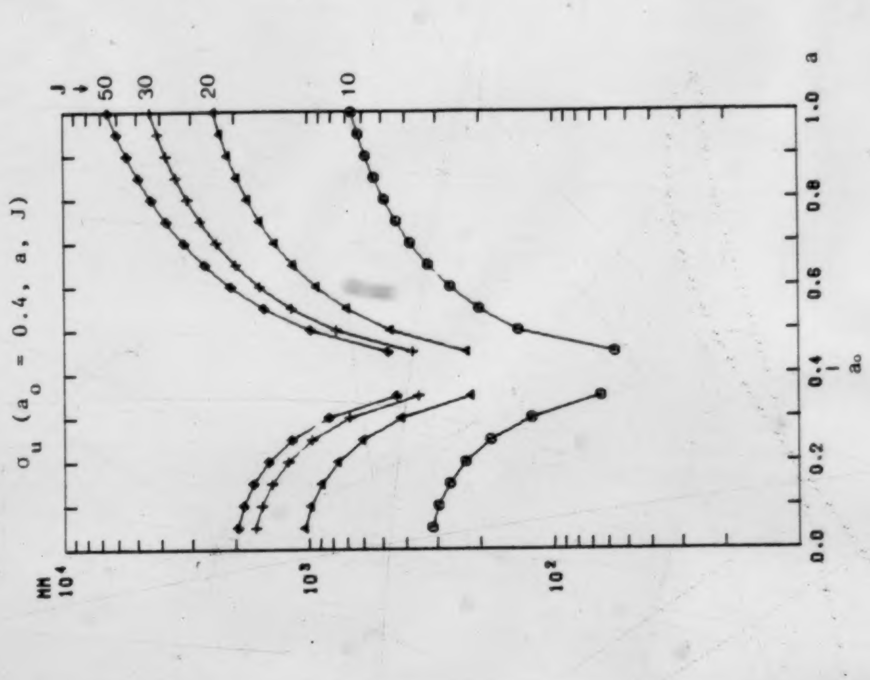

Fig.4.3.5b

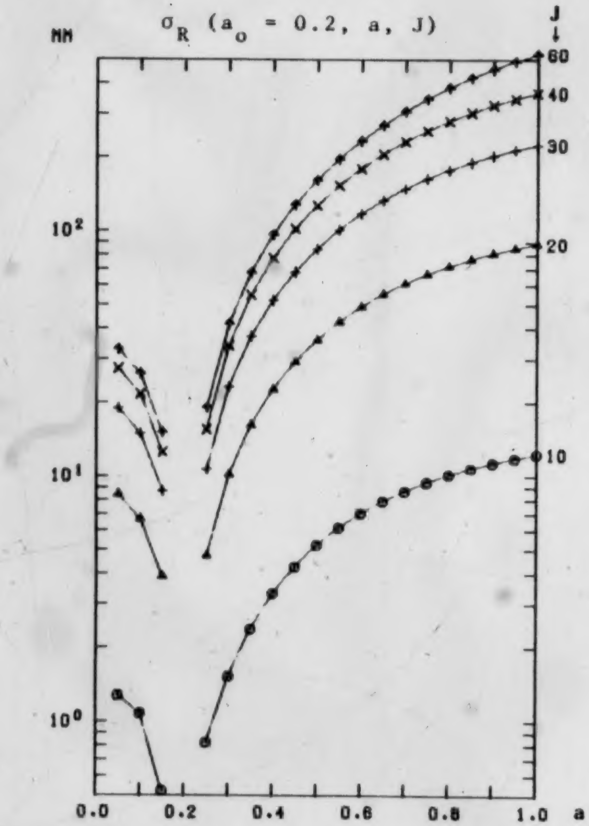

Fig.4.3.5c

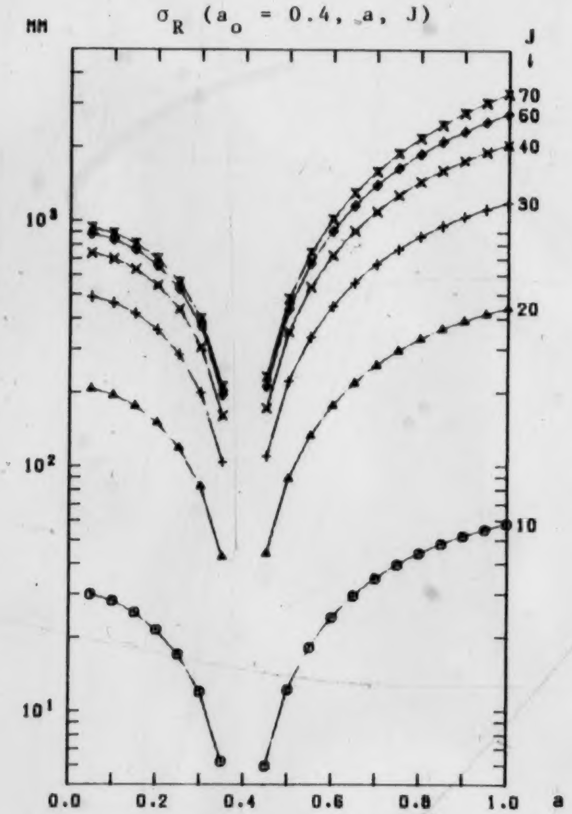

Fig.4.3.5d

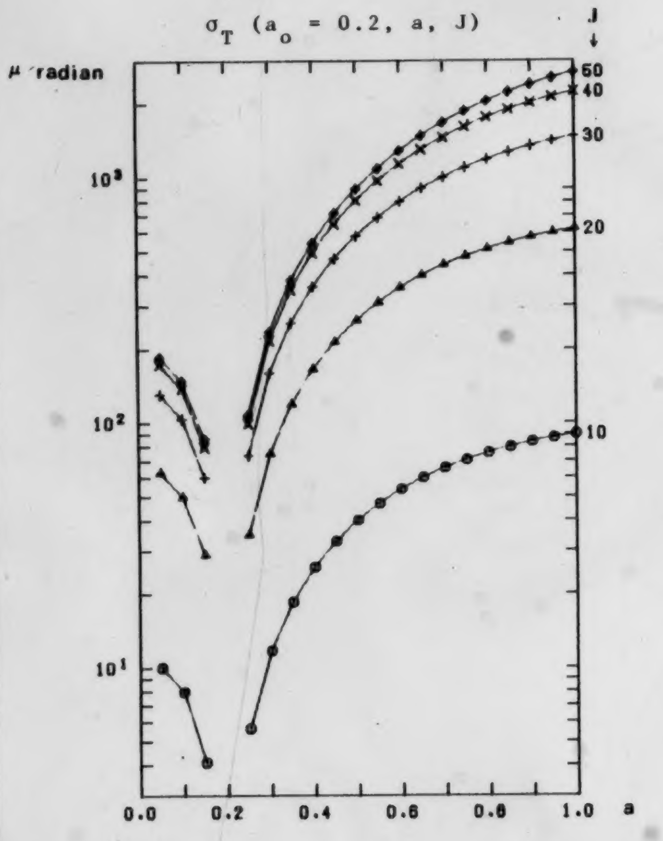

Fig.4.3.5e

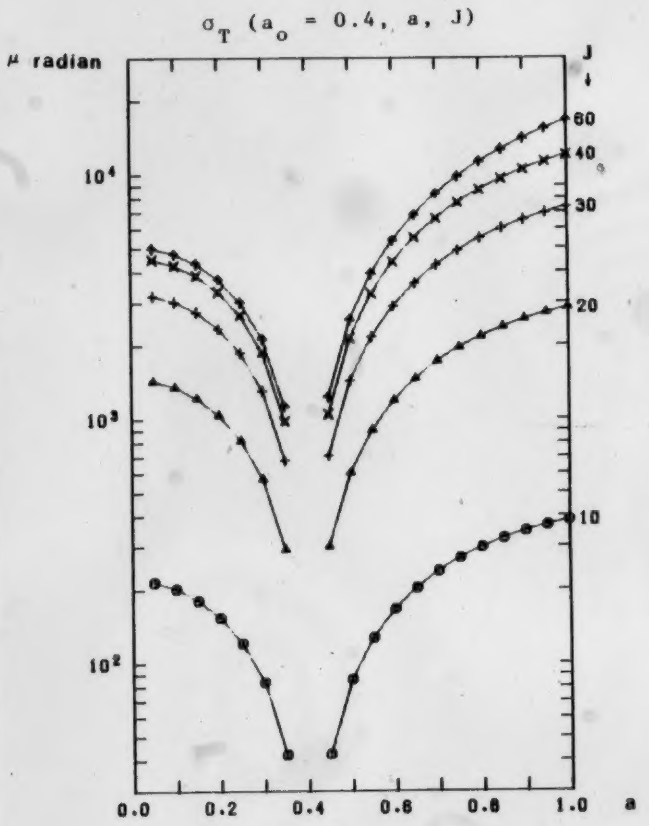

Fig.4.3.5f

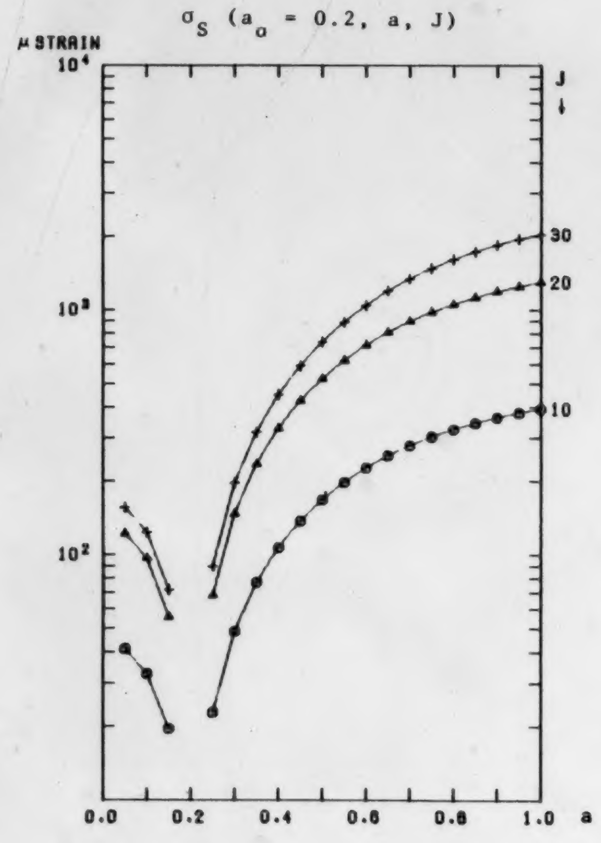

$\sigma_S\ (a_o = 0.2,\ a,\ J)$

Fig.4.3.5g

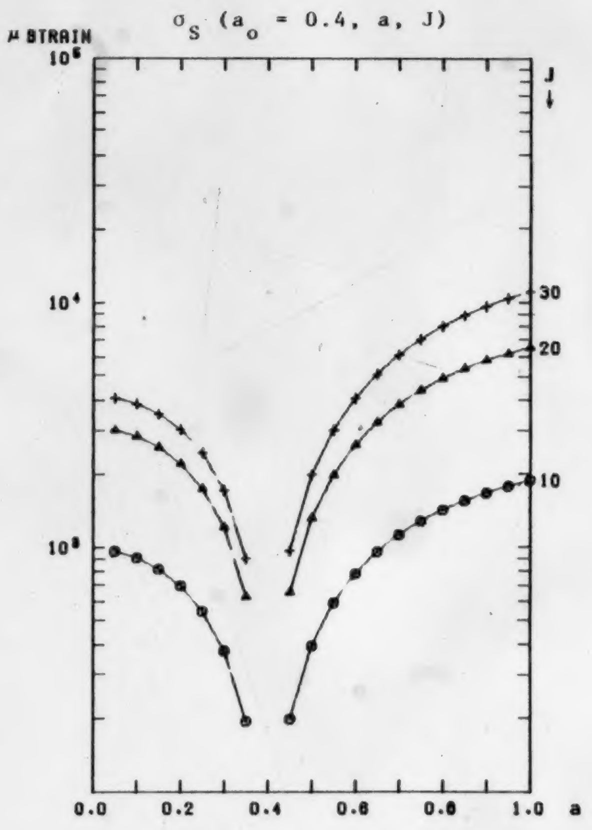

$\sigma_S\ (a_o = 0.4,\ a,\ J)$

Fig.4.3.5h

No.of Pts. J	Span Length L	Uplift (mm)	Hori. Disp. (mm)	Tilt (μrad.)	Hori. Strain (μstr.)
10	d/5	64.24	6.225	42.18	193.8
20	2d/5	216.4	42.54	292.0	627.3
30	3d/5	353.9	103.8	676.1	900.1
40	4d/5	423.5	160.7	978.1	888.0
50	d	436.7	195.7	1112.	798.9
60	6d/5	422.4	209.9	1124.	744.3
70	7d/5	400.0	211.2	1083.	709.6
80	8d/5	377.3	206.1	1029.	678.3
90	9d/5	356.9	198.6	975.3	647.6
100	2d	339.0	190.5	927.1	618.5

Table 4.3.2 .....$\sigma_g(a_0=0.4, a_0-\Delta a, J)$

	Uplift (mm)	Hori. Disp. (mm)	Tilt (μrad.)	Hori. Strain (μstrain)
J=10 (L=80m)	0.018	0.002	0.030	0.137
$J=\tilde{J}$ $(\tilde{L}=\ )$	0.124 (400m)	0.060 (560m)	0.795 (480m)	0.635 (240m)

Table 4.3.3 ..... Estimates of the upper limit of noise-level to attain a resolution of ±20 meters for the radius of fracture.

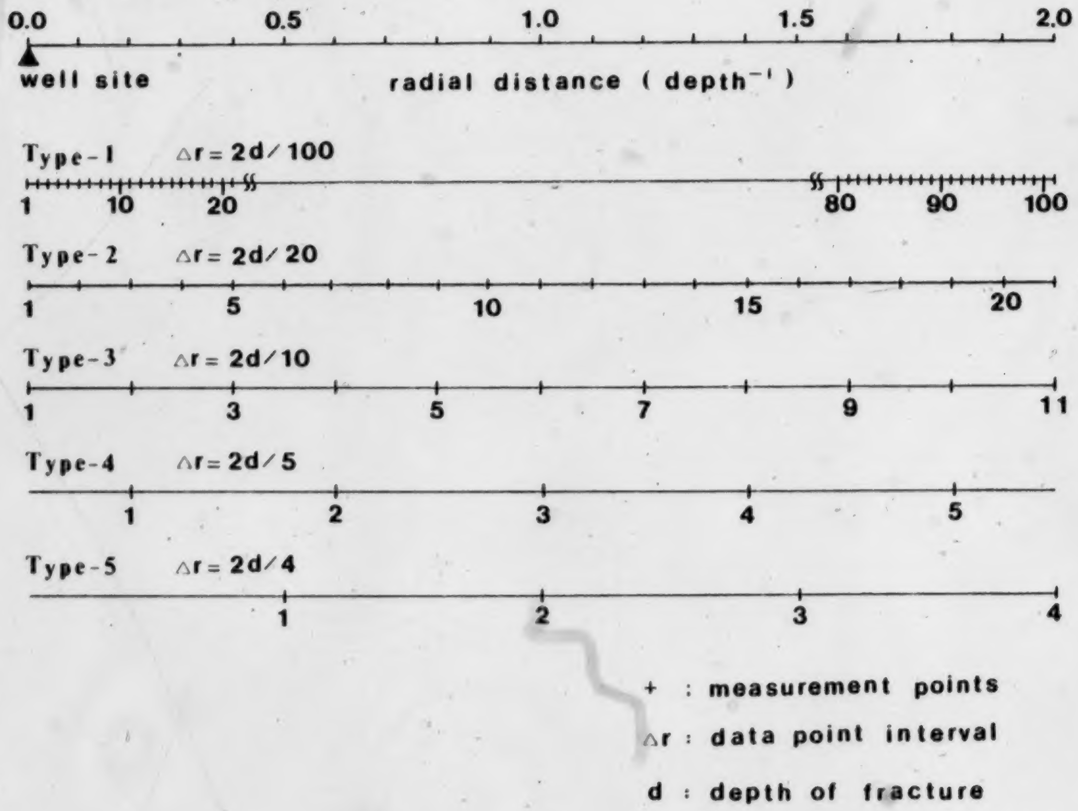
0.0
0.5
1.0
1.5
2.0
well site
radial distance (depth⁻¹)
Type-1 △r = 2d/100
1 10 20 80 90 100
Type-2 △r = 2d/20
1 5 10 15 20
Type-3 △r = 2d/10
1 3 5 7 9 11
Type-4 △r = 2d/5
1 2 3 4 5
Type-5 △r = 2d/4
1 2 3 4
+ : measurement points
△r : data point interval
d : depth of fracture

Fig.4.3.6 ..... Models of measurement point configuration.

	BEST	20% ALLOWANCE
Uplift	Type – 2 L = 0.8 ∼ 1.2 J = 9 ∼ 13	Type – 4 L = 0.6 ∼ 1.0 J = 2 ∼ 3
Tilt	Type – 1 L = 1.0 ∼ 1.6 J = 51 ∼ 81	Type – 3 L = 0.8 ∼ 1.0 J = 5 ∼ 6
Horizontal Displacement	a/d ≤ 0.6 Type – 4 L = 0.6 ∼ 1.0 J = 2 ∼ 3	a/d ≤ 0.4 same as the left
	0.8 ≤ a/d ≤ 1.0 Type – 5 L = 1.0 ∼ 1.5 J = 2 ∼ 3	0.6 ≤ a/d ≤ 1.0 same as the left

a : radius of fracture
d : depth of fracture
J : number of measurment points
L : span length of measurement points (depth^{-1})

Table 4.3.4 ..... The optimum and minimum acceptable measurement configurations.

deformation fields indicates

$$\frac{\sigma_R}{\sigma_T} \sim 1.0 \quad , \quad \frac{\sigma_u}{\sigma_T} \sim 0.5$$

for the fractures which $0.2 < a/d < 1.0$. This analysis also indicates that resolution factors for the tilt and horizontal displacement fields depend heavily on the type of measurement configuration, especially for the fractures of large a/d. This probably results from the fact that the location of the extrema for these fields shifts remarkably with changes of the radius.

In the analysis of observed surface deformation data, the amplitude factor f is obtained as a function of the variable a (see Eq.4.2.4), like the least-squares error E(a) (see Eq.4.2.5). If we can estimate the order of magnitude of the amplitude factor of actual fracture, we may expect that the behavior of f(a) can determine a possible range of the fracture radius. The behavior of f(a) may be evaluated by the calculation of

$$f = \mathring{f}\,\frac{\langle \mathring{g}, \dot{g} \rangle}{\langle \dot{g}, \dot{g} \rangle}$$

Similar to $\sigma_g(a_o,a,J)$, f will be expressed as $f_g(a_o,a,J)$.

Fig.4.3.7 shows $f_T(a_o,a,J=10)/\mathring{f}$. The values in this figure are calculated by using the model tilt field generated by the previous specification (Eq.4.3.1). The following features of $f_g/\mathring{f}$ are found.

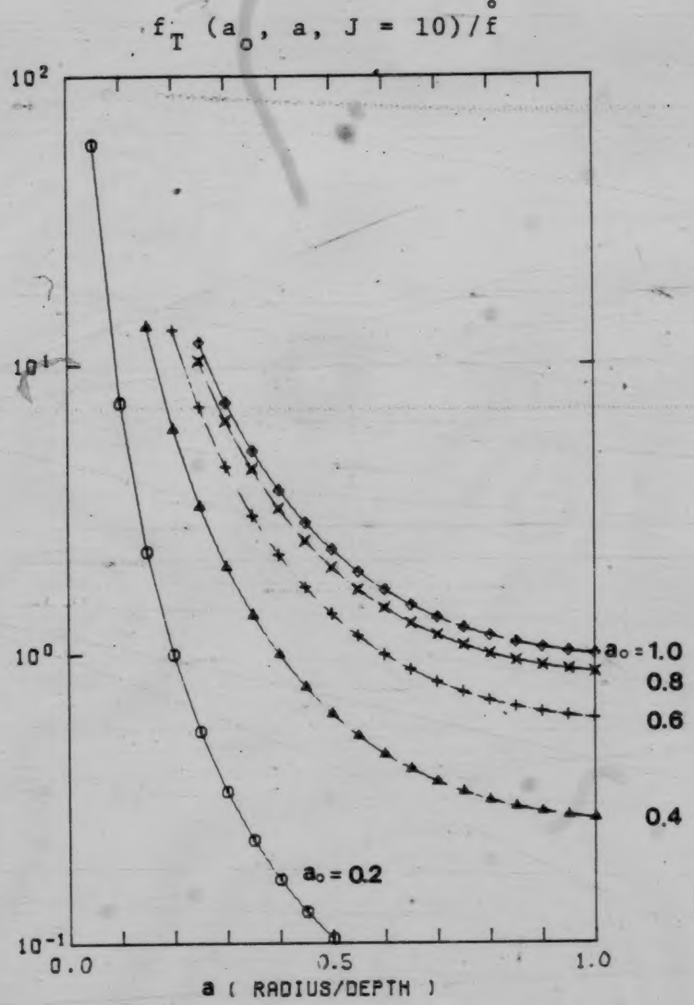

Fig.4.3.7 ..... The amplitude factor as a function of an unknown parameter a, normalized the true value of the amplitude facture, $\mathring{f}$.

(1) $f_g/\overset{\circ}{f}$ of smaller $a_\circ$ has steeper slope.

(2) In the region of $\ell < 0$ (under-estimate of a), it shows more distinct difference from the actual value of the amplitude factor.

(3) The behavior of $f_g/\overset{\circ}{f}$ does not depend on the kind of data (g=U,T,R,S) and the number of data points (J=10 ~ j=100) and all show an almost same curve as Fig.4.3.7.

(1) and (2) suggest that, if the order of magnitude of the actual amplitude factor can be estimated, the resulting values of f(a) determine the lower limit of possible values of the fracture radius, especially for fractures of small radius compared with the depth of fracture. It is noted that the dependency of $f_g/\overset{\circ}{f}$ on $a_\circ$ and $\pm \ell \Delta a$ shows the opposite feature to that of σ_g.

4.4 S/N Enhancement by Combination of Two Kinds of Data

There are several measurable quantities, such as uplift, tilt, radial displacement and strain, relating to a fracture. When some combination of these measurable quantities is considered as input data for the inversion problem, we may expect some enhancement of the signal to noise ratio. Here I will consider the simplest case in which two kinds of observed data, P' and Q', are combined in the form

$$Z'_j = P'_j + xQ'_j \qquad (4.4.1)$$

where j denotes the j'th measuring point, and x is introduced as a variable parameter (it will be called the "stacking factor") and assumed to be independent with respect to j. Incorporating the combination of Eq.4.4.1 and the inversion scheme described in the previous section, I will obtain an equation for the determination of a specific value of x which will yield higher resolution than that achieved by the observed data P' or Q' alone.

Consider a fracture of radius a_o and amplitude factor $\overset{o}{f}$, and express the observed values of data P and Q at the j'th measuring point of distance r_j in the form

$$\begin{aligned} P'_j &= \overset{o}{f}\, p(a_o, r_j) = \overset{o}{f}\, \overset{o}{p}_j + \overset{(p)}{N}_j \\ Q'_j &= \overset{o}{f}\, q(a_o, r_j) = \overset{o}{f}\, \overset{o}{q}_j + \overset{(q)}{N}_j \end{aligned} \qquad (4.4.2)$$

where p and q are the model fuctions for the deformation fields due to the fracture, respectively relating to data P and Q, and $\overset{(p)}{N}$ and $\overset{(q)}{N}$ are noise components of data P and Q, respectively. Define a function

$$z = p + xq$$

and let

$$\overset{\circ}{z}_j = \overset{\circ}{p}_j + x\overset{\circ}{q}_j \tag{4.4.3}$$

In the same way as in the previous section, the following notations are used.

$$\overset{\bullet}{p}_j = p(a,r_j) \tag{4.4.4}$$

$$\overset{\bullet}{q}_j = q(a,r_j) \tag{4.4.5}$$

$$\overset{\bullet}{z}_j = z(a,r_j) \tag{4.4.6}$$

$$\langle A,B \rangle = \sum_j (A_j B_j) \tag{4.4.7}$$

Denote σ defined by Eq.4.2.18 for the functions p,q and z by σ_p, σ_q and σ_z. Also denote σ for the noise components by $\sigma_{n,p}$, $\sigma_{n,q}$ and $\sigma_{n,z}$, respectively. These σ are given by

$$J\sigma_p^2 = \langle\overset{\circ}{p},\overset{\circ}{p}\rangle-\langle\overset{\circ}{p},\overset{\bullet}{p}\rangle^2/\langle\overset{\bullet}{p},\overset{\bullet}{p}\rangle \tag{4.4.8}$$

$$J\sigma_q^2 = \langle\overset{\circ}{q},\overset{\circ}{q}\rangle-\langle\overset{\circ}{q},\overset{\bullet}{q}\rangle^2/\langle\overset{\bullet}{q},\overset{\bullet}{q}\rangle \tag{4.4.9}$$

$$J\sigma_z^2 = \langle\overset{\circ}{z},\overset{\circ}{z}\rangle-\langle\overset{\circ}{z},\overset{\bullet}{z}\rangle^2/\langle\overset{\bullet}{z},\overset{\bullet}{z}\rangle \tag{4.4.10}$$

$$J\sigma_{n,p} = \langle\overset{(p)}{N},\overset{(p)}{N}\rangle \tag{4.4.11}$$

$$J\sigma_{n,q} = \langle\overset{(q)}{N},\overset{(q)}{N}\rangle \tag{4.4.12}$$

$$J\sigma_{n,z} = \langle\overset{(p)}{N},\overset{(p)}{N}\rangle+2x\langle\overset{(p)}{N},\overset{(q)}{N}\rangle+x^2\langle\overset{(q)}{N},\overset{(q)}{N}\rangle \tag{4.4.13}$$

In the following, it is assumed that

$$\langle\overset{(p)}{N},\overset{(q)}{N}\rangle = 0 \tag{4.4.14}$$

Substitution of Eq.4.4.3 and Eq.4.4.6 into Eq.4.4.10 yields the expression of σ_z in terms of p and q,

$$J\sigma_z^2 = \frac{A_0+A_1x+A_2x^2+A_3x^3+A_4x^4}{B_0+B_1x+B_2x^2} \tag{4.4.15}$$

where

$$\begin{aligned}
A_0 &= \langle \mathring{p},\mathring{p}\rangle\langle \dot{p},\dot{p}\rangle-\langle \mathring{p},\dot{p}\rangle^2 \\
A_1 &= 2(\ \langle \mathring{p},\mathring{q}\rangle\langle \dot{p},\dot{p}\rangle+\langle \dot{p},\dot{q}\rangle\langle \mathring{p},\mathring{p}\rangle \\
&\qquad -\langle \mathring{p},\dot{p}\rangle\langle \mathring{p},\dot{q}\rangle-\langle \mathring{p},\dot{p}\rangle\langle \dot{p},\mathring{q}\rangle\ ) \\
A_2 &= \langle \mathring{p},\mathring{p}\rangle\langle \dot{q},\dot{q}\rangle+2\langle \mathring{p},\mathring{q}\rangle\langle \dot{p},\dot{q}\rangle+\langle \mathring{q},\mathring{q}\rangle\langle \dot{p},\dot{p}\rangle \\
&\quad -\langle \mathring{p},\dot{q}\rangle^2-\langle \dot{p},\mathring{q}\rangle^2-2\langle \mathring{p},\dot{q}\rangle\langle \dot{p},\mathring{q}\rangle-2\langle \mathring{p},\dot{p}\rangle\langle \mathring{q},\dot{q}\rangle \\
A_3 &= \langle \mathring{p},\mathring{q}\rangle\langle \dot{q},\dot{q}\rangle+\langle \mathring{q},\mathring{q}\rangle\langle \dot{p},\dot{q}\rangle \\
&\quad -\langle \mathring{p},\dot{q}\rangle\langle \mathring{q},\dot{q}\rangle-\langle \dot{p},\mathring{q}\rangle\langle \mathring{q},\dot{q}\rangle \qquad (4.4.16) \\
A_4 &= \langle \mathring{q},\mathring{q}\rangle\langle \dot{q},\dot{q}\rangle-\langle \mathring{q},\dot{q}\rangle^2 \\
B_0 &= \langle \dot{p},\dot{p}\rangle \\
B_1 &= 2\langle \dot{p},\dot{q}\rangle \\
B_2 &= \langle \dot{q},\dot{q}\rangle
\end{aligned}$$

Let

$$(R)_p = \sigma_p/\sqrt{2}\sigma_{n,p} \qquad (4.4.17)$$

$$(R)_q = \sigma_q/\sqrt{2}\sigma_{n,q} \qquad (4.4.18)$$

$$(R)_z = \sigma_z/\sqrt{2}\sigma_{n,z} \qquad (4.4.19)$$

Substitution of Eq.4.4.13 and Eq.4.4.15 into Eq.4.4.19 yields

$$(R)_z = \left\{ \frac{1}{J}\ \frac{(A_0+A_1x+A_2x^2+A_3x^3+A_4x^4}{(D_0+D_2x^2)(B_0+B_1x+B_2x^2)} \right\}^{\frac{1}{2}} \qquad (4.4.20)$$

where

$$D_0 = 2\sigma_{n,p}^{\ 2}\ ,\ D_2 = 2\sigma_{n,q}^{\ 2} \qquad (4.4.21)$$

(R)z expresses the resolution resulting from the combination z=p+xq. (R)z maybe behaves such that it has the maximum value at a specific value of x, which is the most desired "stacking factor" for the enhancement of resolution because larger values of $(R)_z$ correspond to higher resolution. Eq.4.4.20 indicates that, if the information about the ratio $\sigma_{n,p}/\sigma_{n,q}$ is available, the desired value of x can be estimated by examining only the character of the functions p and q.

The degree of the resolution enhancement resulting from the combination can be evaluated by the ratio

$$(R)_p/(R)_z \quad \text{or} \quad (R)_q/(R)_z$$

The ratio is understood as follows. Fig.4.4.1 illustrates the resolutions relating to the function p alone, q alone and the combined function z=p+xq. Here we assume the linearity of σ-curves, which has been described in Section 4.3. The resolution in the determination of a (radius of fracture) can be expressed by a range between two intersections of σ-curve and σ_n-level. The resolution factor b shown in Fig.4.4.1 is given by

$$b_{\pm} = \Delta a \frac{\sqrt{2}\,\sigma_n}{f\,\sigma(a_0,a)} \quad , \quad a = a_0 \pm \Delta a \qquad (4.4.22)$$

Denote b for p, q and z by b_p, b_q and b_z. The ratio b_z/b_p is written in the form

$$\frac{b_z}{b_p} = \frac{\sigma_{n,z}}{\sigma_z} \Big/ \frac{\sigma_{n,p}}{\sigma_p} = \frac{(R)_p}{(R)_z} \qquad (4.4.23)$$

and expresses the degree of the enhancement of resolution.

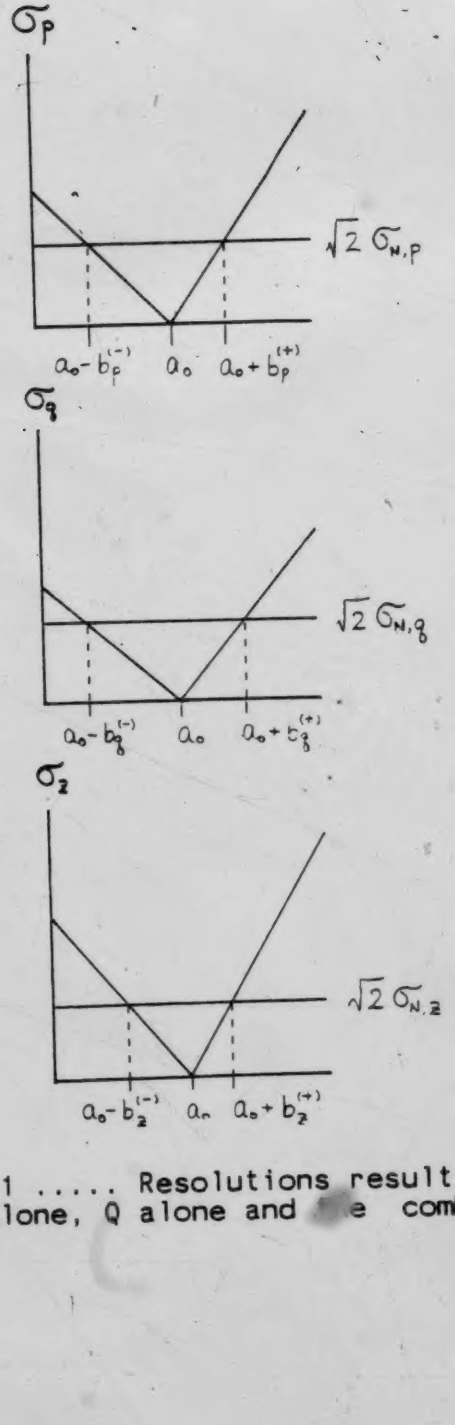
σ_p
$\sqrt{2}\,\sigma_{N,p}$
$a_0 - b_p^{(-)}$
a_0
$a_0 + b_p^{(+)}$
σ_q
$\sqrt{2}\,\sigma_{N,q}$
$a_0 - b_q^{(-)}$
a_0
$a_0 + b_q^{(+)}$
σ_z
$\sqrt{2}\,\sigma_{N,z}$
$a_0 - b_z^{(-)}$
a_0
$a_0 + b_z^{(+)}$

Fig.4.4.1 ..... Resolutions resulting from data P alone, Q alone and [illegible]e combination $Z=P+xQ$.

4.5 Determination of Time Varying Fracture Parameters

Denote the radius and amplitude factor of a fracture at time t_1 by a_1 and f_1,

$$a_1 = a(t_1) \quad , \quad f_1 = f(t_1) \tag{4.5.1}$$

and let $G_{1,j}$ and $g_{1,j}$ be one of the observables at the j'th measurement point of distance r and the corresponding model function, respectively,

$$g_{1,j} = g(a_1, r_j) \quad , \quad G_{1,j} = f_1 g(a_1, r_j) \tag{4.5.2}$$

where, for simplicity, the depth of the fracture has been assumed to be a known parameter, and noise components are not considered. The least-squares method with sweep procedure for the non-linear parameter a (This procedure has been described in Section 4.2, and will be denoted by LSM*) gives the relation, for the data set at time t_1,

$$f_1 = \frac{\langle g_1 , G_1 \rangle}{\langle g_1 , g_1 \rangle} \tag{4.5.3}$$

Similar to Eq.4.5.1, let

$$\begin{aligned} a_2 &= a(t_2) \quad , \quad g_{2,j} = g(a_2, r_j) \\ f_2 &= f(t_2) \quad , \quad G_{2,j} = f_2 g(a_2, r_j) \end{aligned} \tag{4.5.4}$$

The LSM* gives the relation, for the data set at time t_2,

$$f_2 = \frac{\langle g_2 , G_2 \rangle}{\langle g_2 , g_2 \rangle} \tag{4.5.5}$$

Then we can calculate the change of fracture parameters during the time= $t_1 \sim t_2$ as

$$\Delta f^* = f_2 - f_1 \tag{4.5.6}$$

$$\Delta a^* = a_2 - a_1 \tag{4.5.7}$$

If we have several sets of observed data at various times during the growth of the fracture, the fracture source parameters can be interpreted as time varying functions.

Next, one of the alternative methods for the calculation of Δa and Δf will be discussed. We have the equations

$$G_{t,j} = f_t \, g_{t,j}(a) \tag{4.5.8}$$

and

$$\Delta G_{t,j} = G_{t+\Delta t,j} - G_{t,j}$$

$$= \Delta f \left.\frac{\partial G}{\partial f}\right|_{t,j} + \Delta a \left.\frac{\partial G}{\partial a}\right|_{t,j} \tag{4.5.9}$$

$$= \Delta f \cdot g_{t,j} + \Delta a \cdot f_t \cdot \left.\frac{\partial g}{\partial a}\right|_{t,j} \tag{4.5.10}$$

If the appropriate initial value of f and a can be specified, and the observed data at more than two measuring points are available, Δa and Δf can be calculated by using Eq.4.5.10.

Define e and E by

$$\begin{aligned} e_j &= \Delta f \cdot g_{t,j} + \Delta a f_t \cdot \left.\frac{\partial g}{\partial a}\right|_{t,j} - \Delta G_{t,j} \\ E &= \langle e , e \rangle \end{aligned} \tag{4.5.11}$$

Apply the least-squares procedure to Eq.4.5.11

$$\frac{\partial E}{\partial \Delta a} = \frac{\partial E}{\partial \Delta f} = 0 \tag{4.5.12}$$

It follows that

$$\Delta f = \frac{\langle \Delta G , g \rangle \langle \frac{\partial g}{\partial a}, \frac{\partial g}{\partial a} \rangle - \langle g , \frac{\partial g}{\partial a} \rangle \langle \Delta G , \frac{\partial g}{\partial a} \rangle}{\langle g , g \rangle \langle \frac{\partial g}{\partial a}, \frac{\partial g}{\partial a} \rangle - \langle g , \frac{\partial g}{\partial a} \rangle^2} \tag{4.5.13}$$

$$\Delta a = \frac{\langle g,g\rangle\langle \Delta G,\frac{\partial g}{\partial a}\rangle - \langle \Delta G, g\rangle\langle g,\frac{\partial g}{\partial a}\rangle}{\langle g,g\rangle\langle \frac{\partial g}{\partial a},\frac{\partial g}{\partial a}\rangle - \langle g,\frac{\partial g}{\partial a}\rangle^2}\cdot\frac{1}{f} \qquad (4.5.14)$$

where numerous subscripts have been omitted. Although this procedure can be an alternative to the method described in Eq.4.5.3-Eq.4.5.7, it gives rise to several problems, which will be discussed in more detail.

A first remark is concerned with the initialization of a and f. Eq.4.5.13 and Eq.4.5.14 require the initial values such that $a \neq 0$ and $f \neq 0$. This is so because the calculation of "a" requires non-zero value of f as shown in Eq.4.5.14. It suggests that an additional tool (such as LSM*) should be prepared in order to determine the initial value of a and f. If the initial values are not specified correctly, the error which might accumulate should become serious. Usually the initial value can not be specified by a unique correct value but by some bounds. Therefore it is necessary to examine the results obtained by different possible initializations.

A second remark is concerned with computational effort. Suppose that we first calculate Δa, and obtain the result of $\Delta a = 0$. In this case, we can use the equation

$$\Delta f = \frac{\langle \Delta G, g\rangle}{\langle g, g\rangle} \qquad (4.5.15)$$

instead of Eq.4.5.13. Eq.4.5.15 is obtained by substituting $\Delta a = 0$ into Eq.4.5.10. Probably we would first compute only the numerator of Eq.4.5.14 for the calculation of Δa. When the result is $\Delta a = 0$, we do not need to compute the term $\langle \frac{\partial g}{\partial a}, \frac{\partial g}{\partial a} \rangle$ in the denominator, and we can simply determine Δf by Eq.4.5.15. This suggests significant reduction of computational effort. Similarly if we first calculate Δf and obtain the result $\Delta f = 0$, Δa can be calculated by the equation

$$\Delta a = \frac{\langle \Delta G , g \rangle}{\langle g , \frac{\partial g}{\partial a} \rangle} \cdot \frac{1}{f} \qquad (4.5.16)$$

A third comment is concerned with the inherent error contained in the solutions, Δa and Δf, obtained by Eq.4.5.13 and Eq.4.5.14. The true value of Δf is given by

$$\Delta f^{*} = f_2 - f_1 = \frac{\langle G_2 , g_2 \rangle}{\langle g_2 , g_2 \rangle} - \frac{\langle G_1 , g_1 \rangle}{\langle g_1 , g_1 \rangle} \qquad (4.5.17)$$

Suppose that each element in Eq.4.5.13 and Eq.4.5.14 is given by quantities in terms of time t_1 and t_2. Substitution

$$\Delta g = g_2 - g_1 , \quad G_2 = f_2 g_2 , \quad G_1 = f_1 g_1 \qquad (4.5.18)$$

into Eq.4.5.13 yields

$$\Delta f = f_2 - f_1 - \Delta\Delta f \qquad (4.5.19)$$

where

$$\Delta\Delta f = \frac{2 \langle g_1 , g_2 \rangle \langle g_1 , g_1 \rangle}{\langle g_1 , g_1 \rangle \langle g_2 , g_2 \rangle - \langle g_1 , g_2 \rangle^2} \qquad (4.5.20)$$

$\Delta\Delta f$ represents the error originating from Eq.4.5.13. Similarly we can imagine that Δa of Eq.4.5.14 also yields some difference from Δa^{*}. However, Δf in the case of Eq.4.5.15 yields the correct solution, because the basic equation, Eq.4.5.10, is a simple linear equation with respect to the parameter Δf only.

Here, let us consider the error source of $\Delta\Delta f$ and construct a procedure to reduce the error. The error comes from the treatment of Eq.4.5.10. The original equation of Eq.4.5.10 is

$$\begin{aligned} \Delta G &= G_2 - G_1 \\ &= \Delta f\, g_1 + f_1 \Delta g + \Delta f\, \Delta g \qquad (4.5.21) \end{aligned}$$

Eq.4.5.10 is an approximation of Eq.4.5.21 as the result of regarding

$$| \Delta f \Delta g | \ll | \Delta f\, g_1 + f_1 \Delta g | \qquad (4.5.22)$$

and discarding the higher terms of

$$\Delta g = \Delta a \frac{\partial g}{\partial a} + \frac{\Delta a^2}{2} \frac{\partial^2 g}{\partial a^2} + \cdots \qquad (4.5.23)$$

hence

$$\Delta g = \Delta a \frac{\partial g}{\partial a} \qquad (4.5.24)$$

In order to deal with Eq.4.5.21 as a linear equation, we adopt the approximations Eq.4.5.22 and Eq.4.5.24. Here, it is assumed that only the approximation Eq.4.5.24 is satisfied. Eq.4.5.21 can be rewritten into

$$\begin{aligned} \Delta G &= \Delta f\, (g_1 + \Delta g) + \Delta g\, f_1 \\ &= \Delta f \cdot g_2 + \Delta g\, f_1 \qquad (4.5.25') \\ &= \Delta f\, g_2 + \Delta a\, f_1 \left. \frac{\partial g}{\partial a} \right|_1 \qquad (4.5.25) \end{aligned}$$

Eq.4.5.25 suggests a way to reduce the inherent error for Δa and Δf. If g can be estimated in advance, it is better to solve Eq.4.5.25 than Eq.4.5.10.

Once we obtaine Δa and Δf by Eq.4.5.13 and Eq.4.5.14, we have the approximate values of g_2 and Δg

$$g_2' = g(a_1 + \Delta a) \quad \text{or} = g_1 + \Delta a \left.\frac{\partial g}{\partial a}\right|_1 \tag{4.5.26}$$

$$\Delta g' = g_2' - g_1 \tag{4.5.27}$$

Then Eq.4.5.25 can be expressed in the form

$$\Delta G = \Delta f\, g_2' + \Delta a\, f_1 \left.\frac{\partial g}{\partial a}\right|_1 \tag{4.5.28}$$

Applying the least-squares procedure to Eq.4.5.28, we can get the alternative solution for Δf and Δa by using the equations which are obtained by replacing g_2 with g_2' in Eq.4.5.13 and Eq.4.5.14. The iterative procedure - calculation of new g_2' and application of LSM - must tend to yield more accurate solutions. For example, the iterative

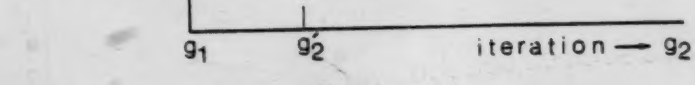

Fig.4.5.1 ..... Schematic diagram showing convergence of in iterative computations.

calculations for Δf are made by

$$\Delta f' = \frac{\langle \Delta G, g_2' \rangle \langle \frac{\partial g}{\partial a}, \frac{\partial g}{\partial a} \rangle - \langle g_2', \frac{\partial g}{\partial a} \rangle \langle \Delta G, \frac{\partial g}{\partial a} \rangle}{\langle g_2', g_2' \rangle \langle \frac{\partial g}{\partial a}, \frac{\partial g}{\partial a} \rangle - \langle g_2', \frac{\partial g}{\partial a} \rangle^2} \qquad (4.5.29)$$

The tendency of $g_2' \to g_2$ naturally results in $\Delta f' \to \Delta f^*$. Consequently, $\Delta f'$ might possibly behave as shown in Fig.4.5.1, where g is assumed to be a positive function.

Another iteration scheme is possible. In Eq.4.5.25', if g_2' and $\Delta g'$ are respectively substituted for g_2 and Δg, the unknown parameter is only Δf. Then the least-squares procedure can be applied with respect to Δf, and leads to the solution

$$\Delta f' = \frac{\langle \Delta G - \Delta g' f_1, g_2 \rangle}{\langle g_2', g_2' \rangle} \qquad (4.5.30)$$

On the other hand, the calculation of Δa is based on the equation

$$\Delta G = \Delta f' g_2' + \Delta a f_1 \left.\frac{\partial g}{\partial a}\right|_1 \qquad (4.5.31)$$

Δa is calculated by

$$\Delta a' = \frac{\langle \Delta G - \Delta f' g_2', \frac{\partial g}{\partial a} \rangle}{f_1 \langle \frac{\partial g}{\partial a}, \frac{\partial g}{\partial a} \rangle} \qquad (4.5.32)$$

Using $\Delta a'$ of Eq.4.5.32, calculate g_2' and $\Delta g'$, and repeat the computation of Eq.4.5.30 and Eq.4.5.32. The behavior of $\Delta f'$ with the iteration is given by

$$\Delta f' = f_2 \cdot \frac{\langle g_2 , g_2' \rangle}{\langle g_2' , g_2' \rangle} - f_1 . \qquad (4.5.33)$$

This derives from the substitution of

$$\Delta G = f_2 g_2 - f_1 g_1 \quad , \quad \Delta g_2' = g_2' - g_1 \qquad (4.5.34)$$

into Eq.4.5.30.

In order to take account of the higher terms in the Taylor's expansion of Δg , (Eq.4.5.23), following two methods are considered. One is based on the equation

$$A_j (\Delta a_j)^2 + 2B_j (\Delta a_j) + 2C_j = 0 \qquad (4.5.35)$$

where

$$A_j = f_1 \frac{\partial g}{\partial a}\Big|_{1,j}$$

$$B_j = f_1 \frac{\partial^2 g}{\partial a^2}\Big|_{1,j} \qquad (4.5.36)$$

$$C_j = \Delta f' g_{2,j}' - \Delta G_j$$

The above equations are the result of adding the second term of the Taylor's expansion to Eq.4.5.25. Since one available root of the above polynomial equation is

$$\Delta a_j' = \frac{-B_j + (B_j^2 - 2A_j C_j)^{1/2}}{A_j} \qquad (4.5.37)$$

The-least squares solution of $\Delta a_j'$ is given by

$$\Delta a = \frac{\langle \Delta a_j' , 1 \rangle}{\langle 1 , 1 \rangle} \qquad (4.5.38)$$

As long as the fracture behaves such that $\Delta a > 0$ and $B_j^2 - 2A_j C_j \geq 0$, Eq.4.5.38 can be used in place of Eq.4.5.32. There is, however, a possibility that $B_j^2 - 2A_j C_j < 0$ and/or $\Delta a < 0$ occur in practical computations, due to mis-estimates in earlier stages of the calculations as well as noise disturbance in observed data. when Eq.4.5.38 is used, the calculation of $g'_{2,j}$ in Eq.4.5.36 should not be made by $g'_{2,j} = g_{1,j} + \Delta a \frac{\partial g}{\partial a}\Big|_{1,j}$, but by $g'_{2,j} = g(a_1 + \Delta a, r_j)$, because Eq.4.5.35 has taken account of a higher term.

Another approach for the treatment of the higher terms of Δg is to apply appropriate non-linear inversion methods to the equation

$$\Delta G = \Delta f^{(1)} g'_2 + \Delta a f_1 \frac{\partial g}{\partial a} + \frac{(\Delta a)^2}{2} f_1 \frac{\partial^2 g}{\partial a^2} + \cdots \qquad (4.5.39)$$

instead of Eq.4.5.28 and/or Eq.4.5.31. However, the usage of any non-linear inversion method has no advantage unless it can reduce computational effort and yield fast convergence. Otherwise, f and a can be calculated by the method described in the first part of this section.

Suppose that two kinds of data are available. There is a different way to determine Δa and Δf. Two kinds of data will be distinguished by the notation of (1) and (2). We have the equation

$$\begin{aligned} \overset{(1)}{\Delta G}_j &= \Delta f \overset{(1)}{g}_j + \Delta a \frac{\partial \overset{(1)}{g}}{\partial a}\Big|_j \\ \overset{(2)}{\Delta G}_j &= \Delta f \overset{(2)}{g}_j + \Delta a \frac{\partial \overset{(2)}{g}}{\partial a}\Big|_j \end{aligned} \qquad (4.5.40)$$

The solution of this binary simultaneous equation is

$$\Delta f = \frac{A_j}{D_j} \quad , \quad \Delta a = \frac{B_j}{D_j} \qquad (4.5.41)$$

where

$$D_j = \overset{(1)}{g}_j \left.\frac{\partial \overset{(2)}{g}}{\partial a}\right|_j - \overset{(2)}{g}_j \left.\frac{\partial \overset{(1)}{g}}{\partial a}\right|_j$$

$$A_j = \Delta\overset{(1)}{G}_j \left.\frac{\partial \overset{(2)}{g}}{\partial a}\right|_j - \Delta\overset{(2)}{G}_j \left.\frac{\partial \overset{(1)}{g}}{\partial a}\right|_j \qquad (4.5.42)$$

$$B_j = \frac{1}{f}\left(\overset{(1)}{g}_j \Delta\overset{(2)}{G}_j - \overset{(2)}{g}_j \Delta\overset{(1)}{G}_j \right)$$

If appropriate intial values for f and a are specified, Δa and Δf can be determined by using the observed data at, at least, one measuring point. If the observed data at several measuring points are available, the least-squares solutions of Δa and Δf are given by

$$\Delta f = \frac{\langle D , A \rangle}{\langle D , D \rangle}$$

$$\Delta a = \frac{\langle D , B \rangle}{\langle D , D \rangle} \qquad (4.5.43)$$

The inherent error resulting from Eq.4.5.43 can be reduced in the same way as the iterative computations described previously.

4.6 Observation Equations for Geodetic Measurements

A horizontal penny-shaped fracture theoretically yields a displacement field with radial and vertical components. It is a reasonable choice to adopt a geodetic network such that measuring points are arranged radially from the well site.

Let (i) and (j) denote two measuring points located radially at distances r_i and r_j, respectively. Also let R_t and θ_t denote the slope distance and the vertical angle between these two points at time t from the inception of a fracture of radius a and amplitude factor f. The displacement vector at the point (i) during the time t will be denoted by $U_i = (U_i, W_i)$. The change of the displacement vector during the time interval $\Delta t = t_2 - t_1$ will be denoted by $\Delta U = (\Delta U_i, \Delta W_i)$.

First, suppose that we measure the slope distances, R, and the vertical angles, θ, at time t=1 and t=2.

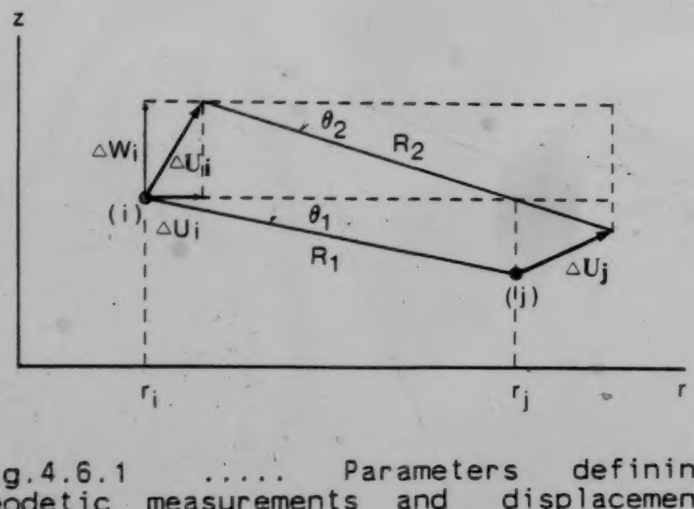

Fig.4.6.1 ..... Parameters defining geodetic measurements and displacement vectors at the points (i) and (j).

Referring to Fig.4.6.1, we have the relations.

$$R_2\cos\theta_2 - R_1\cos\theta_1 = \Delta\bar{U}_j - \Delta\bar{U}_i \qquad (4.6.1)$$

$$R_2\sin\theta_2 - R_1\sin\theta_1 = \Delta\bar{W}_i - \Delta\bar{W}_j \qquad (4.6.2)$$

If t=1 is substituted by the time of fracturing start, t=0, Eqs.4.6.1 and .2 are given in terms of the absolute displacements.

$$R_2\cos\theta_2 - R_0\cos\theta_0 = \bar{U}_j - \bar{U}_i \qquad (4.6.3)$$

$$R_2\sin\theta_2 - R_0\sin\theta_0 = \bar{W}_i - \bar{W}_j \qquad (4.6.4)$$

There is no radial displacement at the well site, r=0. Therefore,if the point (i) is supposed to be located at r=0, Eq.4.6.1 and Eq.4.6.3 are simplified into the form

$$R_2\cos\theta_2 - R_1\cos\theta_1 = \Delta\bar{U}_j \qquad (4.6.5)$$

$$R_2\cos\theta_2 - R_0\cos\theta_0 = \bar{U}_j \qquad (4.6.6)$$

When the measurements of R and θ are given in terms of the changes

$$\begin{aligned} R_2 &= R_1 + \Delta R \quad , \quad R_1 \gg |\Delta R| \\ \theta_2 &= \theta_1 + \Delta\theta \quad , \quad |\theta_1| \gg |\Delta\theta| \end{aligned} \qquad (4.6.7)$$

Eq.4.6.1 and Eq.4.6.2 are rewritten as

$$\Delta R\cos\theta_1 - \Delta\theta R_1\sin\theta_1 = \Delta\bar{U}_j - \Delta\bar{U}_i \qquad (4.6.8)$$

$$\Delta R\sin\theta_1 + \Delta\theta R_1\cos\theta_1 = \Delta\bar{W}_i - \Delta\bar{W}_j \qquad (4.6.9)$$

Let g and h be the model functions of the uplift and the radial displacement, respectively. We can express the displacements and its changes, Ui, Wi,ΔUi,ΔWi, in the form.

$$\begin{aligned} \bar{U}_i &= f_t\, h(a_t, r_i) \\ \bar{W}_i &= f_t\, g(a_t, r_j) \\ \Delta\bar{U}_i &= \Delta f \cdot h(a_t, r_i) + \Delta a \cdot f_t \left.\frac{\partial h}{\partial a}\right|_{t, r_i} \end{aligned} \qquad (4.6.10)$$

$$\Delta \bar{W}_i = \Delta f \cdot g(a_t, r_i) + \Delta a \cdot f_t \left.\frac{\partial g}{\partial a}\right|_{t, r_i}$$

Substitution of Eq.4.6.10 into Eqs.4.6.1 and 2, Eqs.4.6.3 and 4, or Eqs.4.6.8 and 9 yields the relations between the fracture parameters, (a,f) or (Δa,Δf) and the measurements, (R, θ) or (ΔR, Δθ).

Let

$$\begin{aligned} h_{ij,t} &= h(a_t, r_j) - h(a_t, r_i) \\ g_{ij,t} &= g(a_t, r_j) - g(a_t, r_i) \\ \dot{h}_{ij,t} &= \left.\frac{\partial h}{\partial a}\right|_{t, r_j} - \left.\frac{\partial h}{\partial a}\right|_{t, r_i} \\ \dot{g}_{ij,t} &= \left.\frac{\partial g}{\partial a}\right|_{t, r_j} - \left.\frac{\partial g}{\partial a}\right|_{t, r_i} \end{aligned} \qquad (4.6.11)$$

From Eqs.4.6.1 and 2, we have

$$R_2 \cos\theta_2 - R_1 \cos\theta_1 = \Delta f \cdot h_{ij,1} + \Delta a \cdot f_1 \dot{h}_{ij,1} \qquad (4.6.12)$$

$$R_2 \sin\theta_2 - R_1 \sin\theta_1 = -\Delta f\, g_{ij,1} - \Delta a \cdot f_1 \dot{g}_{ij,1} \qquad (4.6.13)$$

From Eqs.4.6.3 and 4, we have

$$R_2 \cos\theta_2 - R_0 \cos\theta_0 = f_2 \cdot h_{ij,2} \qquad (4.6.14)$$

$$R_2 \sin\theta_2 - R_0 \sin\theta_0 = -f_2 \cdot g_{ij,2} \qquad (4.6.15)$$

Next, suppose that we make measurement of the slope distance R alone. Denote the coordinates of two measurement points, (i) and (j), prior to the presence of the fracture by (r_i, z_i) and (r_j, z_j), respectively. Letting

$$\begin{aligned} r_{ij} &= r_j - r_i, \quad & z_{ij} &= z_j - z_i \\ \bar{U}_{ij} &= U_j - U_i, \quad & W_{ij} &= W_j - W_i \end{aligned} \qquad (4.6.16)$$

we have the relations

$$L_o = R_o^2 = r_{ij}^2 + z_{ij}^2 \qquad (4.6.17)$$

$$L_t = R_t^2 = (r_{ij} + \bar{U}_{ij})^2 + (z_{ij} + \bar{W}_{ij})^2 \qquad (4.6.18)$$

It can be considered practically that

$$\bar{U}_{ij}^2 , \bar{W}_{ij}^2 \ll |r_{ij} \bar{U}_{ij}| < r_{ij}^2$$

and should be, from the aspect of the theoretical model, that

$$z_{ij} \sim 0$$

It follows that,

$$L_t \sim L_o + 2 r_{ij} \bar{U}_{ij} \qquad (4.6.19)$$

Since the above equation does not involve the vertical component of the displacements and makes the problem trivial, the following is based on Eq.4.6.18 and the equation

$$\Delta L = \Delta f \frac{\partial L_t}{\partial f} + \Delta a \frac{\partial L_t}{\partial a}$$

Then we have an observation equation which relates the change of the slope distance ΔR and the changes of fracture parameters, Δa and Δf, in the form

$$R_t \cdot \Delta R = \Delta f (A_t h_{ij,t} + B_t g_{ij,t}) + \Delta a (A_t \dot{h}_{ij,t} + B_t \dot{g}_{ij,t}) f_t \qquad (4.6.20)$$

where

$$\begin{aligned} A_t &= r_{ij} + f_t h_{ij,t} \\ B_t &= z_{ij} + f_t \cdot g_{ij,t} \end{aligned} \qquad (4.6.21)$$

On the other hand, from Eq.4.6.19, we obtain the observation equation

$$R_t \cdot \Delta R = r_{ij} (\Delta f \cdot h_{ij,t} + \Delta a f_t \dot{h}_{ij,t}) \qquad (4.6.22)$$

5. Conclusions

The application of surface deformation measurement to the study of details of induced fracture requires an understanding of the accuracy with which surface deformation delineates changes of fracture source parameters. These include the shape, size, dip, strike of fracture as well as the pressure acting on the fracture surface and the displacement dislocation across the fracture plane. In order to analyse this problem, we need tractable and realistic fracture models and appropriate inversion methods. Once these tools are available, we can examine surface deformation data in terms of the attainable resolution for source parameters when noise of defined characteristics is superposed on the data.

Fractures result in several measurable quantities such as uplift tilt, horizontal displacement and strain. Some of these deformation fields are more sensitive to some of the source parameters than other fields. The sensitivities, which can be calculated from information in chapter 4, will indicate in particular cases the optimum observation strategy to be used. Particular locations will be sensitive to some of the source parameters and particular measurement configurations will be sensitive to others. For example a single line of tilt meters distributed in a radial direction with a spacing calculated from the results in chapter 4 would be indicated if equidimensional horizontal fractures are expected. The conventional strategy of a circular array does not exploit all possible information.

A horizontal penny shaped fracture model is not always adequate for a study of the form of fractures induced under various circumstances. It is necessary to extend the analysis to more general fracture models which have a dip or a shape which is not circular but which are still tractable. As long as a fracture plane can be assumed to be characterized by a uniform internal pressure or displacement dislocation, the surface deformation field can be expressed in the form

$$G_j = m \cdot g(\mathbf{n} , \mathbf{r}_j)$$

which consists of a linear parameter, m, depending on the internal pressure or the displacement dislocation, and several non-linear parameters, $\mathbf{n}$, depending on geometric source parameters. Even when a fracture does not have a plane structure or uniformity of the pressure or displacement dislocation, the surface deformation field can be expressed by superposition of the basic model equation, in the form

$$G_j = \sum_k m_k \cdot g_k(\mathbf{n}_k , \mathbf{r}_{k,j})$$

We can apply an inversion scheme and a method of resolution analysis like that described in the previous chapter, to these equations.

The detectability of small magnitude surface deformation is the minimum requirement to utilize such measurements. Accordingly we have to examine a survey design from the point of view of detectability. Often measuring points are located at places where the largest ground responses are predicted. We may expect that some of the source parameters can be estimated by finding the location yielding the maximum (more generally, the extrema or nodes) of the deformation field. We can not, however, discuss the applicability of the deformation measurement from such an aspect only. Indeed, a sensitivity analysis shows different results for these two cases. In one case, the maximum amplitude is compared, and in the other the resolution factor is compared.

Surprisingly, in the literature on hydraulic fracture, it is generally assumed that failure will occur by tensile fracture. In fact, many in-situ stress measurements have been inferred from hydrofracturing data based on the criterion for the occurrence of tensile fracture. There is, however, a possibility that fracture takes place as shear fracture or as combination of shear and tensile fractures. Basically we have to regard the failure mode as one of the unknown source properties. It must be considered that the measurement of surface deformation can be used for the determination of the failure mode if it is used properly, and that the possibility of such an analysis is one of the virtues of this geophysical method.

If we may assume a relatively simple geometry of an induced fracture, or if we may infer a rough geometry of a fracture in terms of strike and dip, it is mathematically possible to estimate the distribution of pressure or displacement dislocation on the fracture plane (or planes), by subdividing it (or them) into several grid cells each of which can be regarded to be characterized by uniform pressure or dislocation.

If the surface deformation is analysed in terms of the history of the source parameters, we could obtain significant results which delineate the process of fracture growth. We may then expect that these analyses could provide important information to substantiate or to revise theoretical predictions. Moreover, we expect that the surface deformation measurement reveals the in-situ behavior of hydraulic fracture which can not be investigated by laboratory experiments. For example, the determination of in-situ fracture toughness is one of the possible studies.

Measurements of the terrestrial deformation associated with volcanic activity and the occurence of earthquakes can also be treated by the techniques developed here. These studies differ from the investigation of a man-made subsurface deformation due to hydraulic fracturing only in scale. The areal extent, magnitude and time scale of hydraulic fracture are much smaller than those of earthquake and volcanic deformation.

Since hydraulic fracturing is conducted at relatively shallow depths. it is possible to obtain information about fracture parameters by direct measurements using observation wells. This implies that we can use more control data for the analysis of measured surface deformations. Results from the surface deformation analysis supported by such an advantage must play an important role not only in the field of energy resource development but also in geophysics itself.

6. Bibliography

Abou-Sayed, A. S., Brechtel, C. E. and Clifton, R. J., In situ stress determination by hydrofracturing: A fracture mechanics approach, **Journal of Geophysical Research**, Vol.83, No.B6, pp.2851-2862, 1978

Aki, K., Fehler, M. and Das, S., Source mechanism of volcanic tremor: Fluid-driven crack models and their application to the 1963 Kilauea eruption, **Journal of Volcanology and Geothermal Research**, Vol.2, pp.259-287, 1977

Aki, K. and Richards, P. G., **Quantitative Seismology: Theory and Methods**, W. H. Freeman and Company, 1980

Aktan, T. and Farouq Ali, S. M., Finite-element analysis of temperature and thermal stresses induced by hot water injection, **Journal of Society of Petroleum Engineers of AIME**, Vol.18, pp.457-469, 1978

Alewine, R. W. and Jordan, T. H., Generalized inversion of earthquake static displacement fields, **Geophysical Journal of the Royal Astronomical Society**, Vol.35, pp.357-361, 1973

Anderson, T. O. and Stahl, E. J., A study of induced fracturing using an instrumental approach, **Journal of Petroleum Technology**, Vol.19, No.2, pp.261-267, 1967

Ando, M., A fault-origin model of the great Kanto earthquake of 1923 as deduced from geodetic data, **Bulletin of the Earthquake Institute**, The University of Tokyo, Vol.49, pp.19-32, 1971

Asada, T. (Editor), **Jishin-Yochi no Hoho**, Tokyo Univ. Press, 1978 (in Japanese)

Backus, G. and Gilbert, F., Numerical applications of a formalism for geophysical inverse problems, **Geophysical Journal of the Royal Astronomical Society**, Vol.13, pp.247- , 1967

Backus, G. and Gilbert, F., The resolving power of gross Earth data, **Geophysical Journal of the Royal Astronomical Society**, Vol.16, pp.169- , 1968

Backus, G. and Gilbert, F., Uniqueness in the inversion of inaccurate gross Earth data, **Phil. Trans. Roy. Soc. London**, Series A, 226, pp.123- , 1970

Bartel, L. C., Seavey, R. W. and Northrop, D. A., Instrumentation for in situ coal gasification; III electrical techniques for remote monitoring, **In Situ**, Vol.2, No.4, pp.247-269, 1978

Barenblatt, G.I., The mathematical theory of equilibrium cracks in brittle fracture, in **Advances in Applied Mechanics**, edited by H. L. Dryden and Th. Von Karman, pp.55-129, Academic Press, New York, 1962

Bechman, L. W., Garbin, H. D. and Northrop, D. A., Instrumentation for in situ coal gasification: seismic and acoustic techniques for remote monitoring, **In Situ**, Vol.3, No.1, pp.1-31, 1979

Bell, J. S. and Gough, D. I., Northeast-southwest compressive stress in Alberta: Evidence from oil wells, **Earth and Planetary Science Letters**, Vol.45, pp.475-482, 1979

Bell, M. L. and Nur, A., Strength changes due to reservoir-induced pore pressure and stresses and application to Lake Oroville, **Journal of Geophysical Research**, Vol.83, No.B9, pp.4469-4483, 1978

Ben-Menahem, A. S. and Singh, S. J. and Solomon, F., Static deformation of a spherical earth model by internal dislocations, **Bulletin of the Seismological Society of America**, Vol.59, pp.813-853, 1969

Ben-Menahem, A. S. and Singh, S. J. and Solomon, F., Deformation of homogeneous earth model by finite dislocations, **Reviews of Geophysics and Space Physics**, Vol.8, pp.591-632, 1970.

Beasley, R. R., Instrumentation and evaluation of the Tally Energy Systems,Inc. oil shale project, Part I:

Hydraulic fracture result, **Sandia National Laboratories**, New Mexico, Report No. SAND 78-1885, 1979

Beasley, R. R. and Boade, R. R., Instrumentation and Evaluation of the Tally Energy Systems,Inc. oil shale project, Part II: Explosive insertion, detonation and post-shot evaluation results, **Sandia National Laboratories**, Report No. SAND 78-1886, 1980

Broek, D., **Elementary engineering fracture mechanics**, Noordhoff International Publishing, Lyden, 1974

Brunner, F. K., On the analysis of geodetic networks for the determination of the incremental strain tensor, **Survey Review**, Vol.25, pp.56-57, 1979

Burridge, R. and Knopoff, L., Body force equivalents for seismic dislocations, **Bulletin of the Seismological Society of America**, Vol.54, No.6, pp.1875-1888, 1964

Byerlee, J. D., Frictional characteristics of granite under high confining pressure, **Journal of Geophysical Research**, Vol.72, pp.3639-3648, 1967

Byerlee, J. D., Friction of rocks, Proc. Conf. II, Experimental studies of rock friction with application to earthquake prediction, **U.S.G.S.**, pp.55-77, 1977

Canitez, N. and Toksoz, M. N., Static and dynamic study of earthquake source mechanism: San Fernando Earthquake, **Journal of Geophysical Research**, Vol.77, pp.2583-2594, 1972

Chinnery, M. A., The deformation of the ground around surface faults, **Bulletin of the Seismological Society of America**, Vol.51, No.3, pp.355-372, 1961

Clark, J. B., A hydraulic process for increasing the productivity of wells, **Transactions of the Americam Institute of Mining and Metallurgical**, Vol.186, pp.1-8, 1949

Coulter, R. G., Hydraulic fracturing: new developments. **Journal of Canadian Petroleum Technology**, Vol.15, No.4, pp.35-40, 1976

Daneshy, A. A., Hydraulic fracture propagation in layered formations. **Journal of Society of Petroleum Engineers, AIME**, Vol.18, No.1, pp.33-41, 1978

Daneshy, A. A., On the design of vertical hydraulic fractures, **Journal of Petroleum Technology, AIME**, Vol.225, pp.83-97, 1973

Daneshy, A. A., Experimental Investigation of hydraulic fracturing through perforations, **Journal of Petroleum Technology, AIME**, Vol.255, pp.1201-1296, 1973

Davis, P. M., Hastie, L. M. and Stacey, F. D., Stresses within an active volcano-with particular reference to Kilauea, **Tectonophysics**, Vol.22, pp.355-362, 1974

Davis, D. T., Lytle, R. J. and Laine, E. F., Use of high-frequency electromagnetic waves for mapping an insitu coal gasification burn front, **In Situ**, Vol.3, No.2, pp.95-120, 1979

Dean, W. R., Parsons, H. W. and Sneddon, I. N., A type of stress distribution on the surface of a semi-infinite elastic solid, **Proc. Cambridge Phil. Soc.**, Vol.40, No.1, pp.5-18, 1944

Dieterich, J. H. and Decker, R. W., Finite element modelling of surface deformation associated with volcanism, **Journal of Geophysical Research**, Vol.80, pp.4094-4102, 1975

Domenico, S. N., Elastic properties of unconsolidated porous sand reservoirs, **Geophysics**, Vol.42, No.7, pp.1339-1368, 1977

Dusseault, M. B., The Geotechnical Characteristics of Oil Sands, **Ph.D thesis, The University of Alberta**, 1977

Dusseault, M. B., Stress state and hydraulic fracturing in the Athabasca Oil Sands. **Canadian Journal of Petroleum Technology**, Vol.16, No.3, pp.19-27, 1977

Dusseault, M. B. and Simmons, J. V., Fracture orientation changes during injection, **Proceeding of the 33th Canadian Geotechnical Conference**, Calgary, Alberta, Sep., 1980

Dusseault, M. B., The behaviour of hydraulically induced fractures in oil sands, **Underground Rock Engineering**, The Canadian Inst. of Mining and Metallurgy ,special issue Vol.22, pp.36-41, 1980

Erdogan, F. and Aksogan, O., Bonded half planes containing an arbitrarily oriented crack, **International Journal of Solids Structures**, Vol.10, pp.569-585, 1974

Evans, K. F., Holzhauzen, G. R. and Wood, M. D., The mapping of nitrogen gas induced hydraulic fractures in Devonian shale by observation of the associated surface deformation, SPE/DOE 8933, presented at **the 1980 SPE/DOE Symposium on Unconventional Gas Recovery** held in Pittburgh, May 18-21, 1980.

Evans, K., The growth of shallow hydraulic fractures as viewed through the surface deformation field, presented at the workshop on **Hydraulic Fracturing Stress Measurements** organized by the U.S.G.S. Office of Earthquake Studies and U.S. National Committee for Rock Mechanics, Monterey, Calif., Dec., 1981

Fast, C. R., Holman, G. B. and Covlin, R. J., The application of massive hydraulic fracturing to the tight Muddy "J" Formation, Watternberg Field, Colorado. **Journal of Petroleum Tecnology, AIME**, Vol.29, pp.10-16, 1977

Fehler, M., Changes in P wave velocity during operation of a hot dry rock geothermal system, **Journal of Geophysical Research**, Vol.86, No.B4, pp.2925-2928, 1981

Fukuda, K., Ippan-naibu-yugamikaku niyoru semi-infinite elastic body no henkei nitsuite, **Kenshin-jiho**, Vol.13, pp.263-291, 1944 (Japanese)

Geertsma, J., Survey of rock mechanics problems associated with the extraction of mineral fluids from underground formations, Proceedings of **The Third Congress of The International Society for Rock Mechanics**, Vol.1, Part

B, pp.1471-1481, 1974

Gough, D. I., Induced seismicity, Chapter 4 in **The Assesment of Minitigation of Earthquake Risk**, pub. UNESCO, pp.91-117, 1978

Green, A. E., On Boussinesq's problem and penny-shaped cracks, **Proc. Cambridge Phil. Soc.**, Vol.45, No.2, pp.251-257, 1949

Haimson, B. and Fairhurst, C., Initiation and extension of hydraulic fractures in rocks, **Society of Petroleum Engineers Journal**, Vol.7, pp.310-318, 1967

Haimson, B. and Fairhurst, C., Hydraulic fracturing in porous permeable materials, **Journal of Petroleum Tecnology**, Vol.21, pp.811-817, 1969

Haimson, B. C., Deep in-situ stress measurements by hydrofracturing, **Tectonophysics**, Vol.29, pp.41-47, 1975

Haimson, B., The hydrofracturing stress measuring method and recent field results. **International Journal of Rock Mechanics and Mining Society**, Vol.15, pp.167-178, 1978

Handin, J., Heard, H. C. and Magouirk, J. N., Effects of the intermediate principal stress on the failure of limestone, dolomite and glass at different temperatures and strain rates, **Journal of Geophysical Research**, Vol.72, pp.611-640, 1967

Harrison, E., Kieschnick, W. F. and McGuire, W. J., The Mechanics of fracture induction and extension, **Petroleum Transactions, AIME**, Vol.201, pp.252-263, 1954

Hastie, L. M. and Savage, . C., A dislocation model for the Alaska earthquake, **Bulletin of the Seismological Society of America**, Vol.60, pp.1389-1392, 1970

Holzhausen, G. R., Wood, M. D., Raisebeck, J. M. and Card, C. C., Results of deformation monitoring during steam stimulation in a single-well test, **Proceeding of Applied Oilsands Geoscience Conference**, Edmonton, Alberta, 1980

Howard, G. C. and Fast, C. R., Hydraulic fracturing, **Monograph Series of the Society of Petroleum Engineers, AIME**, Dallas, 1970

Hubbert, M. K. and Wills, D. G., Mechanics of hydraulic fracturing, **Petroleum Transactions, AIME**, Vol.210, pp.153-168, 1957

Huggett, G. R. and L. E. Slater, Precision of electromagnetic distance-measuring instrument for determining secular strain and fault movement, **Tectonophysics**, Vol.29, pp.19-27, 1975

Huggett, G. R., Slater, L. E. and Pavlis, G., Precision leveling with a two-fluid tiltmeter, **Geophysical Research Letters**, Vol.3, No.12, pp.754-756, 1976

Hungr, D. and Morgenstern, N. R., A numerical approach to predicting stresses and displacements around a three dimensional pressurized fracture, Department of Civil Engineering, The University of Alberta, April, 1980

Hussain, M. A., Pu, S. L. and Underwood, J., Strain energy release rate for a crack under combined Mode I and Mode II, **Americal Society for Testing and Materials Special Technical Publication**, 560, pp.2-28, 1973

Ito, H., DeVilbiss, J. and Nur, A., Compressional and shear waves in saturated rock during water-steam transition, **Journal of Geophysical Research**, Vol.84, No.B9, pp.4731-4735, 1979

Jackson, D. D., Interpretation of inaccurate, insufficient and inconsistent data, **Geophysical Journal of the Royal Astronomical Society**, Vol.28, pp.97-109, 1972

Jackson, D. D., Marginal solution to quasi-linear inverse problem in geophysics: the edgehog method, **Geophysical Journal of the Royal Astronomical Society**, Vol.35, pp.121-136, 1973

Jaeger, J. C. and Cook, N. G. W., **Fundamentals of Rock Mechanics**, Third edition, Chapman and Hall, London, 1979

Jenkins, G. R. and Kirkpatrick, J. W., Twenty years' operation of an in-situ combustion project, **Journal of Canadian Petroleum Technology**, Vol.18, No.1, pp.60-66, 1979

Jungles, P. H. and Frazier, G. A., Finite element analysis of the residual displacements for an earthquake rupture: Source parameters for the San Fernando Earthquake, **Geophysical Journal of Royal Astronomical Society**, Vol.78, pp.5062-5083, 1973

Kanamori, H. (Editor), **Chikyu Kagahu**, Vol.8, Jishin no Butusri, Iwanami Shoten, 1978 (in Japanese)

Kasahara, K. and Sugimura, A. (Editor), **Chikyu Kagaku** , Vol.10, Iwanami Shoten, 1978 (in Japanese)

Kassir, M. K. and Sih, G. C., **Three-dimensional crack problems**, Mechanics of Fracture, Vol.2, Noordhoff International Publishing, Leyden, The Netherlands, 1975

Koerner, R. M., McCabe, W. M., Huck, P. J. and Welsh, J. P., Hydrofracture monitoring using the acoustic emission method, **Proceedings of the Engineering Foundation Conferece on Geotechnical and Enviromental Aspects of Geopressure Energy**, Sea Island, GA, 1980

Kehle, R. O., The determination of tectonic stresses through analysis of hydraulic well fracturing, **Journal of Geophysical Research**, Vol.69, No.2, pp.259-273, 1964

Koide, H. and Bhattacharji, S., Formation of fractures around magmatic intrusions and their role in ore localization, **Economic Geology**, Vol.70, pp.781-799, 1975a

Lachenbruch, A. H., Depth and spacing of tension cracks, **Journal of Geophysical Research**, Vol.66, pp4273-4292, 1961

Landau, L. D. and Lifshitz, E. M., **Theory of Elasticity**, Vol.7 of Course of Theoretical Physics, translated from Russian by J. B. Sykes and W. E. Reid, Pergamon Press, Second Edition, 1970

Lardner, R. W., **Mathematical Theory of Dislocations and Fracture**, Vol.17 of Mathematical Expositions, University of Toronto Press, 1974

Lawn, B. R. and Wilshaw, T. R., **Fracture of Brittle Solids**, Cambridge University Press, 1975

Lawson, C. L. and R. J. Hanson, **Solving Least Squares Problems**, Prentice-Hall Inc., Englewood Cliffs, N.J., 1974

Locker, D. and Byerlee, J. D., Hydrofracture in Webber Sandstone at high confining pressure and differential stress. **Journal of Geophysical Research**, Vol.82, No.14, pp.2018-2026, 1977

Mansinha, L. and Smylie, D. E., Effect of earthquakes on the Chandler Wobble and the Secular polar shift, **Journal of Geophysical Research**, Vol. 72, No.18, pp.4731-4743, 1967

Mansinha, L. and Smylie, D. E., The displacement fields of inclined faults, **Bulletin of the Seismological Society of America**, Vol.61, No.5, pp.1433-1440, 1971

Margrave, G. F. and Nyland, E., Strain from repeated geodetic surveys by generalized inverse methods, **Canadian Journal of Earth Sciences**, Vol.17, No.8, pp.1020-1030, 1980

Margrave, G. F., Microgeodesy and South American Tectonics, **Ph.D Thesis, The University of Alberta**, 1980

Maruyama, T., On the force equivalents of dynamical elastic dislocations with reference to the earthquake mechanism, **Bulletin of the Earthquake Research Institute**, The University of Tokyo, Vol.41, pp.467-486, 1963

Maruyama, T., Statical elastic dislocations in an infinite and semi-infinite medium, **Bulletin of the Earthquake Research Institute**, The University of Tokyo, Vol.42, pp.289-368, 1964

Maruyama, T., On two-dimensional elastic dislocations in an infinite and semi-infinite medium, **Bulletin of the Earthquake Research Institute**, The University of Tokyo, Vol.44, pp.811-871, 1966

Matsuura, M. and Sato, R., Static deformation due to the fault spreading over several layers in a multi-layered medium, Part II: strain and tilt, **Journal of Physics of the Earth**, Vol.23, pp1-29, 1975

Matsuura, M., Inversion of geodetic data. Part I. Mathematical formulation, **Journal of Physics of the Earth**, Vol.25, pp.69-90, 1977a

Matsuura, M., Inversion of geodetic data. Part II. Optimal model of conjugate fault system for the 1927 Tango earthquake, **Journal of Physics of the Earth**, Vol.25, pp.233-255, 1977b

McClain, W. C., The mechanics of hydraulic fractures in shales, **The 3rd Symposium on Salt**, Vol.2, pp.410-420, The Northern Ohio Geological Society Inc., 1969

McCowan, D. W., Glover, P. and Alexander, S. S., A static and dynamic finite element analysis of the 1971 San Fernando, California, earthquake, **Geophysical Journal of Royal Astronomical Society**, Vol.48, pp.163-185,1977

M.D.Wood Inc., Analysis of ground tilts associated with hydraulic-fracture formation and explosive injection, Rock Spring, Wyoming, April-August, 1978: submitted to **Sandia National Laboratories**, Albuquerque, New Mexico, 1979

Melchior, P., **The Earth Tides**, Pergamon Press Inc., New York, 1976

Mikumo, T., Faulting process of the San Fernando Earthquake of February 9, 1971 inferred from static and dynamic near-field displacements, **Bulletin of the Seismological Society of America**, Vol.63, pp.249-269, 1973

Miyashita, K and Matsuura, M., Inversion analysis of static displacement data associated with the Alaska earthquake of 1964, **Journal of Physics of the Earth**, pp.333-349, 1978

Mogi, K., Fracture and flow of rocks under high triaxial compression, **Journal of Geophysical Research**, Vol.76, pp.1255-1269, 1971

Mogi, K., Ganseki-rikigaku to jishin, **Chikyu Kagaku**, Vol.8, pp.211-262, Iwanami Shoten, Tokyo, 1978 (Japanese).

Morgenstern, N., A relation between hydraulic fracture pressure and tectonic stresses. **Geofisica Pura E Applicate**, Vol.52, pp.104-114, 1962

Muskhelishvili, N. I., **Some Basic Problems of The Mathematical Theory of Elasticity**, The Second English Edition, Noordhoff International Publishing, Leyden, 1977

NRC (The National Research Council), **Geodetic Monitoring of Tectonic Deformation - Toward a Strategy**, National Academy Press, 1981

Nyland, E., Body force equivalents as sources of anelastic processes, **Canadian Journal of Earth Sciences**, Vol.8, No.10, pp.1184-1189, 1971

Nyland, E., Body-force equivalent calculations from permanent deformation in the near field, **Geophysical Journal of Royal Astronomical Society**, Vol.32, pp.279-294, 1973

Nyland, E., Body force equivalent calculations for subsidence of the Po Valley, **Pageoph**, Vol.114, pp.95-107, 1976

Nyland, E., Repeated geodetic surveys as experiments in geophysics, **Canadian Surveyor**, Vol.31, No.4, pp.347-360, 1977

Nyland, E. et al., Measurement and analysis of ground movement using microgeodetic networks on active faults, **Geofisica Internacional**, Vol.18, pp.53-71, 1979

Paris, P. and Sih, G. C., **Stress analysis of cracks**, Amarican Society for Testing and Materials Special Technical Publication, Vol.381, pp.30-81, 1964

Parker, R. L., Inverse theory with grossly inadequate data, **Geophysical Journal of the Royal Astronomical Society**, Vol.29, pp.123-138, 1972

Parker, R. L., Understanding inverse theory, **Annual Reviews of the Earth and Planetary Science**, Vol.5, pp.35-64, 1977

Parker, R. L., Linear inference and underparameterized models, **Reviews of Geophysics and Space Physics**, Vol.15, No.4, pp.446-456, 1977

Paulding, B. W. Jr., Orientation of hydraulically induced fractures. **9th Symposium on Rock Mechanics**, Colorado School of Mines, Colorado, pp.461-489, 1967

Pearson, C., The relationship between microseismicity and high pore pressures during hydraulic stimulation experiments in low permeability granitic rocks, **Journal of Geophysical Research**, Vol.86, No.B9, pp.7855-7864, 1981

Perkins, T. K. and Kern, L. R., Widths of hydraulic fractures, **Journal of Petroleum Technology**, AIME, Vol.13, pp.937-949, 1961

Pollard, D. D., Equations for stress and displacement fields around pressurized elliptical holes in elastic solids. (International Journal) **Mathematical Geology**, Vol.5, No.1, pp.11-25, 1973

Pollard, D. D. and Holzhausen, G., On the mechanical interaction between a fluid-filled fracture and the earth's surface, **Tectonophysics**, Vol.53, pp.27-57, 1979.

Pollard, D. D., On the form and stability of open hydraulic fractures in the earth's crust, **Geophysical Research Letters**, Vol.3, No.9, pp.513-516, 1976

Power, D. V., Schuster, C. L., Hay, R. and Twombly, J., Detection of hydraulic fracture orientation and dimensions in cased wells, **Transactions of the Society of Petroleum Engineers of AIME**, Vol.261, pp.1116-1124,1976

Power, D. V., Acoustic emissions following hydraulic fracturing in a gas well, **Proceedings of First Conference on Acoustic Emission and Microseismic Activity in Geologic Structures and Materials**, pp.291-308, Trans Tech Publications, 1977

Press, F., Displacements, strains, and tilts at teleseismic distances, **Journal of Geophysical Research**, Vol.70, No.10, pp.2395-2412, 1965

Raisbeck, J. M. and Currie, J. B., A laboratory investigation of hydraulic fracturing in oil sands, **In Situ**, Vol.5, No.1, pp.1-24, 1981

Raleigh, C. B., Hearly, J. H. and Bredehoeft, J. D., Faulting and crustal stress at Rangely, Colorado. in **Geophysical Monograph Series, No.16**, "Flow and Fracture of Rocks", pp.275-284, 1972

Rice, J. R., Mathematical analysis in the mechanics of fracture, in **Fracture: An Advanced Treatise**, edited by H. Liebowitz, Vol.II, pp.191-308, Academic Press, 1968

Rice, J. R. and Cleary, M. P., Some basic stress diffusion solutions for fluid-saturated elastic porous media with compressible constituens, **Reviews of Geophysics and Space Physics**, Vol.14, No.2, pp.227-241, 1976

Roegiers, J. C. and McLennan, J. D., Factors influencing the initiation orientation of hydraulically induced fractures, presented at the workshop on **Hydraulic Fracturing Stress Measurements** organized U.S.G.S. Office of Earthquake Studies and U.S. National Committee for Rock Mechanics, Monterey, Calif., Dec., 1981

Sato, R., Crustal deformation due to dislocation in a multi-layered medium, **Journal of Physics of the Earth**, Vol.19, pp.31-46, 1971

Sato, R. and Matsuura, M., Static deformations due to the fault spreading over several layers in a multi-layered medium; Part I: Displacement, **Journal of Physics of the Earth**, Vol.21, pp.227-249, 1973

Sato, R. and Matsuura, M., Strains and tilts on the surface of a semi-infinite medium, **Journal of Physics of the Earth**, Vol.22, pp.213-221, 1974

Sato, R. and Matsuura, M., Static deformation due to the fault spreading over several layers in a multi-layered medium; Part II: Strain and tilt, **Journal of Physics of the Earth**, Vol.23, pp.1-29, 1975

Savage, J. C. and Prescott, W. H., Precision of geodolite distance measurements for determing fault movements, **Journal of Geophysical Research**, Vol.78, No.26, pp.6001-6008, 1973

Savage, J. C. and Hastie, L. M., Surface deformation associated with dip-slip faulting, **Journal of Geophysical Research**, Vol.71, No.20, pp.4897-4904, 1966

Savage, J. C., Prescott, W. H., Lisowski, M. and King, N. E., Strain accumulation in southern California 1973-1980, **Journal of Geophysical Research**, Vol.86, pp.6991-7001, 1981

Schuster, C. L., Detection within the wellbore of seismic signals created by hydraulic fracturing, **53th anual Fall Meeting of the Society of Petroleum Engineers of AIME**, SEP 7448, Houston, 1978

Settari, A. and Raisbeck, J. M., Fracture mechanics analysis in in-situ oil sands recovery, **Journal of Canadian Petroleum Technology**, Vol.18, No.2, pp.85-94, 1979

Shuck, L. Z. and Komar, C. A., The dynamic pressure response of a petroleum reservoir: a field case study, **54th Anual Fall Meeting of The Society of Petroleum Engineers of AIME**, SEP 8349, Las Vegas, 1979

Shuck, L. Z. and Keech, T. W., Monitoring acoustic emission from propagating fractures in petroleum reservoir rocks, **Proceedings of First Conference on Acoustic**

Emission and Microseismic Activity in Geologic Structures and Materials, pp.309-338, Trans Tech Publications, 1977

Sih, G. C., **Methods of analysis and solutions of crack problems, Mechanics of fracture Vol.I**, Noordhoff International Publishing, Leyden, The Netherlands, 1973

Sih, G. C., Strain-energy-density factor applied to mixed mode crack problems, **International Journal of Fracture**, Vol.10, No.3, pp.305-321, 1974

Simonson, E. R., Abou-sayed, A. S and Clifton, R. J., Containment of massive hydraulic fractures. **Journal of Society of Petroleum Engineers of AIME**, Vol.18, No.1, pp.224-255, 1971

Smith, M. B., Holman, G. B., Fast, C. R. and Covlin, R. J., The azimuth of deep, penetrating fractures in the Wattenberg Field. **Journal of Petroleum Technology**, AIME, Vol.30, pp.185-193, 1978

Sneddon, I. N., The distribution of stress in the neighborhood of a crack in an elastic solid, **Proc. Roy. Soc. London**, A, 187, pp.229-260, 1946

Sneddon, I. N., **Fourier transform**, in International Series in Pure and Applied Mathematics, McGraw-Hill, 1951

Sokolnikoff, I. S., **Mathematical Theory of Elasticity**, Second Edition, McGraw-Hill, 1956

Solberg, P., Lockner, D. and Byerlee, J., Shear and tension hydraulic frqctures in low permeability rocks. **Pure Applied Geophysics**, Vol.115, No.1, pp.191-198, 1977

Sondergeld, C. H. and Estey, L. H., Acoustic emission study of microfracturing during the cyclic loading of Westerly granite, **Journal of Geophysical Research**, Bol.86, No.B4, pp.2915-2924, 1981

Steketee, J. A., On Volterra's dislocations in a semi-infinite elastic medium, **Canadian Journal of Physics**, Vol.36, pp.192-205, 1958

Steketee, J. A., Some geophysical applications of the elasticity theory of dislocations, **Canadian Journal of Physics**, Vol.36, pp.1168-1198, 1958

Sun, Ren Jen, Theoretical size of hydraulically induced horizontal fractures and corresponding surface uplift in an idealized medium, **Journal of Geophysical Research**, Vol.74, No.25, pp.5995-6011, 1969

Swanson, D. A., Jackson, D. B., Koyanagi, R. T. and Wright, T. R., The February 1969 east rift eruption of Kilauea Volcano, Hawaii, **U.S. Geol. Surv. Prof. Paper**, No.891, pp.1-24, 1976

Takeuchi, H., **Danseiron**, Sho-kabo, Tokyo, 1969 (Japanese)

Thatcher, W., Horizontal crustal deformation from historic geodetic measurements in southern California, **Journal of Geophysical Research**, Vol.84, pp.2351-2370, 1979

Tsukahara, H., Ikeda, R., Satake, H., Ohtake, M. and Takahashi, H., In situ stress measurements by hydrofracturing in Japan, **International Symposium on Earthquake Prediction**, Unesco Headquaters, Paris, April 1979

Von Schonfeldt, H. and Fairhurst, C., Open hole hydraulic fracturing, **The 3rd Symposium on Salt**, Vol.2, pp.404-409, Cleaveland, Ohio, 1969

Warpinski, N. R., Northrop, D. A. and Schmidt, R. A., Direct observation of hydraulic fractures at a formation interface, Sandia Laboratories, New Mexico, **SAND-78-1935**, Oct., 1978

Walsh, J. B., Dip angle of faults as calculated from surface deformation, **Journal of Geophysical Research**, Vol.74, pp.2070-2080, 1969

Walsh, J. B. and Decker, R. W., Surface deformation associated with volcanism, **Journal of Geophysical Research**, Vol.76, pp.3291-3302, 1971

Welsh, W., A Review of the adjustments of free networks,

Survey Review, Vol.25, pp.167-180, 1979

Wiggins, R. A., The general inverse problem: Implication of surface waves and free oscillations for the earth structure, **Reviews of Geophysics and Space Physics**, Vol.10, pp.251-285, 1972

Withers, R. J., Seismicity and stress determination at man-made lakes, **Ph.D Thesis, The University of Alberta**, 1977

Wood, M. D., Holzhausen, G. R., Smith, C., Porter, S., Bachmann, W. and Khaw, M., A system for mapping and monitoring subsurface processes in enhancing recovery schemes, **The Future of Heavy Crude and Tar Sands**, Mcgraw-Hill, Inc., 1981

Wyatt, F. and Berger, J., Investigations of tilt measurements using shallow borehole tiltmeters. **Journal of Geophysical Research**, Vol.85, No.B8, pp.4351-4362, 1980

Yamakawa, N., Naibu-rikigen niyoru semi-infinite elastic body no henkei nitsuite, **Jisin**, Vol.8, pp.84-98, 1955 (Japanese)

Yonekura, N., Sekai no kyodai-jishin katarogu, **Chikyu Kagaku**, Vol.8, pp.263-270, Iwanami Shoten, 1978 (Japanese)

Zobach, M. D. and Pollard, D. D., Hydraulic fracture propagation and interpretation of pressure-time records for in-situ stress determination. **19th U.S. Symposium on Rock Mechanics**, pp.14-22, 1978